2016

Insights into the link between bulk and surface properties of solid oxide fuel cell cathode materials

Alex Christian Tomkiewicz
Lehigh University

Recommended Citation

Tomkiewicz, Alex Christian, "Insights into the link between bulk and surface properties of solid oxide fuel cell cathode materials" (2016). *Theses and Dissertations*. 2847.
http://preserve.lehigh.edu/etd/2847

Insights into the link between bulk and surface properties of solid oxide fuel cell cathode materials

by

Alex C. Tomkiewicz

Presented to the Graduate and Research Committee
of Lehigh University
in Candidacy for the Degree of
Doctor of Philosophy

in

Chemical Engineering

Lehigh University

May, 2016

DISSERTATION SIGNATURE SHEET

Approved and recommended for acceptance as a dissertation draft in partial fulfillment of the requirements for the degree of Doctor of Philosophy.

____
Date

____
Dissertation Director

____
Accepted Date

Committee Members:

____
Prof. Steven McIntosh

____
Prof. James Gilchrist

____
Prof. Hugo Caram

____
Prof. Jonas Baltrusaitis

____
Prof. Nicholas Strandwitz

Acknowledgement

This dissertation is the culmination of my hard work and effort over the past five years at Lehigh University, but it would never have come to fruition without the support I have received. I would like to thank my advisor Prof. Steven McIntosh for his continued support and guidance in my research and for teaching me the critical thinking required of a PhD. I would similarly like to thank my committee members Prof. James Gilchrist, Prof. Hugo Caram, Prof. Jonas Baltrusaitis, and Prof. Nicholas Strandwitz for their time and advice.

I would like to thank my co-workers Mazin Tamimi and Hyunho Shin for their assistance in my experiments and in day to day life. Simiarly, I would like to thank John Caffrey and Henry Luftman for their technical support in constructing the experimental apparatus and performing surface composition measurements respectively. I would also like to thank Dr. Ashfia Huq of Oak Ridge National Laboratory for her instruction and guidance in crystallography and neutron powder diffraction.

Finally, I would like to thank my family for their support throughout my life. Always having a safe and relaxing atmosphere to return to after weeks of learning and research has meant the world to me. I want to thank my brother, Dylan for cheering me up and helping me maintain my sanity. Lastly, I would also like to thank my parents, John and Heidi Tomkiewicz for their moral support and love.

I. Table of Contents

Acknowledgement iii

I. Table of Contents iv

II. List of Tables vii

III. List of Figures ix

IV. List of Symbols xiii

1 Abstract 1

2 Introduction 2

2.1 Background and Motivation 2

2.2 SOFC Operation 4

2.3 Material Selection 6

2.4 Powder Synthesis 11

2.5 X-Ray Powder Diffraction (XRD) 12

2.6 Neutron Diffraction Experiments 14

2.7 Rietveld Refinement 17

2.8 Pulse Isotope Exchange Experiments 19

2.9 Electrochemical Impedance Spectroscopy (EIS) 22

2.10 X-Ray Photoelectron Spectroscopy (XPS) 24

2.11 High Sensitivity – Low Energy Ion Scattering (HS-LEIS) 26

3 Evidence for the Low Oxygen Stoichiometry of Cubic $Ba_{0.5}Sr_{0.5}Co_{0.5}Fe_{0.5}O_{3-\delta}$ from In-Situ Neutron Diffraction 28

3.1 Introduction 28

3.2 Experimental 30

3.3 Results and Discussion 31

3.4 Conclusion 41

4 On the Link Between Bulk Structure and Surface Activity of Double Perovskite Based SOFC Cathodes 42

4.1 Introduction 42

4.2 Experimental 43

4.3 Results 45

4.4 Discussion 51

4.5 Conclusion 55

5 Oxygen Transport Pathways in Ruddlesden-Popper structured oxides revealed via in situ neutron diffraction 56

5.1 Introduction 56

5.2 Experimental 58

5.3 Results 60

5.4 Discussion 79

5.5 Conclusion 85

6 Is the surface oxygen exchange rate linked to bulk ion diffusivity in mixed conducting Ruddlesden-Popper phases? 86

6.1 Introduction 86

6.2 Experimental 89

Material synthesis......89
In situ determination of bulk crystal structure......90
Surface oxygen exchange......90
Surface composition......91
6.3 Results......92
In situ neutron diffraction......92
Surface exchange and composition......101
6.4 Discussion......105
6.5 Conclusion......108
7 Structural Analysis of $PrBaMn_2O_{5+\delta}$ under SOFC Anode Conditions by In-Situ Neutron Powder Diffraction......110
7.1 Introduction......110
7.2 Experimental......111
7.3 Results and Discussion......114
7.4 Conclusion......125
8 Conclusion......126
9 References......128
10 Vita......148

II. List of Tables

Table 3.1: Cubic, space group $Pm3m$, Rietveld fit parameters for BSCF at pO_2 of 10^{-1} atm refined using: (a) neutron data and (b) synchrotron data 34

Table 5.1: Tetragonal space group I4/mmm, Rietveld fit parameters for RPn1 structure at 1070 K..62

Table 5.2: Tetragonal space group I4/mmm, Rietveld fit parameters for RPn2 structure at 1070 K..63

Table 5.3: Tetragonal space group I4/mmm, Rietveld fit parameters RPn3 structure at 1070 K..64

Table 6.1: Tetragonal space group I4/mmm, Rietveld fit parameters for RPn1 structure at 967 K..94

Table 6.2: Tetragonal space group I4/mmm, Rietveld fit parameters for RPn2 structure at 967 K..95

Table 6.3: Tetragonal space group I4/mmm, Rietveld fit parameters for RPn3 structure at 967 K..96

Table 6.4: Direct oxygen transport distances through least occupied sites at 967 K......97

Table 7.1: Measured and calculated outlet pO_2 as a function of gas composition and temperature...113

***Table 7.2**: Tetragonal space group P4/mmm, Rietveld fit parameters for Model 1 structures at 984 K, log (pO_2) = -20.85* 116

***Table 7.3**: Tetragonal space group P4/mmm, Rietveld fit parameters for Model 2 (no O3) structures at 984 K, log (pO_2) = -20.85* 117

Table 7.4: Quality of fit for Model 1 and Model 2 over a range of measurement conditions. 120

Table 7.5: Bond valence sums around each cation / anion under all measured conditions. ………125

III. List of Figures

Figure 2.1: Diagram of solid oxide fuel cell during operation 5

Figure 2.2: Diagram of movement in oxygen in (1) a purely electronic conducting cathode and (2) a mixed ionic electronic conductor.. 7

Figure 2.3: Oxygen vacancy formation in a perovskite 8

Figure 2.4: Comparison between a) single perovskite structure with disordered mixture of A site cations and b) ordered double perovskite structure with alternating A and A' layers 10

Figure 2.5: Ruddlesden-Popper structures for a) n=1, b) n=2, and c) n=3....................11

Figure 2.6: Bragg's diffraction 14

Figure 2.7: Comparison of neutron scattering length and X-ray form factor. 16

Figure 2.8: Diagram of oxygen exchange during usage of isotopic pulse technique......20

Figure 2.9: Example Nyquist plot for a process with a dominating low-frequency response and a smaller high-frequency response 23

Figure 2.10: Schematic of the photoemission process in XPS. a) Incident photon energy $h\nu$ is absorbed by a core level electron. b) If $h\nu > EB$ then the electron is emitted and a core hole is left behind..25

Figure 2.11: Schematic representation of the ion scattering process. 26

Figure 3.1: Representative data from a) neutron diffraction at 1100K with a pO_2 of 0.1 atm and b) Synchrotron diffraction at 295K in air of $Ba_{0.5}Sr_{0.5}Co_{0.5}Fe_{0.5}O_{3-\delta}$. 32

Figure 3.2: a) Refined lattice parameter and oxygen stoichiometries for isotropic and anisotropic oxygen versus temperature. b) Oxygen isotropic thermal parameter U_{iso} compared to anisotropic thermal parameters U_{11},U_{22} and U_{33} with temperature.............36

Figure 3.3: Observed nuclear density map generated by VESTA[40] from 1100K neutron data 37

Figure 3.4: Comparison of oxygen stoichiometry values from literature values for pO_2=0.1 atm 38

Figure 4.1: X-ray diffraction patterns for PBCO, NBCO and GBCO 46

Figure 4.2: RGA signal for m/z= 34 ($^{16}O^{18}O$, red) and m/z =36 ($^{18}O_2$, blue) for a single $^{18}O_2$ pulse response at 298K and 1023K. 47

Figure 4.3: Arrhenius plot of surface reaction rates derived from $^{18}O_2$ isotopic pulse experiments for NBCO, PBCO, and GBCO 48

Figure 4.4: Impedance spectra (electrolyte resistance subtracted) measured for NBCO, PBCO, and GBCO based in electrodes in air at 873K 49

Figure 4.5: Area specific resistance (ASR) for NBCO, PBCO, and GBCO based electrodes in air. 50

Figure 4.6: Comparison of surface oxygen exchange rate and inverse of area specific resistance for GBCO.. 53

Figure 5.1: Ruddlesden-Popper unit cells for a) n = 1 (RPn1), b) n = 2 (RPn2), and c) n = 3 (RPn3) structures. 57

Figure 5.2: Representative data from neutron diffraction at 1070 K with a pO_2 of .1 atm for a) $LaSrCo_{0.5}Fe_{0.5}O_{4-\delta}$ (RPn1), b) $La_{0.3}Sr_{2.7}CoFeO_{7-\delta}$ (RPn2), and c) $LaSr_3Co_{1.5}Fe_{1.5}O_{10-\delta}$ (RPn3) samples. 61

***Figure 5.3**: a lattice parameter for RPn1, RPn2, RPn3.* 65

Figure 5.4: c lattice parameter for RPn1, RPn2, RPn3. 66

Figure 5.5: Fourier observed nuclear density diagram at 1070 K with a pO_2 of .1 atm for $LaSrCo_{0.5}Fe_{0.5}O_{4-\delta}$ (RPn1). 68

Figure 5.6: Fourier observed nuclear density diagram at 1070 K with a pO_2 of .1 atm for $La_{0.3}Sr_{2.7}CoFeO_{7-\delta}$ (RPn2). 69

Figure 5.7: Fourier observed nuclear density diagram at 1070 K with a pO_2 of .1 atm $LaSr_3Co_{1.5}Fe_{1.5}O_{10-\delta}$ (RPn3).. 70

Figure 5.8: Oxygen site occupancies for a)RPn1, b)RPn2, and c)RPn3 phases. 72

Figure 5.9: Direct oxygen transport distances between nearest oxygen sites 75

Figure 5.10: Co/Fe - O bond lengths...77

Figure 5.11: Bond angle of O1 - Co/Fe1 - O2 bond for RPn2 and RPn3 structures......78

Figure 6.1: Ruddlesden–Popper structures for (a) n = 1 (RPn1), (b) n = 2 (RPn2) and (c) n = 3 (RPn3). 89

Figure 6.2: Neutron diffraction patterns collected at 967 K with a pO_2 of 0.1 atm for (a) $LaSrCo_{0.5}Fe_{0.5}O_{4-\delta}$ (RPn1), (b) $La_{0.3}Sr_{2.7}CoFeO_{7-\delta}$ (RPn2), and (c) $LaSr_3Co_{1.5}Fe_{1.5}O_{10-\delta}$ (RPn3) samples..93

Figure 6.3: Observed nuclear density cut along the b–c plane of the least occupied equatorial oxygen for (a) the O2 site of RPn1, (b) the O2 site of RPn2 and (c) the O4 site of RPn3. 99

Figure 6.4: (a) Representative RGA signals for $^{16}O^{18}O$ (m/z = 34, red) and $^{18}O_2$ (m/z = 36, blue) for pulses at 298 K (left) and 973 K (right). (b) Arrhenius plot of surface reaction rates derived from $^{18}O_2$ isotopic pulse experiments for RPn1, RPn2 and RPn3. 102

Figure 6.5: Example LEIS spectra for RPn1, RPn2 and RPn3 samples, showing initial scans of the surfaces after treatment with O atoms and after achieving bulk compositions 104

Figure 6.6: Depth profiles generated by LEIS, showing the fractional surface coverages of Co/Fe, Sr and La for RPn1, RPn2 and RPn3 structures. 104

Figure 7.1: Neutron diffraction patterns collected at 984 K under log (pO_2) = -21.2 for $PrBaMn_2O_{5+\delta}$. 115

Figure 7.2: Two stacked unit cells for $PrBaMn_2O_{5+\delta}$ at 984K, log (pO_2) = -21.2. 118

Figure 7.3: Fourier observed nuclear density diagram at 984 K, log (pO_2) = -21.2 for $PrBaMn_2O_{5+\delta}$. 122

Figure 7.4: Overall stoichiometry of the $PrBaMn_2O_{5+\delta}$ structure as a function of pO_2 and temperature.. 123

Figure 7.5: a and c lattice parameters for $PrBaMn_2O_{5+\delta}$ as a function of temperature. 124

IV. List of Symbols

E	open circuit potential (V)
E_o	reversible potential (V)
F	Faraday’s constant (96485 C/mol)
R	gas constant (8.314 J/mol-K)
T	temperature (K or ^{o}C)
pX	partial pressure of component X
δ	oxygen non-stoichiometry
h, k ,l	Miller index
•	positive charge relative to the lattice in Kröger-Vink notation
′	negative charge relative to the lattice in Kröger-Vink notation
X	no net charge relative to the lattice in Kröger-Vink notation
λ	wavelength of the incident wave
d	Inter planar crystal lattice spacing (Å)
θ	angle (degrees)
Q	Momentum transfer of Eqn. (7)
l	Neutron wavelength of Eqn. (7, 8)
m_n	Neutron mass
R_o	overall surface exchange reaction rate (mol D $\cdot m^{-2} \cdot s^{-1}$) of Eqn. (10)
f_g	fraction of deuterium isotope in gas phase of Eqn (10)
f_o	fraction of deuterium isotope in oxide phase of Eqn. (10)
S	surface area of proton conducting phase of Eqn. (10)
τ_r	Average residence time in the reactor of Eqn. (10)
t	time (s) of Eqn. (10)
n	Number of moles of ^{18}O in gas phase of Eqn. (10)
h	Planck constant ($6.63 x 10^{-34} m^{2}.kg/s$)
v	Frequency of radiation (s^{-1})
E_b	Electron binding energy (eV)
E_k	Kinetic energy of electron (eV)
ϕ	Work function of X-ray photoelectron spectroscopy (XPS)
E_i	energy of primary ion (keV)

E_f	energy of backscattered ion (keV)
k^2	HS-LEIS factor
m_1, m_2	masses of the primary ion and scattering surface atom

1 Abstract

Solid oxide fuel cells (SOFCs) possess the potential for efficient conversion of chemical energy to electrical energy with minimal production of pollutants. Development of intermediate temperature solid oxide fuel cells (IT-SOFCs) requires the development of more active electrode materials due to the high activation energies associated with oxygen dissociation and incorporation.

Both the surface activities and bulk conductivities for oxygen dissociation and transport have been measured for a wide variety of cathode materials utilizing isotopic depth profiling and thermogravimetric analysis techniques, with a correlation found between these values. As discussed within however, these techniques can be misleading for a variety of reasons. Consequently, a combination of bulk and surface measurement techniques including neutron powder diffraction, isotopic oxygen pulsing, as well as surface composition measurements were performed for a range of perovskite-related materials to define the nature of this relationship between surface and bulk properties.

It was found that the link between surface reaction rates and bulk conductivity is caused by a difficulty in measuring the actual “surface” reaction rate, as several materials with notably similar surface compositions exhibited significantly different reaction rates. Similarly, these surface reaction rates were directly linked to the bulk structure through an oxygen vacancy hopping mechanism. As such, we conclude that the measurement of surface reaction rates is limited by an incorporation step which has oxygen on the surface of the material migrate into the bulk structure rather than any actual limitation of oxygen dissociation on the surface or bulk oxygen transport.

2 Introduction

2.1 *Background and Motivation*

Solid Oxide Fuel Cells (SOFCs) are the subject of numerous research efforts due to the promise of efficient conversion of chemical energy to electrical energy with minimal production of pollutants. More recently, investigation of materials for use in intermediate temperature solid oxide fuel cells (IT-SOFCs) which operate in the 773K-973K temperature range has taken center stage due to reduced costs and increased economic feasibility at these temperatures. Operation at these lower temperatures requires more active materials for the electrodes however due to the high activation energies associated with oxygen dissociation and incorporation. Thus, many research groups have devoted their efforts to identifying and measuring the properties of promising new materials.

Numerous studies on the surface reaction rate and bulk diffusion, k* and D* have been conducted by various research groups utilizing a variety of methods such as Electrical Conductivity Relaxation (ECR and Isotope Exchange Depth Profiling (IEDP). These two techniques have been utilized over others for their supposed ability simultaneously measure both k and D, however there is a high degree of uncertainty in these measurements[1-3]. Many of these measurements fail to account for several of the factors that can have a dominating effect on the values of surface reaction rate, most notably of which is the surface composition and how it differs from that of the bulk. Thusly, it is the goal of this proposal to provide a detailed assessment of the properties of a series of materials and to identify how these properties interact with each other.

The proposed work will focus on detailed characterization of $Ln_{0.5}Sr_{0.5}Co_{0.8}Fe_{0.2}O_{3-\delta}$[2,4] (perovskite structure), $LnBaCo_2O_{5+\delta}$ (layered perovskite)[5-8], and $LaSrCo_{0.5}Fe_{0.5}O_{4-\delta}$[9],

$La_{0.3}Sr_{2.7}CoFeO_{7-\delta}$[9,10], $LaSr_3Co_{1.5}Fe_{1.5}O_{10-\delta}$[9] (n=1,2,3 Ruddlesden-Popper phases), where Ln is a lanthanide such as La, Nd, Pr, or GD, utilizing detailed characterization techniques such as isotope pulse experiments to determine surface reaction rates, HS-LEIS and XPS techniques to analyze the surface composition and how it differs from that of the bulk, and electrochemical impedance spectroscopy. Links between these measurements and previously taken measurements using neutron diffraction will be examined in order to gain a better understanding of how these properties relate to each other, with several samples prepared under varying conditions to analyze how samples of supposedly identical composition can differ.

The combination of rising fuel costs as well as concerns about the environmental impact of pollutants such as CO2 have led to an increased interest in “clean energy” or otherwise methods of more efficient use of existing fossil fuel resources. One such technology, Solid Oxide Fuel Cells (SOFCs), provides a pathway for the efficient direct conversion of chemical energy to electrical energy, yielding efficiencies significantly higher than existing combustion methods. High temperatures in excess of 1073K are required in order to achieve high power densities despite the high activation energy for oxygen anion transport[11]. These high operating temperatures allow for greater fuel flexibility and higher tolerances to catalyst poisoning[12,13], yet the selection of materials which can withstand these temperatures is limited, greatly increasing system costs. Furthermore, the high temperatures lead to greatly increased rates of thermal degradation and difficulty in system start-up and shut-down due to the great temperature differentials involved[13,14].

To avoid these issues, research on “intermediate temperature solid oxide fuel cells” (IT-SOFCs), which operate in the general temperature range of 773-973K is ongoing. These

IT-SOFCs correct many of the issues previously mentioned for higher temperature SOFCs, possessing increased lifespans and reduced costs as well as easier operation, greatly increasing their commercial viability. However, the lower operating temperatures lead to lower power output and increased overpotentials due to the high activation energies required for oxygen incorporation and transport at the cathode[13,14]. Following this, much research has been performed with the goal of identifying potential materials which are able to achieve high rates of reaction at intermediate temperatures and into furthering our understanding of these materials. Understanding the processes occurring at the cathode and the properties of the material that govern them is key to gaining an overall understanding of the system, and thus detailed measurements of bulk and surface structures, reaction rates, and the electrochemical properties of these materials should be performed.

2.2 *SOFC Operation*

Solid oxide fuel cells operate based on the same principals as all electrochemical cells and are comprised of three main components: an anode, an electrolyte, and a cathode. Fuel (typically H_2 or otherwise a light hydrocarbon such as CH_4) is supplied to the cell at the anode where it is oxidized with oxygen contained within the cathode in the reaction:

$$CH_4 + 4O^{2-} \rightarrow 2H_2O + CO_2 + 8e^- \qquad (1)$$

This reaction produces electrons (8 electrons per mole CH_4, 2 electrons per mole H_2) which are fed through an external circuit to the cathode. The cathode is typically exposed to atmospheric or otherwise oxygen-rich conditions. At the cathode, oxygen is reduced to form oxygen anions in the reaction:

$$\frac{1}{2}O_{2\,(g)} + 2e^- \rightarrow O^{2-} \qquad (2)$$

The electrolyte serves as a barrier to the transport of electrons while allowing the transport of O^{2-} anions, thereby completing the cell[12,13].

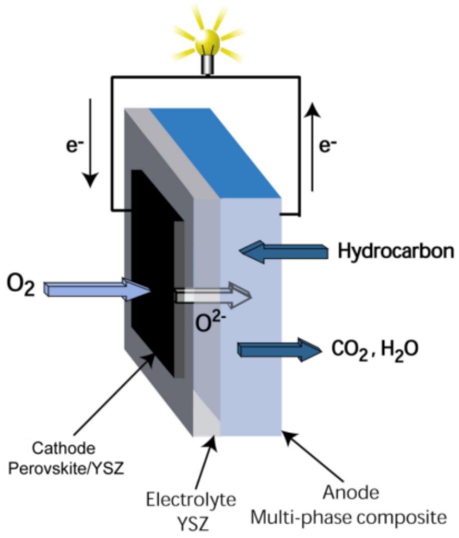

***Figure 2.1**: Diagram of solid oxide fuel cell during operation*

Oxygen anions migrate through the electrolyte due to a difference in the electrochemical potential of oxygen between the anode and the cathode caused by the differing atmospheres each is exposed to. The maximum cell potential that can be generated is described by the Nernst equation, which for a H_2 fuel would be[12]:

$$E = \frac{RT}{4F}\ln\left(\frac{pO_{2,cathode}}{pO_{2,anode}}\right) = E_0 + \frac{RT}{2F}\ln\left(\frac{pO_{2,cathode}^{0.5} \cdot pH_{2,anode}}{pH_2O_{anode}}\right) \qquad (3)$$

Where E_0 is the reversible potential, pH_2, pO_2, and pH_20 are the partial pressures of hydrogen, oxygen, and water at the respective electrodes and R is the gas constant, T is temperature, and F is Faraday's constant.

2.3 *Material Selection*

A working cathode in a solid oxide fuel cell must have: (1) a high catalytic activity to allow rapid oxygen exchange kinetics with the atmosphere, (2) a high electronic conductivity to allow the transport of electrons consumed during oxygen reduction, (3) a high ionic conductivity to allow the rapid transport of oxygen anions into the electrolyte, (4) chemical and structural stability at the operating conditions to prevent physical or chemical degradation of the cathode, and (5) compatibility with the electrolyte material such that the formation of secondary phases which interfere with the transport of oxygen is avoided[15,16].

Mixed ionic electronic conductors (MIEC) are the most suitable for cathode materials in a SOFC, as it greatly enhances the effective catalytic surface of the material. If the cathode is a heterogeneous mixture of ionic and electronic conducting materials, oxygen splitting and incorporation into the cell can only truly occur at the three-phase boundary between these two materials and the oxygen atmosphere. Either the oxygen will react directly at the three phase boundary with electrons flowing into the electronic conductor and oxygen anions incorporating into the ionic conductor, or the oxygen will dissociate on the surface of the electronic conductor, with the resulting anions migrating along the surface to the three-phase boundary (shown as mechanism (1) and (2) in Figure 2.2 respectively). A MIEC material on the other hand is able to react at any surface that is exposed to oxygen, with the oxygen dissociating into oxygen anions that are transported through the MIEC to the electrolyte while electrons are transported to the external circuit. This increase in effectiveness greatly increases the effective rate of oxygen incorporation which is a heavily limiting factor in the operation of SOFCs.

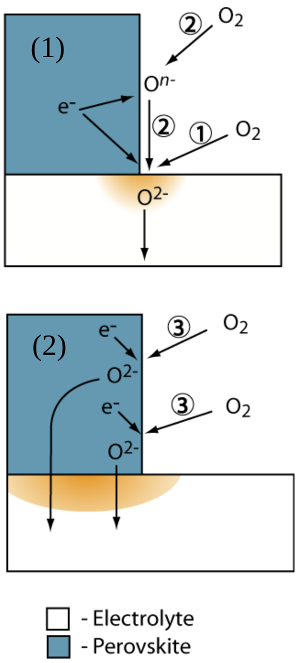

***Figure 2.2**: Diagram of movement in oxygen in (1) a purely electronic conducting cathode and (2) a mixed ionic electronic conductor*

Perovskite structured oxides have the general formula $ABO_{3-\delta}$, where A is a 12-coordinated metal cation such as La, Sr, Ca, or Ba, B is an 8-coordinated transition metal cation, such as Co or Fe, and δ is the degree of oxygen non-stoichiometry. Perovskite materials are commonly used in SOFC applications due to their stability and ability to incorporate a wide range of dopants while maintaining a high concentration of oxygen vacancies, which provide a pathway for oxygen anion transport through the material. Furthermore, these dopants can provide electronic conductivity in addition to this ionic conductivity[12,14,16,17], forming a mixed ionic electronic conductor (MIEC).

Ion conductivity occurs through an oxygen “hopping” mechanism, whereby oxygen anions can “hop” between energetically equivalent oxygen sites thereby allowing transport of oxygen through the material via oxygen vacancies[18]. These vacancies are produced under reducing conditions such as an increase in temperature or a decrease in the partial pressure of O_2. As these oxygen vacancies form, electroneutrality is maintained through reduction of the B-site transition metal cation[18,19]. Similarly, aliovalent doping of the A-site cations causes the formation of oxygen vacancies or charge compensation through the B-sites.

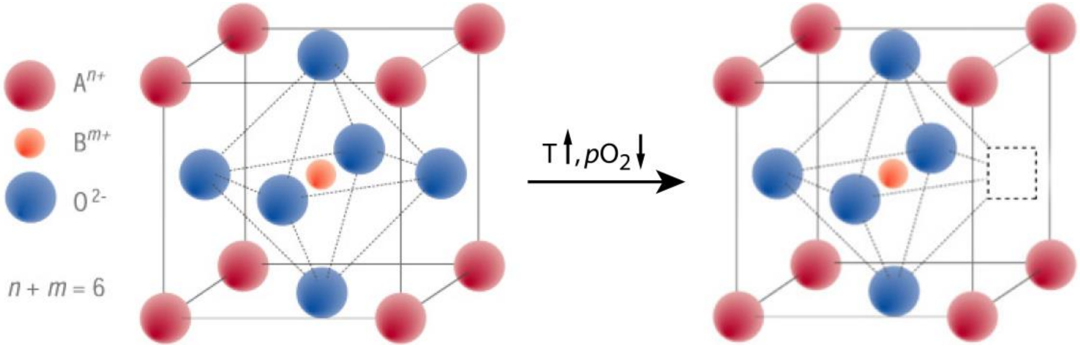

Figure 2.3*: Oxygen vacancy formation in a perovskite*

Kröger-Vink notation provides a convenient method of expressing these electrochemical changes, with neutral, positive, and negative charges relative to the base lattice represented as X, ·, and ‘ respectively. For example, if the A site of $LaCoO_3$ is doped with Sr to form $La_{1-x}Sr_xCoO_3$, the change of x La-site cations from La^{+3} to Sr^{+2} (a net -1 charge from the base state) would be balanced by an equal number of Fe^{+3} cations oxidizing to Fe^{+4} (thereby adopting a net +1 charge from the base state). This can be expressed in Kröger-Vink (for x=1) as:

$$SrCoO_3 \xrightarrow{LaCoO_3} Sr'_{La} + Co^{\cdot}_{Co} + O^{x}_{O} \qquad (4)$$

where Sr'_{La}denotes Sr^{+2} on a La site with a net -1 charge from the base La^{+3}, $Co^{\cdot}_{Co}$denotes Co+4 on a Co site with a net +1 charge from the base Co^{+3}, and O^{x}_{O} denotes O^{+2} on an O site with a neutral charge relative to the base O^{+2}. It should be noted that the same doping could cause the formation of an oxygen vacancy rather than oxidizing the B-site cation, as charge neutrality can also be met through the following:

$$2Co_{Co}^{\cdot} + O_O^x \leftrightarrow 2Co_{Co}^x + V_O^{\cdot\cdot} + \frac{1}{2}O_2 \qquad (5)$$

where $V_O^{\cdot\cdot}$ is an oxygen vacancy, with a net +2 charge from the base O^{2-}. The charge compensation within a perovskite is formed of a mixture of oxygen vacancy formation and oxidation/reduction of the cations, with the ratios determined by temperature and pO_2. It should also be noted that the electronic conductivity of these materials is due to the mixed oxidation states of the B-site cation, allowing for the transport of electrons or holes through the exchange of electrons between $Co_{Co}^{\cdot}, Co_{Co}'$, and Co_{Co}^x.

Double perovskites have the general formula $AA'BO_{5+\delta}$ and are formed by stacked single perovskite unit cells. The size difference between the A and A' cations drives A-site layering into alternating $ABO_{3-\delta}$ and $A'BO_{3-\delta}$ perovskite unit cells in a doubling of the simple perovskite unit cell. The primary difference between the double or layered perovskites and the previously discussed single perovskite structures is that the A and A' atoms form alternating layers in one direction, as shown below:

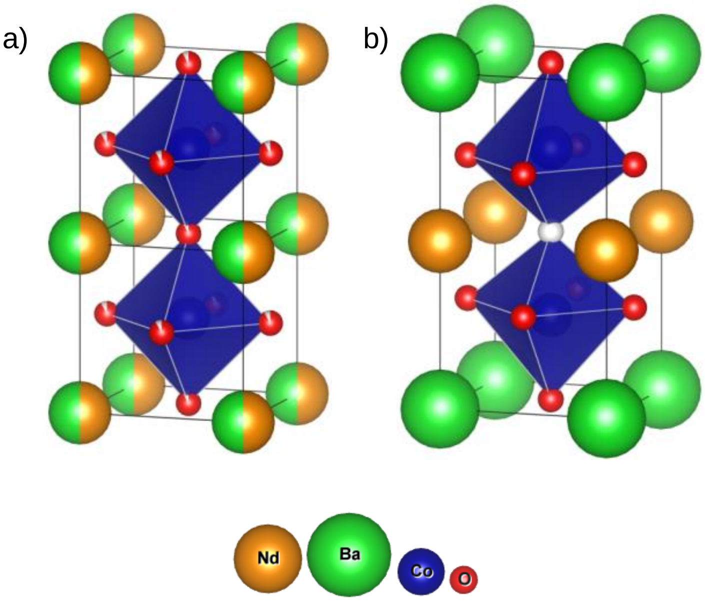

Figure 2.4*: Comparison between a) single perovskite structure with disordered mixture of A site cations and b) ordered double perovskite structure with alternating A and A' layers*

This layering of A and A' site cations leads to a separation of the O sites into three separate crystallographic sites, one each in the layers of the A, A', and B site cations. These oxygen sites have greatly differing properties, and it is typically found that the oxygen occupancies concentrate into either the A or A' layers, leaving the other oxygen sites fully occupied[7,8,16,20,21]. These layers of highly concentrated oxygen vacancies provide pathways for rapid oxygen transport, as they can have occupancies of 50% or less, well below what would be found for the single oxygen site in a typical perovskite.

The Ruddlesden-Popper structure is another variation of the perovskite structure with the general formula $A_{n+1}B_nO_{3n+1}$, where n is the number of layers of ABO_3 perovskite structure occurring before a single layer of a rock-salt structure AO, with this pattern repeating to form the overall crystal structure. These repeating rock-salt layers offset the perovskite structure laterally by half a unit cell each time they occur.

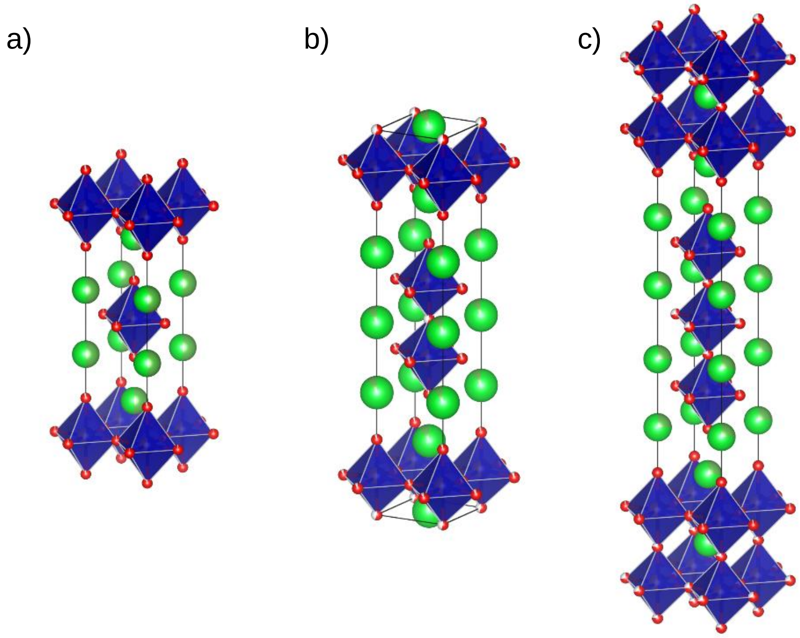

***Figure 2.5**: Ruddlesden-Popper structures for a) n=1, b) n=2, and c) n=3. The octahedrons represent the B-site cations along with the octahedrally coordinated surrounding oxygen.*

The layered nature of the Ruddlesden-Popper structure can provide several different oxygen exchange pathways as compared to the single pathway available in the cubic perovskite, reducing the activation energy of oxygen transport and allowing higher rates at lower temperatures[22,23]. As such, Ruddlesden-Popper and other layered materials are seen as promising candidates for SOFC cathodes[8,22-24].

2.4 *Powder Synthesis*

Several synthesis procedures can be utilized to form metal oxides such as the perovskite structures described previously. The most common of these techniques is the ceramic, or solid state reaction method. Stoichiometric amounts of oxide or carbonate precursors are ground, mixed and then sintered at high temperature. This method however has notable flaws, mostly due to the slow kinetics of the metal cations forming the desired crystal structure, even at high temperatures. Repeated steps of high temperature sintering and grinding of the resulting solids are required to ensure a homogeneous end product[25,26].

An alternative method was developed by Pechini[27] in 1967 to prepare a polymeric resin precursor for the formation of these complex oxides rather than the solid state synthesis method utilized previously. This method utilizes the ability of certain compounds to behave as chelating agents when added to a solution of metal ions, allowing them to remain in solution and maintain a homogeneous mixture. A variation of this method, and the one utilized in our laboratory, is the sol-gel method[28]. Utilizing metal nitrate solutions along with a complexing agent such as citric acid or ethylenediaminetetraacetic acid (EDTA), a homogeneous precursor solution is formed[29,30]. This solution is rendered to a gel-like consistency with atomic level mixing of the metals and subsequently oxidized at high temperatures. The organic compounds fully oxidize and are removed from the product, leading to the formation of a metal oxide with an even distribution of metal cations throughout the solid and allowing the formation of the finalized crystal lattice without requiring repeated sintering steps. This updated methodology not only allows the creation of a single crystalline phase at a lower temperature than would be required for solid state synthesis, but also ensures increased homogeneity of the crystal lattice as there are no localized concentrations of the simple oxides that are utilized in solid state synthesis.

2.5 *X-Ray Powder Diffraction (XRD)*

X-Ray powder diffraction is an incredibly useful characterization tool in the field of solid state chemistry as it can be utilized to identify the unique x-ray diffraction pattern generated by a crystalline structure. This technique allows not only the identification of the crystal structure of the bulk material but can also be used to identify the presence of any impurities such as simple oxides that formed during synthesis.

When X-rays interact with the electron cloud surrounding an atom, secondary spherical waves are created radiating from the electron through elastic scattering. When interacting with a regular array of atoms, such as within a crystalline structure, these emitted waves can interfere with each other through constructive or destructive interference. Where destructive interference occurs, no significant output is generated. Constructive interference on the other hand occurs in specific directions, as defined by Bragg's law:

$$n\lambda = 2d \sin\theta \qquad (6)$$

where *n* is an integer, *λ* is the wavelength of the incident wave, *d* is the spacing between the planes in the atomic lattice, and θ is the angle between the incident ray and the scattering planes. A relation between reflection angle and spacing between planes can be reached given the incident wavelength. These reflections are defined by the indices *h*, *k,* and *l* , which when examined using a predicted crystal symmetry can be used to determine the lattice parameters and atom positions. These calculated diffraction patterns are then compared with the measured diffraction pattern, and the model is updated until the patterns match, yielding the true crystal structure of the sample.

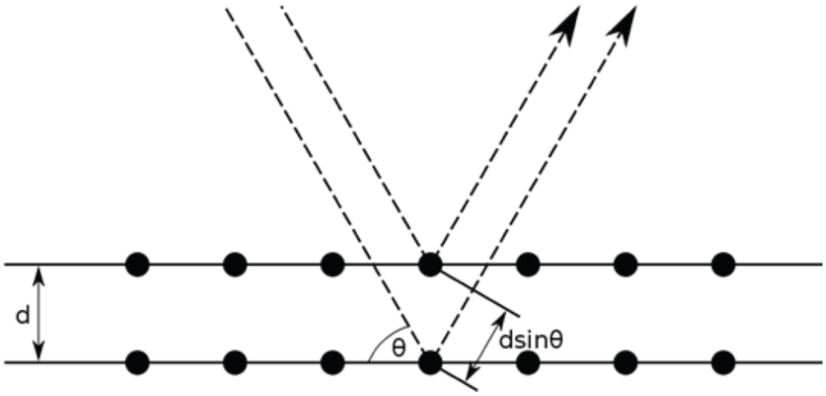

***Figure 2.6**: Bragg's diffraction*

Powder X-ray diffraction was collected with a desktop instrument (Rigaku Miniflex II, Texas, USA) in order to determine phase purity of every sample created. For this purpose, the indexing of peaks (peak position 2θ) was primarily considered, with reduced emphasis on peak intensities. Unidentified peaks typically indicated impurities or a difference in phase, with impurity peaks typically identified as simple oxide phases.

Synchrotron X-ray data was collected at line 11-BM, Advanced Photon Source, Argonne National Labs, Argonne, IL, USA[31], utilizing the mail-in sample program. Synchrotron-generated XRD patterns are much higher resolution than those generated by the desktop instrument and were therefore used to aid in determining potential cation ordering or minor phase differences between samples that would be impossible to detect otherwise.

2.6 ***Neutron Diffraction Experiments***

Neutron diffraction can be utilized to gain similar information about the crystal structure as X-ray diffraction with a few key differences in the measurement and the information gained about each atom. Neutron diffraction, as the name would suggest, utilizes neutrons rather than X-rays as the scanning beam. The neutron passes through the electron cloud (which reflects X-rays) without interaction and instead interacts directly with the atom's nucleus. In addition, rather than measuring the scattering angle, neutron diffraction is measured using neutron time-of-flight scattering, where the initial neutron beam has a fixed initial position and velocity. This beam is broken into individual "pulses", allowing the measurement of the position of deflected neutrons as well as the time after the pulse when they are detected. For a time-of-flight diffractometer, the time of flight can be linked to the diffraction through a combination of Bragg's law (Equation 7) and the de Broglie relationship (Equation 8). This information can be utilized to determine the momentum and energies of the deflected neutrons and thereby provide accurate information about the crystal structure of the sample.

$$l = 2\, d_{hkl} \sin Q \tag{7}$$

$$\frac{h}{l} = m_n \frac{L}{t} \tag{8}$$

The primary advantage of neutron diffraction over X-ray diffraction lies in its ability to achieve a higher intensity from certain atoms (with X-ray diffraction having an advantage for others). The relative importance of a given atom is determined through a combination of its scattering length / form factor (for neutrons and X-rays respectively) and the momentum transfer Q (which is proportional to $\sin\theta / \lambda$). The X-ray form factor linearly increases with atomic number, while the neutron scattering length has no defining relationship and is instead individually determined for each atom, as shown in Figure 2.7. Atoms with similar form factor / scattering length are difficult to distinguish from each other with only one technique, requiring us to utilize both to gain full information about a crystal structure, especially concerning potential ordering. In addition to these effects, the relationship between Q and the scattering power (which determines intensity of the resulting peaks) differs between neutrons and X-rays. Where neutrons have a scattering power independent of Q (constant), X-rays have a significantly higher scattering power for low Q and significantly lower for high Q[32]. It is this difference that shows why detailed information regarding oxygen atoms, a key factor when considering oxygen transporting materials, can be readily obtained with neutron diffraction but not with X-ray diffraction.

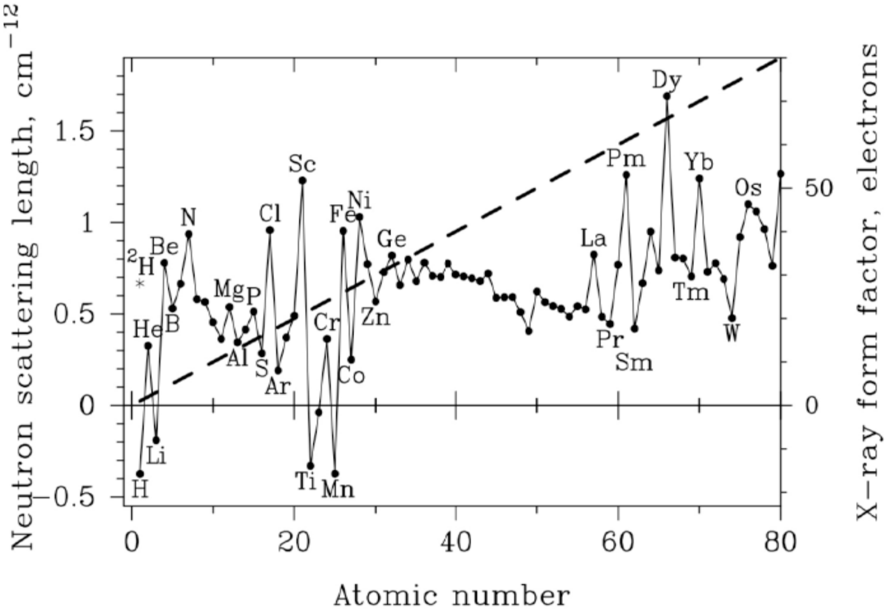

***Figure 2.7**: Comparison of neutron scattering length and X-ray form factor. Neutron scattering lengths are specified per element and the X-ray form factoris displayed as a dashed line. Figure reproduced from* Toby, B.[32]

Thermogravimetric analysis (TGA) is the most commonly utilized technique to determine the oxygen stoichiometry of these materials; however, TGA can be problematic in terms of ensuring sample equilibrium and accurate knowledge of a reference oxidation state from which to calculate all other values. This can lead to significant variation in reported values of oxygen stoichiometry for the same material [33-35]. While there can be issues related to the correlation between the oxygen stoichiometry and anisotropic nuclear densities determined via Rietveld refinement of the neutron diffraction data, there are no issues with reference states. Furthermore, it is important to note that each diffraction data set, that is each composition at each temperature, is analyzed completely independently of all others. Neutron diffraction also allows for the occupancy of each oxygen site to be refined separately, showing localization of vacancy formation, providing a significant advantage over alternative techniques.

Neutron diffraction studies were conducted at the POWGEN beamline, Spallation Neutron Source (SNS), Oak Ridge National Laboratory, Oak Ridge, TN, USA. A powder sample is placed in a quartz sample holder. The sample holder is suspended within the neutron beam utilizing a long quartz rod. The temperature and gas atmosphere of the sample chamber are both continuously controlled. The furnace temperature is calibrated using a ZnO sample[36]. Samples are allowed to equilibrate after each atmosphere change, with several brief data collecton periods (5-10 minutes) used to determine when equilibrium has been reached. Equilibrium is declared after at least 30 minutes of short scans show no significant movement in peak positions or intensities.

2.7 *Rietveld Refinement*

Rietveld[37] refinements for both neutron and synchrotron data were performed using the GSAS package[38]with the EXPGUI interface[39]. Background scans of the sample holder were subtracted from the raw data with the remaining background fit using either a Chebyschev function.

For the neutron diffraction data, the lattice parameter, oxygen fractional occupancy, isotropic atomic displacement parameters for each atom, and profile parameters (γ_1, σ_1 and σ_2) were all refined for each phase individually. Atomic displacement parameters were typically refined for each crystallographic site, as for a disordered structure it is impossible to distinguish between elements located on a singular site. The DIFA and absorption parameters were constrained to be the same for all of the data sets for a given sample, as these should be constant with temperature. The scale factor was held constant when no change in phase was expected.

For the synchrotron data, the background was described by a shifted Chebyschev function with twenty parameters. Lattice parameter, oxygen fractional occupancy, isotropic displacement parameters, profile parameters (LX, ptec, S400, S220), and diffractometer zero and absorption/reflectivity correction were refined[32]. The refined crystal structure was visualized using the VESTA package[40]

Each Rietveld refinement starts with default values with only instrument parameters, crystal symmetry, and atomic positions manually entered. From there, each refinement refines all parameters independently of all other refinements. The reported values and trends in oxygen stoichiometry (decreasing with increasing temperature and decreasing pO_2) and anisotropic or isotropic nuclear density (increasing with increasing temperature and decreasing occupancy) are only compared at the end of all refinements and serve as a check on the relative accuracy of the refinements. Additional checks for accuracy include similar occupancy determination for the same, or very similar, materials by different research teams utilizing different diffractometers and sample environment systems [33,41,42], and correlation between structure controlled and diffraction determined oxygen stoichiometry. This second check is clearly demonstrated in the accurate determination that the perovskite $SrCo_{0.8}Fe_{0.2}O_{2.5}$ is formed from disordering of the Brownmillerite structured $Sr_2Co_{1.6}Fe_{0.4}O_5$ phase[43]

2.8 *Pulse Isotope Exchange Experiments*

Measurements of the surface reaction rate are taken using an isotopic pulse exchange technique, as described by Bouwmeester et al.[44] and as previously implemented for H_2/D_2 exchange in our laboratory[45,46]. A sample of the cathode powder (sieved to a specified particle size) is placed in a quartz tube and held in place by plugs of quartz wool. The reactor tube is placed in a tube furnace and heated to 1073K in an atmosphere of 21% O_2/N2 for 30 minutes to clean the surface of any carbonates that had formed since the sample synthesis[47]. Gas flow rates were regulated by mass flow controllers [Brooks, 4850 series, Exton, Pa, USA]. A continuous flow of natural abundance O_2 [OX 4.3UH, Praxair] /N_2 [NI 5.0UH, Praxair] mixture is flowed over the reactor bed to maintain a constant pO_2, and the sample is allowed to equilibrate to a specified temperature and pO_2. A mixture of $^{18}O_2$ [97 atom%, Sigma-Aldrich, Miamisburg, Oh, USA] /N_2 at the same pO_2 as the previously described gas mixture is flowed through a 500 µL sample loop attached to a computer controlled 6-way valve with a pneumatic actuator [Swagelok model 131 SR] such that when the valve is actuated, the natural abundance mixture pushes the isotopic gas mixture contained in the sample loop over the reactor bed, thereby creating the isotopic pulse.

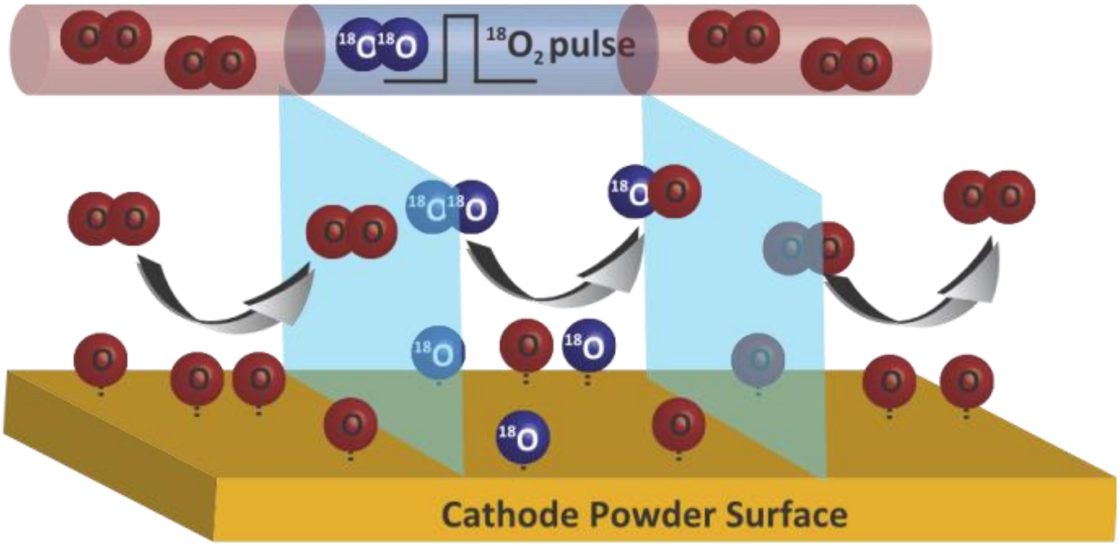

***Figure 2.8**: Diagram of oxygen exchange during usage of isotopic pulse technique*

The sample, which is in chemical equilibrium with oxygen even during the isotopic pulse and therefore has no driving force for incorporation/release of oxygen to/from the sample, has $^{18}O_2$ react with the surface, forming ^{18}O surface species in place of the previously saturated ^{16}O surface. The ^{18}O surface species then react with surface ^{16}O, creating $^{16}O^{18}O$ species in the gas phase. It should be noted that ^{18}O surface species do not re-combine, as the surface saturation of ^{16}O makes it incredibly unlikely for two ^{18}O surface species to interact. By measuring the consumption of $^{18}O_2$ gas species and the production of $^{16}O^{18}O$ gas species, the surface reaction rate on the material can be measured.

The products of each pulse set are continuously analyzed (sampling frequency, 1.67 s^{-1}) using a residual gas analyzer (RGA) fitted with a quadrapole analyzer and associated Faraday and secondary electron multiplier detectors (Cirrus 2, MKS Instruments UK Ltd). The $^{16}O_2$ (m/z = 32) signal does not vary significantly over the course of the pulse experiments due to the short duration of the pulse compared to the residence time in the

RGA chamber. Considering this, only the $^{16}O^{18}O$ (m/z = 34) and $^{18}O_2$ (m/z = 36) signals are measured. The amount of $^{18}O2$ consumed by the powder sample is determined by comparing the average peak area between the reactive and baseline room temperature experiments. The areas are calculated through numerical integration using the mean value of the signal previous to the pulse as a baseline.

The surface exchange rate, Ro (mol ^{18}O m^{-2} s^{-1}), is calculated based on the $^{16}O^{18}O$ and $^{18}O_2$ pulse responses[44] using the equation:

$$n\frac{\partial f_g}{\partial t} = -R_o S\left(f_g - f_o\right) \qquad (9)$$

where S is the total surface area, n is the total amount of ^{18}O atoms in the gas phase, and f_g and f_o are the fractions of ^{18}O in the gas and the oxide phase respectively. The fraction in the oxide, f_o is assumed to be negligible in comparison to f_g, as the sample is held in equilibrium with natural abundance oxygen, primarily ^{16}O, prior to pulsing. Under the assumptions of plug flow within the reactor bed as well as first order reaction kinetics, the surface exchange rate can be expressed as:

$$R_o = \frac{n}{S\tau_r} ln\frac{f_{g,i}}{f_{g,e}} \qquad (10)$$

where τ_r represents the average residence time in the reactor and $f_{g,i}$ and $f_{g,e}$ represent the $^{18}O_2$ volumetric fraction in the pulse at the inlet and exit of the reactor, respectively. The $^{18}O_2$ fractions were evaluated as a weighted sum of the $^{16}O^{18}O$ and $^{18}O_2$ responses, with $f_g^{18} = f_g^{36} + 0.5f_g^{34}$. This measured isotopic exchange rate is analogous to k* in the terminology proposed by Maier[48].

The sample size of the isotope pulses are designed to minimize the influence of bulk ionic transport on the measured surface reaction rate. Flow conditions were chosen such that the measured reaction rate was independent of carrier gas flow rates, ensuring that the above equations are valid for all measurements.

2.9 *Electrochemical Impedance Spectroscopy (EIS)*

Electrochemical impedance spectroscopy is a technique that analyzes the frequency response of a cell to an applied alternating current. The overall electrochemical performance of the cell is broken up into various processes, such as surface reaction of the electrode, oxygen transport through the electrode, and oxygen transport through the electrolyte to name a few of the more important processes. Each of these processes has an associated rate constant and therefore an associated time scale. When the applied frequency is much greater than the time scale of a process, the system reacts quickly to the alternating current, making the process behave as a resistor. Conversely, when the frequency is much less than the time scale, the process is unable to respond and therefore the process has no impact on the overall performance. Between these two extremes however, a phase shift is created by the limitations of the process, creating “imaginary” impedance, which can be shown on a Nyquist plot.

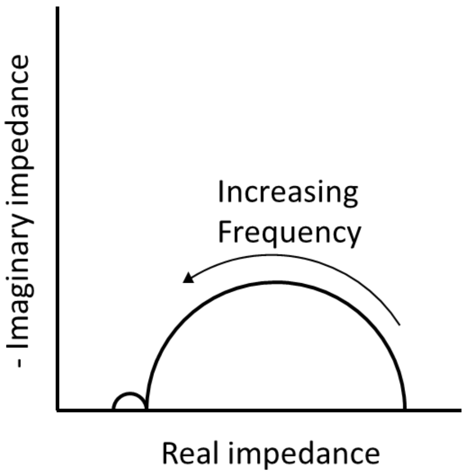

***Figure 2.9**: Example Nyquist plot for a process with a dominating low-frequency response and a smaller high-frequency response*

These processes that limit the overall cell at varying frequencies are plotted as semi-circular arcs, where the size of the arc is proportional to the effective resistance of that process. Several of these arcs can also overlap, although in this case it is very difficult to distinguish between them. In a case similar to the example shown above where one arc is dominating the process, it can be determined that the limiting process causing the dominant arc is the one with the largest resistance and therefore the slowest reaction rates. Identifying this limiting process is key to understanding how electrode materials can be improved. In our lab, we analyze the impedance of symmetric cells comprised of an electrolyte and 2 identical electrodes, thereby reducing the number of arcs caused by the electrodes as the identical electrodes will create arcs that perfectly overlap.

The symmetric cell is formed using a dense pellet of electrolyte material such as $Gd_{0.2}Ce_{0.8}O_{2.9}$. This pellet is formed by uniaxial pressing of electrolyte powder, the result of which is then sintered for 4 hours at 1623K in air to form the dense pellet. The electrodes are formed of an equal weight mixture of the electrode powder to be tested and electrolyte powder which were ball-milled together in a slurry with ethanol. The resulting powder was dried and mixed with an equivalent volume of graphite powder, creating an electrode ink which was painted in the center of each side of the electrolyte pellet and then sintered at 1373K for 4h. Silver wire was attached to each side of the electrodes with silver ink to ensure good electrical contact, resulting in the completed symmetric cell which could be analyzed using EIS.

2.10 *X-Ray Photoelectron Spectroscopy (XPS)*

The first of two techniques that our laboratory uses to identify the surface composition of a material is X-ray Photoelectron Spectroscopy (XPS). Understanding the surface composition is important to fully understand the surface reaction rate, as the surface composition and structure can differ significantly from the bulk[45,49,50]. XPS is able to analyze the composition of the material to a depth of ~10 nm, obtaining information on the atoms comprising the top ~20 layers. In addition to information about composition, XPS is able to determine information about the chemical state of the atoms in the measured layers.

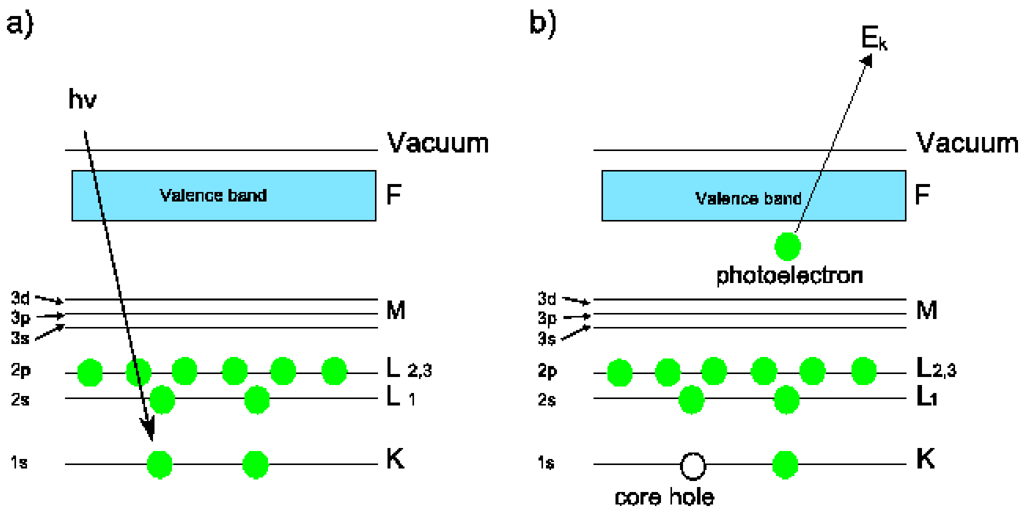

***Figure 2.10**: Schematic of the photoemission process in XPS. a) Incident photon energy $h\nu$ is absorbed by a core level electron. b) If $h\nu > E_B$ then the electron is emitted and a core hole is left behind. This core hole may be filled by an electron from a higher state, causing emission of a secondary photon or an Auger electron. Figure reproduced from* Leadley, D.[51]

XPS measurements are performed under high vacuum, allowing an incident beam of x-rays to strike the surface atoms, exciting an electron which is then potentially ejected from the electron cloud. The ejected electron has a specified kinetic energy, E_k, determined by taking the difference between the energy imparted by the x-ray, *hv*, and the electron binding energy E_b, where *h* is Planck's constant and *v* is the frequency of the radiation.

$$E_k = hv - E_b \qquad (11)$$

Measured experimentally, an additional factor of the work function of the spectrometer, Φ, must be considered.

$$E_k = hv - E_b - \phi \qquad (12)$$

The composition of the surface can be determined through a combination of the ejected electron's E_k, allowing the identification of an atom and its chemical state, and the number of electrons ejected at that energy, corresponding to the relative abundance of that species.

2.11 *High Sensitivity – Low Energy Ion Scattering (HS-LEIS)*

Low Energy Ion Scattering (LEIS) is another surface sensitive technique that is much more sensitive to the surface layers, only measuring up to a depth of the first few atomic layers. A noble gas ion (primary ion) strikes the surface of the material in a vacuum with an incident energy E_i as shown in Figure 2.11.

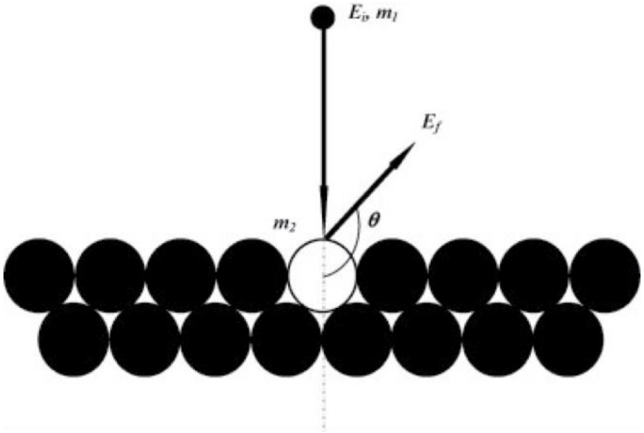

Figure 2.11*: Schematic representation of the ion scattering process. Figure reproduced from ter Veen* et al.[52]

The energy of the backscattered ion, E_f, is determined through a combination of conservation of momentum and conservation of energy, as shown below:

$$E_f = k^2\left(\frac{m_2}{m_1}, \theta\right) E_i \qquad (13)$$

Where m_1 and m_2 are the masses of the primary ion and the scattering surface atom, respectively, and θ represents the back scattering angle. The factor k^2 is a known function of m_1/m_2 and θ, increasing monotonously from 0 for $m_1/m_2 = 1$ to 1 for m_1/m_2 approaching infinity (if $\theta > 90°$). With this equation, the mass of the scattering surface atom can be identified from the change in ion energy, allowing accurate identification and quantification of the top atomic layer. In addition, through alternating use of LEIS and sputtering, a depth profile of the surface layers can be achieved, allowing us to understand the transition from surface compositions to those of the bulk.

3 Evidence for the Low Oxygen Stoichiometry of Cubic $Ba_{0.5}Sr_{0.5}Co_{0.5}Fe_{0.5}O_{3-\delta}$ from In-Situ Neutron Diffraction

3.1 *Introduction*

The series (Ba,Sr)(Co,Fe)$O_{3-\delta}$ (BSCF) has received a great deal of interest as an MIEC perovskite cathode material[1,8,42,53-67], with the composition $Ba_{0.5}Sr_{0.5}Co_{0.8}Fe_{0.2}O_{3-\delta}$ (BSCF5582) having been shown to provide one of the lowest cathode polarization resistances[68], and one of the highest oxygen fluxes when employed as an oxygen separation membrane [58,67]. Initial measurements of the structure and oxygen stoichiometry of BSCF5582 by *in-situ* neutron diffraction[42] indicated that this high performance may be due to the very high oxygen non-stoichiometry, δ, of the material, leading to rapid ionic transport by providing a high concentration of oxygen vacancies. This initial report led to a number of researchers attempting to confirm the low oxygen stoichiometry using the traditional thermogravimetric approach. This has led to a wide range of reported values, none of which are as low as those reported previously in neutron studies[54,55,57,61,69].

The reported oxygen stoichiometry of BSCF5582 is significantly lower than for the comparable material, $SrCo_{0.8}Fe_{0.2}O_{3-\delta}$, even though the total A-site charge in both cases is 2+[70]. Clearly the presence of Ba^{2+} influences the oxygen stoichiometry beyond simple charge compensation arguments. One argument is that the increased relative size of the Ba^{2+} cation leads to greater reducibility of the B-site cations through the increased lattice parameter and associated increase in bond length[55,69]. Understanding this non-linear effect may lead to the development of more appropriate materials for these applications. Thus there is some debate regarding the correct oxygen stoichiometry values for this range of materials, and a necessity to understand the influence of Ba^{2+}in determining the ionic conductivity of the title material.

Thermogravimetric analysis and coulometric titration provide accurate measurements of the mass or oxygen stoichiometry differential between different sample conditions (temperature and oxygen partial pressure, pO_2) however, in order to determine an absolute stoichiometry a reference state must be established. This reference point is typically obtained by reducing the sample in H_2 and assuming reduction to base components (BaO, SrO, Co, and Fe for BSCF)[54,55,66], or by titration[57,58]. Inaccuracies in determining this reference point can lead to an offset in the reported oxygen stoichiometry. TGA also typically requires long equilibration times, which may be problematic for BSCF5582 as it has been reported to undergo a slow phase transformation from cubic to hexagonal structure[66].

Neutron diffraction techniques take a different approach, allowing the simultaneous determination of absolute oxygen stoichiometry and crystal structure at varying temperatures and pressures. Phenomena such as site ordering can also be seen, an advantage that is not offered through TGA measurements or coulometric titration. The accuracy of values refined from neutron diffraction measurements are determined by the goodness of fit of the crystallographic model to the diffraction data.

This experiment sets out to utilize neutron and synchrotron diffraction data to determine oxygen stoichiometry for $Ba_{0.5}Sr_{0.5}Co_{0.5}Fe_{0.5}O_{3-\delta}$ and compare the calculated values to those previously reported in the literature. Differences between values reported here and those reported previously were investigated. In addition, calculated diffraction patterns from phases involving cation ordering were compared to obtained data to determine whether the BSCF structure is ordered or disordered.

3.2 *Experimental*

$Ba_{0.5}Sr_{0.5}Co_{0.5}Fe_{0.5}O_{3-\delta}$ (BSCF5555) powder was synthesized using metal nitrate solutions through the modified Pechini method described in Section 1.4. The resulting cake was ground and calcined in air at 1273K for 8h with 5K/min heating and cooling rates. BSCF5555 powder was reduced for 12h at 1173K in flowing 5% H_2/N_2 and the reduced powder characterized by X-ray diffraction (Rigaku Miniflex II, Texas, USA).

Neutron diffraction studies were conducted as described in section 1.6. 3.72g of the BSCF powder sample was utilized. The powder sample was equilibrated in 500 sccm of ultra-high purity O_2 and N_2 mixed to give pO_2=0.1 atm. Diffraction patterns were collected at 1100K, 1001K, 898K, and 793K, in that order, in the d-spacing range of 0.45 – 3.8 Å until a total accelerator source proton charge of 3.30×10^{12} pC (~1 hour measuring time) was reached.

Synchrotron X-ray data was collected at line 11-BM, Advanced Photon Source, Argonne National Labs, Argonne, IL, USA[31], utilizing the mail-in sample program. The profile was collected at room temperature with a calibrated wavelength of 0.413895 Å.

Rietveld[37] refinements for both neutron and synchrotron data were performed using the GSAS package[38]with the EXPGUI interface[39]. For the neutron data, background scans of the quartz sample holder were subtracted from the raw data with the remaining background fit using a shifted Chebyschev function with eighteen refined terms. The scale factor was allowed to refine separately for each data set. Constraining the scale factors to be equal caused no change in the refined values for oxygen occupancy and thermal parameters within one standard deviation. For the synchrotron data, the background was described by a shifted Chebyschev function with twenty parameters. The standard deviations of the refined values are indicated by error bars on the relevant data points. The crystal structure was visualized using the VESTA package[40]

3.3 ***Results and Discussion***

Neutron (elevated temperatures) and synchrotron (room temperature) data, Figure 3.1, were refined to determine the crystal structure of BSCF5555. The synchrotron data was primarily utilized to determine whether cation ordering was present in the material as X-ray diffraction enables clear differentiation between cations. In contrast, neutron diffraction is more sensitive to oxygen, enabling accurate determination of oxygen stoichiometry under *in-situ* conditions.

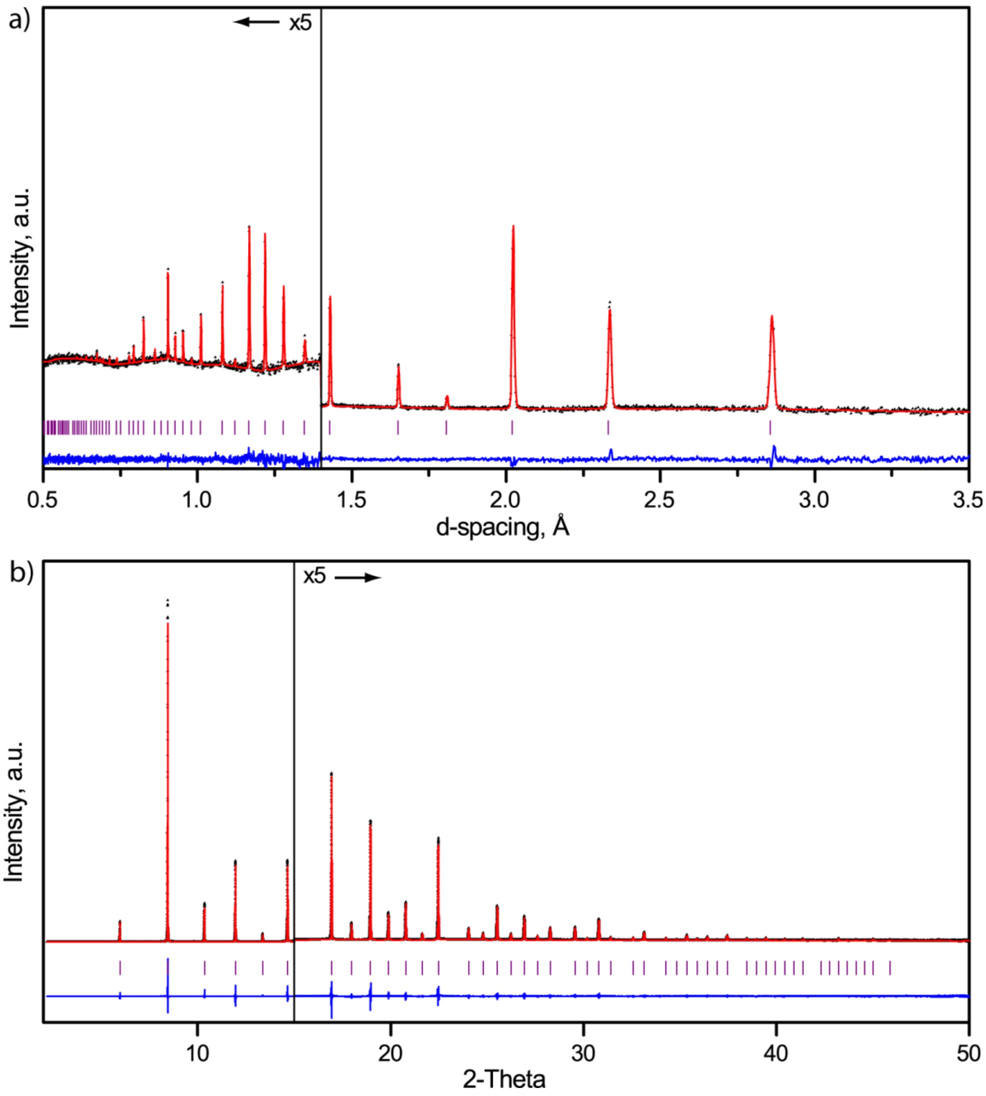

Figure 3.1*: Representative data from a) neutron diffraction at 1100K with a pO_2 of 0.1 atm and b) Synchrotron diffraction at 295K in air of $Ba_{0.5}Sr_{0.5}Co_{0.5}Fe_{0.5}O_{3-\delta}$. Measured data (black dots), calculated diffraction pattern (top red line), difference pattern (bottom blue line), and expected peak positions are shown. The material has a space group $Pm\bar{3}m$ with sites: Ba 1a (0, 0, 0); Sr 1a (0, 0, 0); Co 1b (0.5, 0.5, 0.5); Fe 1b (0.5, 0.5, 0.5); O 3c (0.5, 0.5, 0). The occupancies of Ba, Sr, Co, and Fe were set to 0.5, refined occupancy of O was 0.75 (1) for neutron data and 0.89 (1) for synchrotron data.*

The cubic perovskite structure, space group $Pm\bar{3}m$, was observed at all measured temperatures at pO_2= 0.1 atm. Refined values of displacement parameters and χ^2 for a representative set of neutron and synchrotron data are shown in Table 3.1. Neither additional phases, nor the hexagonal polymorph as proposed by Švarcová et al.[66], were detected in the gathered data sets. Attempts to fit structures involving either A- or B-site cation ordering, such as rock salt $Fm\bar{3}m$ or layered P4/mmm[71], resulted in a splitting of peaks or generation of additional peaks that were not seen in the synchrotron or neutron diffraction patterns. We can thus conclude that the cations are disordered, with Ba/Sr ions randomly occupying the A-site and Fe/Co ions randomly occupying the B-site. The disorder in cation positions required the Ba/Sr as well as the Co/Fe isotropic atomic displacement parameters to be fixed as pairs for both models during refinement.

***Table 3.1**: Cubic, space group $Pm\bar{3}m$, Rietveld fit parameters for BSCF at pO_2 of 10^{-1} atm refined using: (a) neutron data and (b) synchrotron data, with sites: Ba 1a (0, 0, 0); Sr 1a (0, 0, 0); Co 1b (0.5, 0.5, 0.5); Fe 1b (0.5, 0.5, 0.5); O 3c (0.5, 0.5, 0). The occupancies of Ba, Sr, Co, and Fe were set to 0.5, refined occupancy of O was 0.75 (1) for neutron data and 0.89 (1) for synchrotron data.*

a) Pm-3m Neutron 1100K			b) Pm-3m Synchrotron 295K		
a (Å)	4.0389 (1)		a (Å)	3.9728 (1)	
Occ. O	0.75 (1)		Occ. O	0.89 (1)	
χ^2	1.44		χ^2	3.83	
R_P %	9.01		R_P %	8.40	
wR_P %	4.77		wR_P %	10.50	
V (Å^3)	65.884 (4)		V (Å^3)	62.701 (0)	
ρ_c (g/cm^3)	5.178		ρ_c (g/cm^3)	5.618	
Atomic displacement parameters (Å^2)*100			Atomic displacement parameters (Å^2)*100		
	U_{iso}/U_{11}	U_{33}		U_{iso}/U_{11}	U_{33}
Ba/Sr	4.3 (1)		Ba/Sr	2.15 (1)	
Co/Fe	4.6 (1)		Co/Fe	2.40 (1)	
O_{iso}	5.6 (1)		O_{iso}	3.22 (4)	
O_{aniso}	5.9 (1)	5.1(2)	O_{aniso}	3.19 (6)	3.27(9)

The oxygen site occupancy was refined to the values between 0.75 (1), $3-\delta=2.26(2)$, at 1100K and 0.79 (1), $3-\delta=2.36(2)$, at 793 K, as shown in Figure 3.2a, with corresponding lattice parameters ranging from 4.0389 (1) at 1100K to 4.0041 (1) at 793K. Models with oxygen refined using both isotropic and anisotropic atomic displacement parameters were analyzed to determine if allowing anisotropic motion would substantially alter the oxygen site occupancy; however, there was no significant difference in quality of fit parameters between these two models. The refined anisotropic U_{11} and U_{33} values were similar to the refined isotropic value, indicating close to isotropic atomic displacement of oxygen , Figure 3.2b. This is in contrast to the anisotropic oxygen displacement for the cubic perovskite $La_{0.6}Sr_{0.4}Co_{0.8}Fe_{0.2}O_{3-\delta}$ reported by Yashima and Kamioka[72]. Oxygen site occupancies were within a single standard deviation for both isotropic and anisotropic displacement parameters. Figure 3.3 shows the observed Fourier density map for BSCF5555 showing the isotropic oxygen model derived through Rietveld analysis.

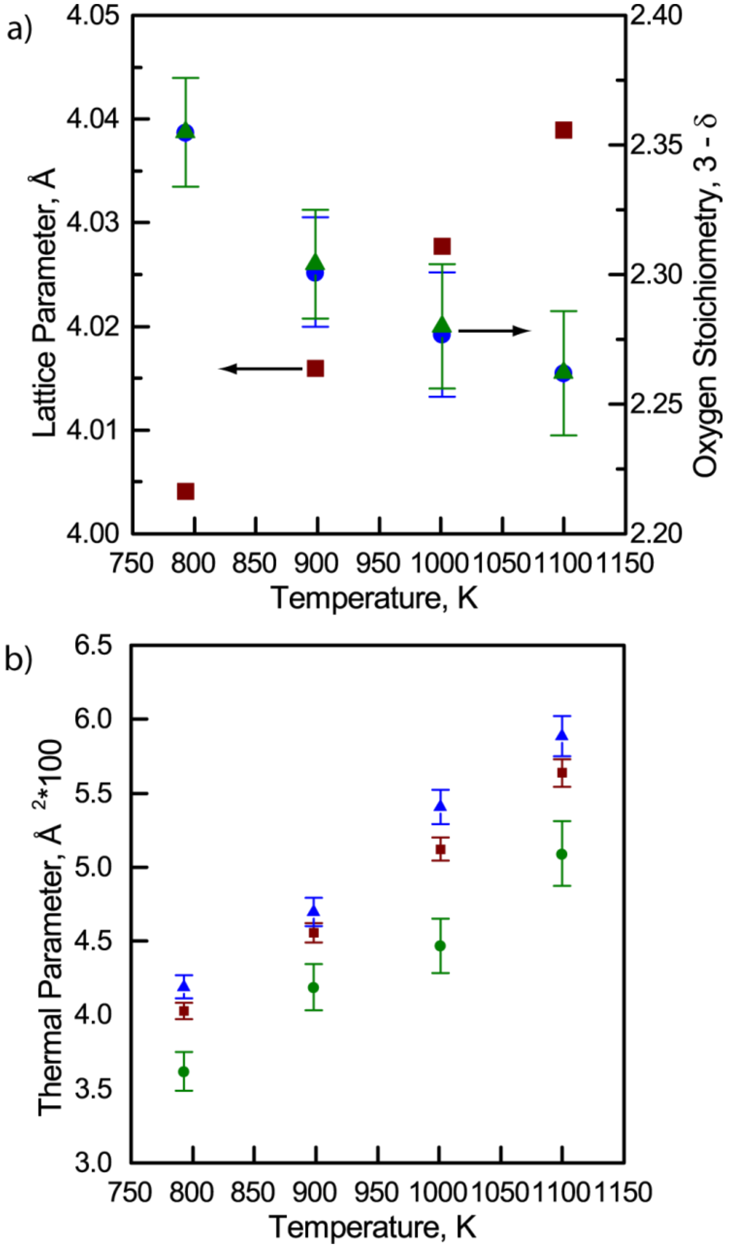

Figure 3.2: *a) Refined lattice parameter (red square), and oxygen stoichiometries for isotropic (green triangle) and anisotropic (blue circle) oxygen versus temperature. b) Oxygen isotropic thermal parameter U_{iso} (red square) compared to anisotropic thermal parameters U_{11},U_{22} (blue triangle) and U_{33} (green circle) with temperature*

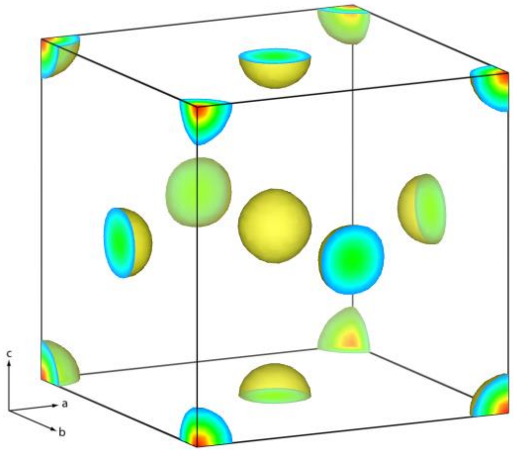

***Figure 3.3**: Observed nuclear density map generated by VESTA[40] from 1100K neutron data*

Values for oxygen stoichiometry in BSCF5555 along with data from the literature for comparison are shown in Figure 3.4. Our refined stoichiometry values are slightly higher than those of McIntosh et al.[42], who reported powder neutron diffraction and thermogravimetric analysis of BSCF5582. The slightly higher oxygen stoichiometry of BSCF5555 is consistent with the higher Fe/Co ratio as Fe is less reducible than Co. In contrast to this agreement, the other previous studies, based on thermogravimetric analysis or coulometric titration, provide a wide range of reported oxygen stoichiometry values for materials of similar composition. If we assume that the TGA instruments used are sufficiently accurate, one potential source of this discrepancy is the calculation of the absolute oxygen stoichiometry, whether by reduction in H_2-rich gas or by iodometric titration. However, the discrepancy seems particularly large for BSCF-based materials.

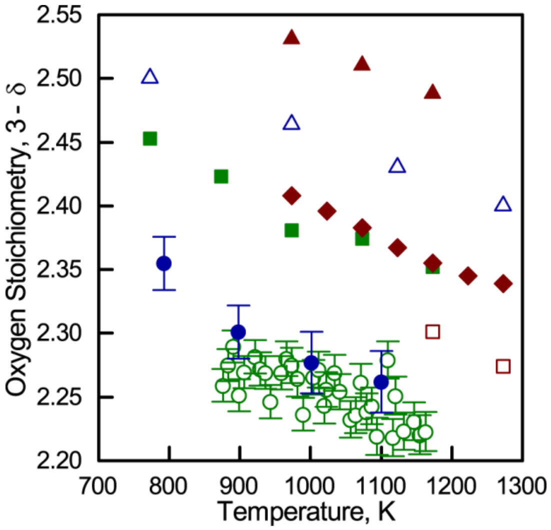

Figure 3.4*: Comparison of oxygen stoichiometry values from literature values for pO_2=0.1 atm. This experiment (closed blue circles), McIntosh et al.[42] (open green circles), Mueller et al.[61] (open red squares), Jung et al.[57] (closed green squares), Švarcová et al.[66] (red diamonds), Kriegel et al.[58] (open blue triangles), Bucher et al.[54] (closed red triangles)*

It is feasible that there is some consistent error in the neutron diffraction data sets and analysis; however, the data presented here is collected on a different diffraction instrument at a different beamline with different sample holder configuration than the previously published data on BSCF5582[69]. The quality of fit parameters in this and the previous study indicate a very good fit to the data, and here we have accounted for any possibility of cation vacancy and the possible influence of oxygen site anisotropy. Sample equilibration in the neutron beam can be a problem due to limited measurement time[8], but we would anticipate that this would lead to an increased oxygen stoichiometry for the first high temperature data point as the sample was previously slowly cooled in air. Previous issues with equilibration have occurred upon cooling with low pO_2 where the kinetics are insufficient to re-oxidize the sample, leading to near constant oxygen occupancy with decreasing temperature. Here we observe a significant increase in oxygen stoichiometry with decreasing temperature, suggesting that sample equilibration was not a problem.

The most likely cause of this discrepancy is the formation of secondary phases in the TGA or coulometric titration cell during measurement. Švarcová et al.[66] first reported the formation of a hexagonal phase of BSCF5582 below 1173K with a cation stoichiometry identical to the bulk cubic phase. Subsequent work by other groups[56,60,62,63] has shown that the hexagonal polymorph is highly enriched in Co and slightly enriched in Ba, with an almost complete absence of Fe. Conversely, the cubic perovskite then becomes enriched in Sr and Fe to balance the overall cation composition. In addition to the hexagonal phase, a plate-like lamellar structure[56,62,63] and a monoclinic structure, which is assumed to be a precursor to the hexagonal phase[53,63,64], have been identified. These additional phases may have an oxygen stoichiometry that is greater than that of the cubic perovskite conformation. First principles calculations performed by Kuklja et al.[59] indicated that the oxygen vacancy formation energy for the cubic phase is significantly less than for the hexagonal phase. This difference in vacancy formation energy would cause the hexagonal phase to have a much higher oxygen stoichiometry than the cubic phase at the same pO_2 and temperature.

The kinetics of the formation of the hexagonal phase were studied by Mueller et al.[60]. They showed that the formation of the hexagonal phase is a decomposition of the original cubic perovskite structure to a Ba/Co enriched hexagonal structure and a Sr/Fe enriched cubic structure. This transition occurs at temperatures below 1123K; however, at lower temperatures the rate decreases until the decomposition effectively stops. At temperatures around 1073K, significant amounts (as much as 12-13%) of the hexagonal phase can form within 24 hours with the phase fraction continuously increasing with time and coming to a maximum of around 50% after several weeks. Thus formation of this secondary phase during the typical long equilibration periods typical for TGA and coulometric titration measurements will cause the reported values to be consistently higher than the actual stoichiometry of the cubic phase. In addition, the wide scatter of these values in the literature can be explained by differing phase fractions of the hexagonal phase being present in the samples.

While the higher stoichiometry values determined through TGA are most likely caused by the formation of the hexagonal phase during measurement, the scatter between the measurements made by different groups may be due to poorly defined and determined reference states. Reducing the BSCF5555 sample in 5% H_2/N_2 for 12h resulted in only partial decomposition of the perovskite structure; the XRD pattern showed the presence of a perovskite phase, BaO, SrO, Fe, and Co. Thus, an assumption of complete reduction to back-calculate the oxygen stoichiometry from the TGA weight change would yield an erroneous result. The XRD pattern of the reduced material is not typically reported in TGA studies, but variations in reduction procedure, leading to similar incomplete reduction, may partially explain the scatter in the reported data.

Many of the issues that complicate oxygen stoichiometry measurements via TGA or coulometric titration do not affect measurements via neutron diffraction. Neutron diffraction yields a direct evaluation of the oxygen site occupancy in the crystal lattice, avoiding errors that occur while determining a reference state. Neutron diffraction also clearly shows the formation of secondary crystalline phases, allowing the determination of oxygen stoichiometry and other relevant structure parameters for all phases present in the sample.

3.4 *Conclusion*

BSCF exhibits the cubic perovskite phase $Pm\overline{3}m$ across the temperature range measured in this study. The oxygen stoichiometry determined by Rietveld analysis of neutron diffraction patterns varied between 2.26(2) at 1100K and 2.36(2) at 793K at pO_2=0.1 atm. These values of oxygen stoichiometry are in good agreement with previous neutron diffraction studies but disagree with those determined by other techniques. This is attributed to secondary phase formation during long equilibration periods in these other studies. Direct determination of crystal structure and oxygen stoichiometry through Rietveld analysis of neutron diffraction patterns avoids these issues.

4 On the Link Between Bulk Structure and Surface Activity of Double Perovskite Based SOFC Cathodes

4.1 *Introduction*

Layered perovskite cobaltites of the series $LnBaCo_2O_{5+d}$ (Ln= Nd (NBCO), Pr (PBCO), Gd (GBCO)) have been investigated by numerous groups as potential materials with high rates of oxygen transport through the oxygen vacancies in the $AA'BO_{5+d}$ crystal structure at intermediate temperatures[8,73-75]. These materials contain significant amounts of oxygen vacancies within the Ln layer, allowing rapid oxygen diffusion through the material.

Typically, oxygen exchange rates are measured using impedance spectroscopy, Isotope exchange depth profiling (IEDP), and electric conductivity relaxation experiments (ECR). These techniques attempt to simultaneously measure both the surface reaction and bulk transport rates. However, as discussed by Cox-Galhotra and McIntosh[1] these techniques have difficulty simultaneously determining both of these values with any degree of reliability. This challenge was addressed by Bouwmeester et al. who proposed an isotopic pulse exchange method to directly measure the oxygen surface exchange rate[44].

A universal link between surface exchange rate and bulk oxygen transport in perovskite structure oxides has been proposed by analysis of data primarily from isotopic depth profiling[76,77]. Independent experimental evidence links one of these parameters to electrochemical performance, and shows a link between bulk structure and surface exchange is limited. An underlying question is whether the bulk structure has any influence on the surface rate, this is especially true when we consider that the bulk surface composition and structure can vary significantly from bulk values; almost all studies on SOFC cathode materials show surface enrichment of A-site cations[78,79].

Herein we utilize an isotopic pulse technique to directly measure the oxygen surface exchange rate on the surface of NBCO, PBCO, and GBCO between 573K and 973K. The results are compared to impedance spectroscopy experiments to identify potential links between the experiments. Finally, the surface of the materials was analyzed using XPS in order to gain a better understanding of the surface composition, a parameter which is directly related to the surface reaction rate.

4.2 ***Experimental***

$NdBaCo_2O_{5+\delta}$ (NBCO), $PrBaCo_2O_{5+\delta}$ (PBCO), and $GdBaCo_2O_{5+\delta}$ (GBCO) powders were synthesized using metal nitrate solutions through a modified Pechini method as described in Section 1.4. The resulting cakes were ground and calcined in air at 1273K (NBCO), 1373K (PBCO), or 1473K (GBCO) for 10h with 5K/min heating and cooling rates. The powders were sieved, with only those particles between the sizes of 106 and 150 µm used in the isotopic pulsing experiment. BET surface areas of the powders were measured (Micromeritics ASAP 2020) using N_2 as the adsorbent. Samples were degassed at 573K for 10h prior to measurement.

Measurements of the surface reaction rate were taken using an isotopic pulse exchange technique, as described in Section 1.8. 100mg of sieved powder was placed in a 4 mm i.d. quartz tube, with the powder held in the center of the tube by plugs of quartz wool. Samples diluted with SrTiO3 (STO) were utilized to measure the reaction rate at temperatures above 723K. To ensure standardized pulse sizes, a computer controlled 6-

way valve with a pneumatic actuator [Swagelok model 131 SR] was utilized with a 500 µL sample loop to create each pulse.

The STO diluent was found to be unreactive with the powder samples within the temperature range of the pulsing experiments. In addition, a set of pulsing experiments conducted with pure STO powder was shown to be unreactive with $^{18}O_2$ below 873K, with reaction rates several orders of magnitude lower than those of NBCO, PBCO, or GBCO, allowing STO to be utilized as an effective diluent to bring total sample conversion down to measureable values at higher temperatures.

Five pulses were measured at each temperature, with the standard deviation between measurements represented as error bars in the data. The pulses were separated by 90s intervals; sufficient time for the measured isotopic fraction to return to baseline values.

The electrochemical performance of the materials as SOFC cathodes was characterized by impedance spectroscopy (Reference 3000, Gamry Instruments, Malvern, Pa, USA). Cerium Gadolinium oxide (CGO, $Gd_{0.2}Ce_{0.8}O_{2.9}$ 99%, American Elements) powder was pressed at 2500lbs in a uniaxial press then sintered for 4 hours at 1623K in air to form dense pellets. Electrodes of equal area, 0.4 cm^2, were painted in the center of each side each side of the electrolyte pellet and sintered at 1373K for 4h. The impedance spectra of the cell were recorded in galvanostatic mode with an AC RMS perturbation of 1mA between 1MHz and 0.1Hz, with ten points collected per decade of frequency. Measurements were performed in laboratory air without DC bias. Each sample was tested at 50K increments from 773K to 1073K.

The surface cation composition was determined using X-ray photoelectron spectroscopy (XPS, Scienta ESCA-300). The samples were heated to their sintering temperatures for 5 hours to clean the surface prior to this measurement. XPS spectra were taken using a monochromatized X-ray from an Al Kα source (E=1486 eV). Quantization of the surface cations was performed using the CASA software package, utilizing the areas of the Ba (4d), Co (3p) and Ln (3d5/2) peaks for calculation. All data was collected at a pass energy of 300 eV. An electron flood gun was used for sample charge neutralization, although a slight shift in peak eV values may have occurred due to net charging.

4.3 ***Results***

NBCO, PBCO, and GBCO powders were characterized by X-ray diffraction, Figure 4.1. The patterns were indexed using the GSAS software package [38,80] and the generated XRD plots compared to the crystal structure data in the literature. NBCO was indexed to the tetragonal *P4/mmm* space group with lattice parameters $a = b = 3.901$ Å and $c = 7.610$ Å and atoms located on their ideal positions. Both PBCO and GBCO were indexed to the orthorhombic *Pmmm* space group[81-83]. PBCO was indexed with unit cell $a = b$ 3.901 Å and $c = 7.628$ Å with atoms on their ideal positions while GBCO was indexed to $a = 3.876$ Å, $b = 7.826$ Å, $c = 7.540$ Å with atom positions as defined previously by Tarancon et al.[83]. All three patterns showed phase pure materials. The sieved NBCO, PBCO and GBCO powders had a BET surface area of 3.776 m^2g^{-1}, 4.435 m^2g^{-1}, and 4.053 m^2g^{-1}, respectively.

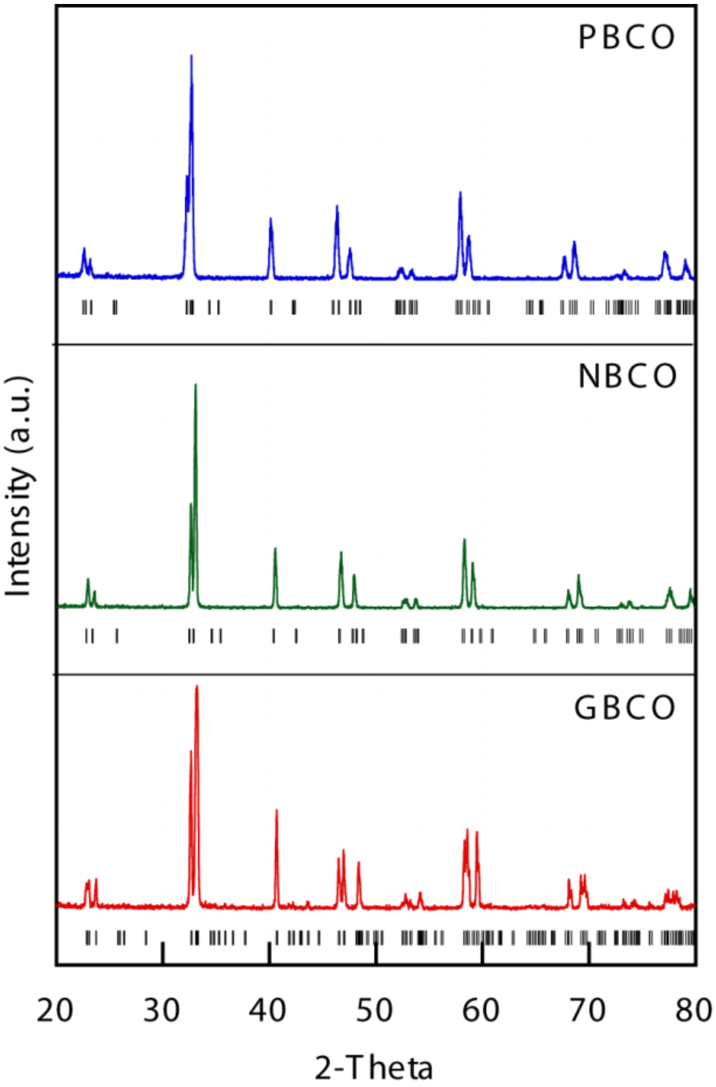

***Figure 4.1**: X-ray diffraction patterns for PBCO (blue), NBCO (green) and GBCO (red). Tick marks indicated expected peak positions extracted from GSAS [38,80].*

Figure 4.2 shows representative data from the isotopic exchange experiments at room temperature and 1023K. At room temperature a sharp $^{18}O_2$ peak is observed with no detectable $^{16}O^{18}O$ signal, indicating an oxygen exchange rate below detectable limits for our experimental system. No change in the size of this $^{18}O_2$ was observed at temperatures below 573K for any of the materials examined. A decrease in intensity of the $^{18}O_2$ peak above this temperature, with associated appearance of a $^{16}O^{18}O$ peak, indicated isotopic oxygen exchange on the sample[44].

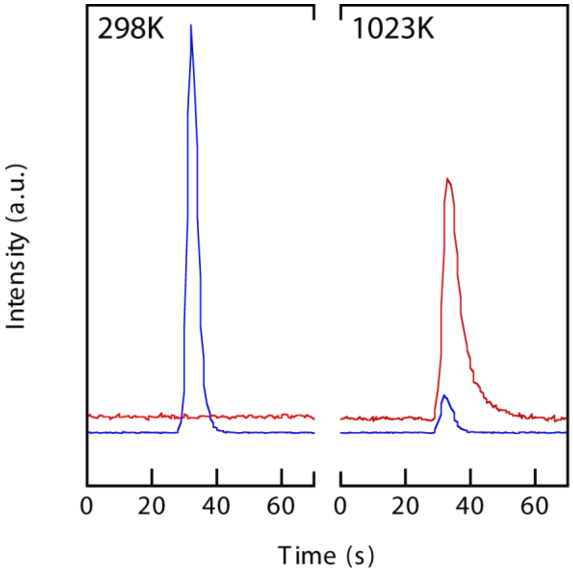

Figure 4.2: *RGA signal for m/z= 34 ($^{16}O^{18}O$, red) and m/z =36 ($^{18}O_2$, blue) for a single $^{18}O_2$ pulse response at 298K and 1023K.*

The overall surface isotopic exchange rate, R_o, for NBCO, PBCO, and GBCO as a function of inverse temperature are shown in Figure 4.3. The rate on NBCO was found to be the greatest with the oxygen exchange rate of PBCO being slightly faster than that of GBCO. The experiment was repeated for multiple samples with the same results, and the figure contains data for both pure double perovskite powders and those diluted with STO. The data collected above 723K is for the diluted samples. The reaction rates calculated for both the pure and STO-diluted samples formed the same Arrhenius relation, proving that the STO dilution did not impact the measured reaction rates in the higher temperature experiments. While the NBCO and PBCO samples show a linear relationship with inverse temperature, there is a discontinuity in the data for GBCO at 798K. All three materials have approximately equal overall activation energies, 80.8, 83.3, and 79.3 kJ/mol for NBCO, PBCO, and GBCO, respectively.

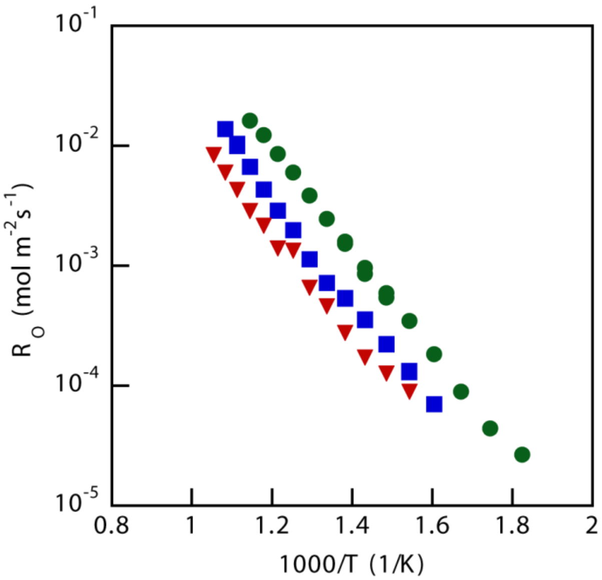

***Figure 4.3**: Arrhenius plot of surface reaction rates derived from $^{18}O_2$ isotopic pulse experiments for NBCO (green circle), PBCO (blue square), and GBCO (red inverse triangle).*

Attempts were made to separate the overall rate of ^{18}O incorporation into surface adsorption and lattice incorporation reaction rates, following the procedure outlined by Bouwmeester and coworkers[44]. We were unable to definitively separate the two rate constants of these competing steps, due to non-unique solutions to fitting two rate parameters to a single set of data; the experimental data could be fit equally well by numerous combinations of the adsorption and incorporation rates. Depending on initial values, the fit would converge with either adsorption or incorporation rate limiting the surface reaction rate, with the other held as significantly higher and therefore insignificant in determining the overall ^{18}O incorporation rate. This led to the focus on the single, overall surface reaction rate in this study.

Representative data for the impedance spectroscopy experiments performed on NBCO, PBCO, and GBCO at 873K are shown in Figure 4.4. The spectra were normalized by the electrode area and divided by two to yield the impedance of a single electrode. The area specific resistance (ASR) of the electrodes was calculated as the total span of the resulting semicircular arcs. Each impedance arc was formed of a large, lower frequency arc as well as several overlapping higher frequency arcs. The natural log of the ASR is plotted against inverse temperature in Figure 4.5. While the ASR values of PBCO and GBCO were approximately equivalent across the entire temperature range, the ASR for the NBCO based electrode was lower 1023K. The convergence of ASR values for each material at the higher temperatures is due to the decreasing span of the lower frequency arc; the process leading to the higher frequency arcs dominates the ASR values and is similar for all materials

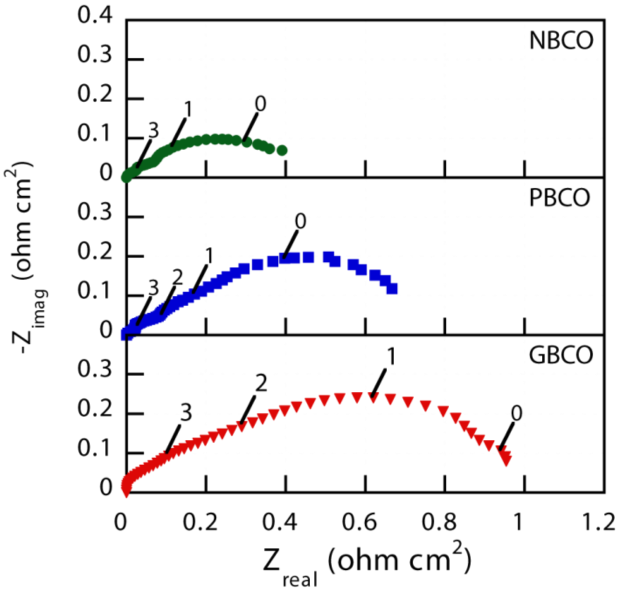

***Figure 4.4**: Impedance spectra (electrolyte resistance subtracted) measured for NBCO (green circle), PBCO (blue square), and GBCO (red inverse triangle) based in electrodes in air at 873K. Labeled points denote frequency in decades of 10^n Hz.*

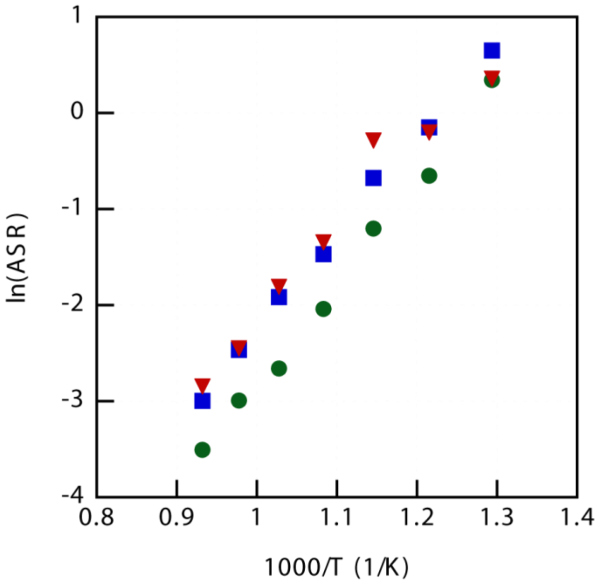

Figure 4.5*: Area specific resistance (ASR) for NBCO (green circle), PBCO (blue square), and GBCO (red inverse triangle) based electrodes in air.*

As with the surface exchange rate data, the impedance data for GBCO shows a discontinuity. This discontinuity was present for all GBCO cells tested as part of this study. Activation energies were calculated by taking the span of the dominant low frequency arc, yielding values of 87.9 kJ/mol, 83.0 kJ/mol, and 84.6 kJ/mol for NBCO, PBCO, and GBCO respectively. The span of the dominant arc was taken to represent the dominant rate limiting process in the electrode.

The surface composition shows some enrichment of Ba on the surface of the NBCO, PBCO, and GBCO. Regions used for the quantitative analysis of the surface include Ba(3p) from 1040-1080 eV, Co(3p) and Ba(4d) from 55-105 eV, and O(1s) from 520-550 eV. The most intense peaks for Co(2p) and Ba(3d) lie too close together for quantitative analysis and thus other peaks were utilized. The cations on the surface of the NBCO and GBCO were enriched to an approximately 1:4:2.3 ratio of Ln:Ba:Co respectively, with the

PBCO having a slightly higher concentration of lanthanide on the surface, possessing a ratio of 1:1.8:1.

4.4 *Discussion*

The surface reaction rates for NBCO, PBCO, and GBCO found in this work compare favorably to the most active cathode materials $Ba_{0.5}Sr_{0.5}Co_{0.8}Fe_{0.2}O_{3-\delta}$ (BSCF) and $La_2NiO_{4+\delta}$ studied by Bouwmeester et al. [44]. The rates measured for NBCO are comparable to those reported for BSCF, with the rates of PBCO and GBCO still significantly above those for $La_2NiO_{4+\delta}$. These rapid surface reaction rates show the potential for layered cobaltites, most notably NBCO, as cathode materials for IT-SOFC application.

The surface reaction activation energies are also in good agreement with literature from measurements made by a range of other techniques. Taskin et al.[84] a value of 82.0 kJ/mol and Tarancón et al.[73] report 78.1 kJ/mol for GBCO. Other groups have proposed a range of activation energies from 74 kJ/mol to 118 kJ/mol[85-88]. Similarly, for PBCO, Liu et al.[6] reported an activation energy of 74.3 kJ/mol on highly epitaxial thin films and Cox-Galhotra et al.[78] found a similar value of 83.9 kJ/mol. No literature values directly agreeing with our activation energy for NBCO were found, with Yoo et al.[5] reporting 106 kJ/mol; however, it seems unlikely that the activation energy would differ so greatly for this one material. This agreement with literature suggests that the measurement technique reported here is reliable.

Both the impedance and surface rate data show similar trends for the relative performance of the three materials examined. The high surface rate of NBCO corresponds with the lowest ASR for the NBCO based electrode, with PBCO and GBCO showing similar values for each parameter.

Furthermore, the activation energies derived both sets of data show less than 7% difference for all three materials. This discrepancy can be attributed to the difficulty in extracting the ASR from the low frequency arc with the multiple overlapping high frequency arcs. We hypothesize that the match in performance trend and similarity of activation energies is one piece of evidence that the surface reaction is the rate limiting process for these SOFC cathodes below 1073K. We further propose that the low frequency arc in the impedance spectra is dominated by the surface reaction.

This identification of surface rate dominated electrode performance is not unique for these materials. For example, numerous studies have reported that the performance of $La_{1-x}Sr_xMnO_{3-\delta}$ electrodes is strongly dependent on the surface composition[89,90], with surface enrichment of Sr under operation leading to significant changes in electrode performance. In this case, we observe some enrichment of Ba on the surface of all of the materials. This is similar to the report by Cox-Galhotra and McIntosh [78], who observed surface enrichment of Pr and Ba on PBCO. They were unable to distinguish between these two elements due to overlapping peaks in the measurement.

The extent of surface enrichment is important; in the current case, while Ba is enriched on the surface, the surface fraction cation concentration is less than the >90% coverage observed by Shin and McIntosh on proton conducting barium zirconates[45]. In this latter case, the high surface coverage of Ba across samples led to surface reaction rates that were independent of bulk properties. In our case we suggest that the Ba surface cation coverage, always less than 70% compared to a theoretical 25%, is sufficiently low that the bulk composition still influences the surface reaction rate. With significant amounts of Co and more importantly the lanthanide present on the surface, these elements clearly play a role in the surface reaction as evidenced by the differing rates for the materials.

Close examination of both the surface exchange rate data and the impedance data for GBCO show a discontinuity at around 798K. Both sets of data in this temperature range are plotted together in Figure 4.6. We suggest that this discontinuity is due to a phase transition from orthorhombic *Pmmm* to tetragonal *P4/mmm* that has observed using high temperature XRD to occur between 723K and 773K[83,91]. Both the temperature difference for this discontinuity between our two measurements, and the wide range of temperatures reported in the literature for the phase transition, is likely due to differences in thermocouple placement and equilibration time.

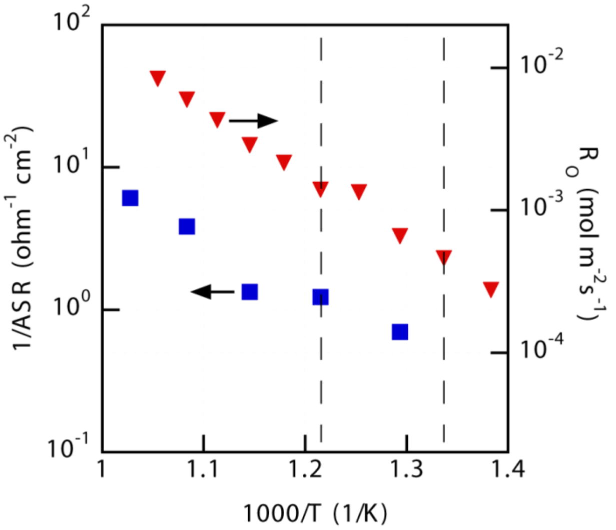

***Figure 4.6**: Comparison of surface oxygen exchange rate (R_0, red inverse triangle) and inverse of area specific resistance (ASR, blue square) for GBCO. Dashed lines denote the reported temperature for the P4/mmm to Pmmm phase transition*[83,91].

The influence of this phase transition on both surface rate and electrochemical performance again suggests that the surface exchange rate controls electrode performance and that the surface rate is directly influenced by the bulk structure. The similar activation energies above and below the phase transition indicate that the rate limiting step is the same for both crystal structures.

The question then arises as to the nature of the link. A strong, and universal, correlation between surface kinetics and bulk ion transport has been reported to hold for a wide range of perovskite structure materials[76,77]. We suggest that this link may be through the oxygen vacancy concentration. NBCO has both a higher oxygen vacancy concentration and shorter direct distance for oxygen transport within the crystal than PBCO, as demonstrated by the work of Cox-Galhotra et al.[7,8]. Furthermore, the phase transition for GBCO is accompanied by a decrease in oxygen stoichiometry ($5+\delta$)[87], and, as reported here, an increase in rate. Further work is required to determine if this increase in vacancy concentration facilitates the surface dissociation of oxygen or a subsequent incorporation step.

Differences in extent of Ba or other element surface segregation may be the reason that other groups have not shown the same influence of the GBCO phase change on the electrochemical behavior of the cathode. If the surface is rate limiting, and this surface is covered in Ba, we may expect that the bulk structure would have little influence on electrochemical performance. The extent of surface segregation will be a strong function of sample history. Unfortunately we cannot prove this hypothesis as, to our knowledge, there are no other reports that include both electrochemical performance and surface composition analysis.

4.5 *Conclusion*

NBCO, PBCO, and GBCO based SOFC cathodes are indicated to be surface reaction rate limited, with a reaction rate that is dependent on the bulk properties of the oxide. NBCO was shown to have the highest reaction rate, approximately half an order of magnitude above those of PBCO and GBCO. A phase transition from Pmmm to P4/mmm for GBCO linked to a discontinuity in both surface oxygen exchange rate and electrochemical performance. Analysis of the surface of the materials with XPS showed an enrichment of Ba.

5 Oxygen Transport Pathways in Ruddlesden-Popper structured oxides revealed via in situ neutron diffraction

5.1 *Introduction*

One promising class of materials is the Ruddlesden-Popper family with general formula $A_{n+1}B_nO_{3n+1}$[7,8,44,61,69,75,92,93]. These materials have been shown to possess high rates of ionic conductivity for O^{2-} anions. Transport mechanisms involving mobile oxygen interstitials have been shown to exist for Ruddlesden-Popper materials such as those with the composition Ln_2NiO_{4+d}[94-99], while other Ruddlesden-Popper structures exhibit the vacancy hopping mechanism similar to the cubic perovskites[9,22,100,101] Herein, we study a series of Ruddlesden-Popper structured materials, utilizing varying ratios of La/Sr in the A-site and Co/Fe in the B-site to form the n=1, n=2, and n=3 analogs with compositions $LaSrCo_{0.5}Fe_{0.5}O_{4-\delta}$ (RPn1), $La_{0.3}Sr_{2.7}CoFeO_{7-\delta}$ (RPn2), and $LaSr_3Co_{1.5}Fe_{1.5}O_{10-\delta}$ (RPn3), respectively. A visualization of the three Ruddlesden-Popper structures considered in this study is shown in Figure 5.1.

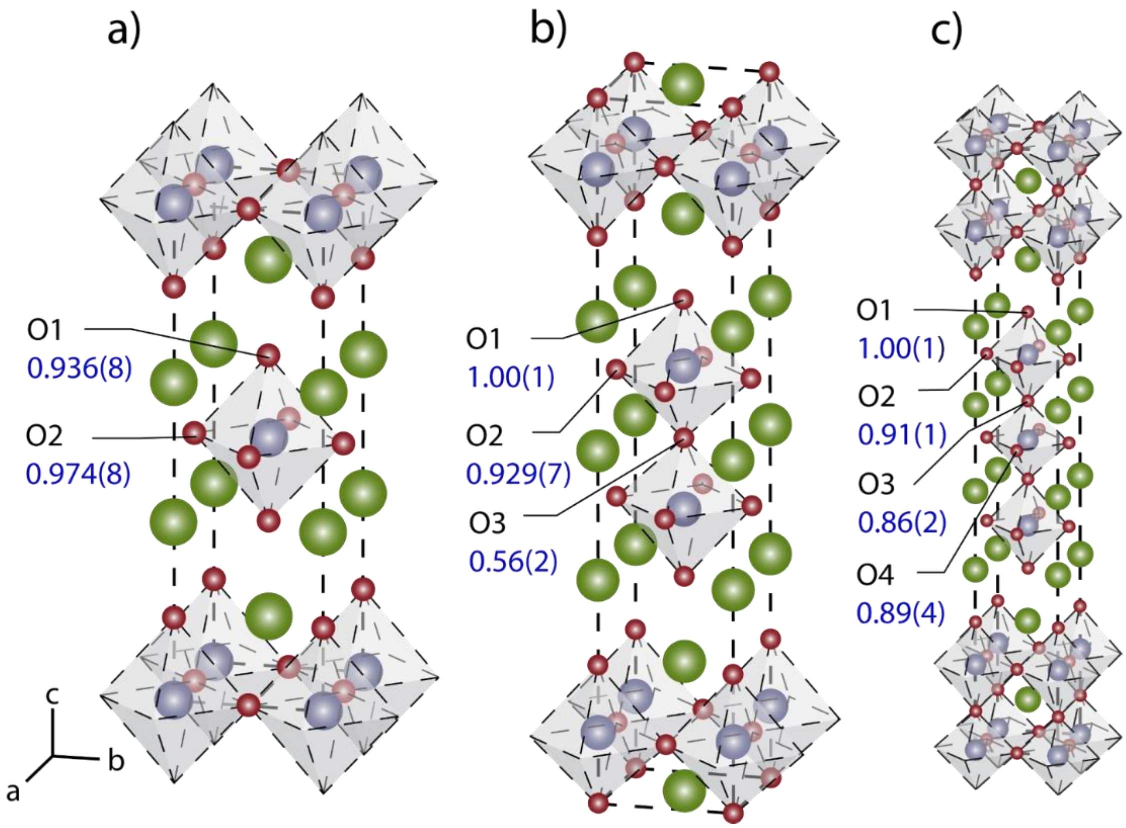

***Figure 5.1**: Ruddlesden-Popper unit cells for a) n = 1 (RPn1), b) n = 2 (RPn2), and c) n = 3 (RPn3) structures. Note that these structures are derived from Rietveld refinement of the neutron diffraction data collected at 1070 K and pO_2 of 0.1 atm. Numbers in blue denote refined oxygen site occupancy at these conditions.*

The ionic conductivity of oxygen deficient MIEC materials occurs through an oxygen vacancy hopping mechanism[102]. Thus the accurate determination of the concentration, location, and mobility of oxygen vacancies in the crystal lattice is essential to understand the ionic transport properties of these materials. The bulk ionic conductivities[9] and surface oxygen exchange rates[103] of the three Ruddlesden-Popper compositions have been measured previously, showing trends of RPn3 ≳RPn2 >> RPn1 and RPn2 ≳RPn3 >> RPn1 respectively. This work seeks to utilize *in-situ* neutron diffraction to identify oxygen exchange pathways within the materials and to link this with the ionic conductivity of each composition.

High temperature *in-situ* neutron powder diffraction can simultaneously determine detailed information about the crystal symmetry, lattice parameters, and atomic positions, occupancies, and displacement parameters of both the cations and anions in these materials[7,8,33-35,42,43,69,103]. Our group has previously demonstrated the efficacy of this technique for both cubic perovskite structured oxides[33,34] and layered perovskite structures[7,8]. The detailed information thus obtained allows prediction of the ionic transport pathways through these materials[7,8] and, in an increasing number of cases, the inferred ionic mobility has previously correlated directly with measured surface oxygen exchange rates[24,34,103].

5.2 ***Experimental***

Synthesis of phase pure samples of n=1, n=2, and n=3 Ruddlesden-Popper phases with identical La/Sr and Co/Fe ratios was not feasible due to phase instability. Attempts to synthesize these materials yielded a mixture of Ruddlesden-Popper, perovskite, and simple oxide phases. Materials with identical Co/Fe ratios but varying La/Sr ratios were synthesized based on similar compositions reported in the literature[9,104]. A tolerance factor for the n = 1 Ruddlesden-Popper phases can be calculated based on the work of Sharma and Singh[105]. Compositions were chosen to achieve n=1 tolerance factors of approximately 1.08, corresponding to a tetragonal *T* phase K_2NiF_4-type structure. $LaSrCo_{0.5}Fe_{0.5}O_{4-\delta}$ (RPn1), $La_{0.3}Sr_{2.7}CoFeO_{7-\delta}$ (RPn2), and $LaSr_3Co_{1.5}Fe_{1.5}O_{10-\delta}$ (RPn3) were synthesized as single phases with only minor presence of single perovskite impurity phases.

All materials were synthesized using metal nitrate solutions in a modified Pechini method, Section 1.4. The resulting cake was then ground into powder and then calcined in air at 1623 K for 10 hours. The finalized powder samples were characterized by X-ray diffraction [Rigaku Miniflex II, Texas, USA] to verify phase purity.

Neutron diffraction patterns were collected at 1070 K, 967 K, 865 K, and 765 K in the d-spacing range of 0.45 – 5.35 Å until a total accelerator source proton charge of 9.0 x 10^{12} pC (~2 hour measuring time) was reached.

Rietveld[37] refinements were performed on the diffraction patterns using the GSAS package[38] with the EXPGUI interface[39]. The profile was modeled using an extended form of the profile function originally derived by Von Dreele, Jorgensen, and Windsor[106] to account for Lorentzian broadening. Decisions regarding which parameters to refine, for example whether atomic displacement should be isotropic or anisotropic, were made with regard to significant changes in the cumulative χ^2 value.

It should be noted that for the RPn2 and RPn3 structures, the multiple A-sites within the unit cell could allow for the A-site in the rock salt to have a different composition from the stoichiometric ratio. Furthermore, the similar coherent neutron scattering lengths of La and Sr, at 8.24 and 7.02 respectively, make it difficult to distinguish between the two in neutron diffraction experiments. Attempts to refine the site occupancy for the multiple A-sites from the neutron diffraction patterns yielded results showing that all sites had similar compositions within standard deviation, and thus the ratios of the cations composing the A-sites were fixed at the stoichiometric ratios. Refinement of the La/Sr ratio using synchrotron X-ray data was unsuccessful due to the formation of additional phases at room temperature.

5.3 *Results*

Neutron diffraction patterns were collected for the three prepared Ruddlesden-Popper phases, Figure 5.2. All three samples were fit to a tetragonal structure, space group *I4/mmm*. Less than 4 wt-% of a cubic perovskite impurity (space group $Pm\bar{3}m$) was identified in each sample, with positions denoted by an asterisk in Figure 5.2. Refined values of all parameters and χ^2 for neutron data collected at 1070 K for all three phases are shown in Table 5.1 - Table 5.3. The same parameters were refined at each temperature. The fit quality was not improved for any of the materials either by ordering of the A-sites and/or the B-sites or by allowing significant deviations in overall composition from the as-synthesized target values. The cation occupancies at each site were therefore fixed to their stoichiometric ratios. No evidence of a phase change was identified in any of the Ruddlesden-Popper structures examined between 765 K and 1070 K.

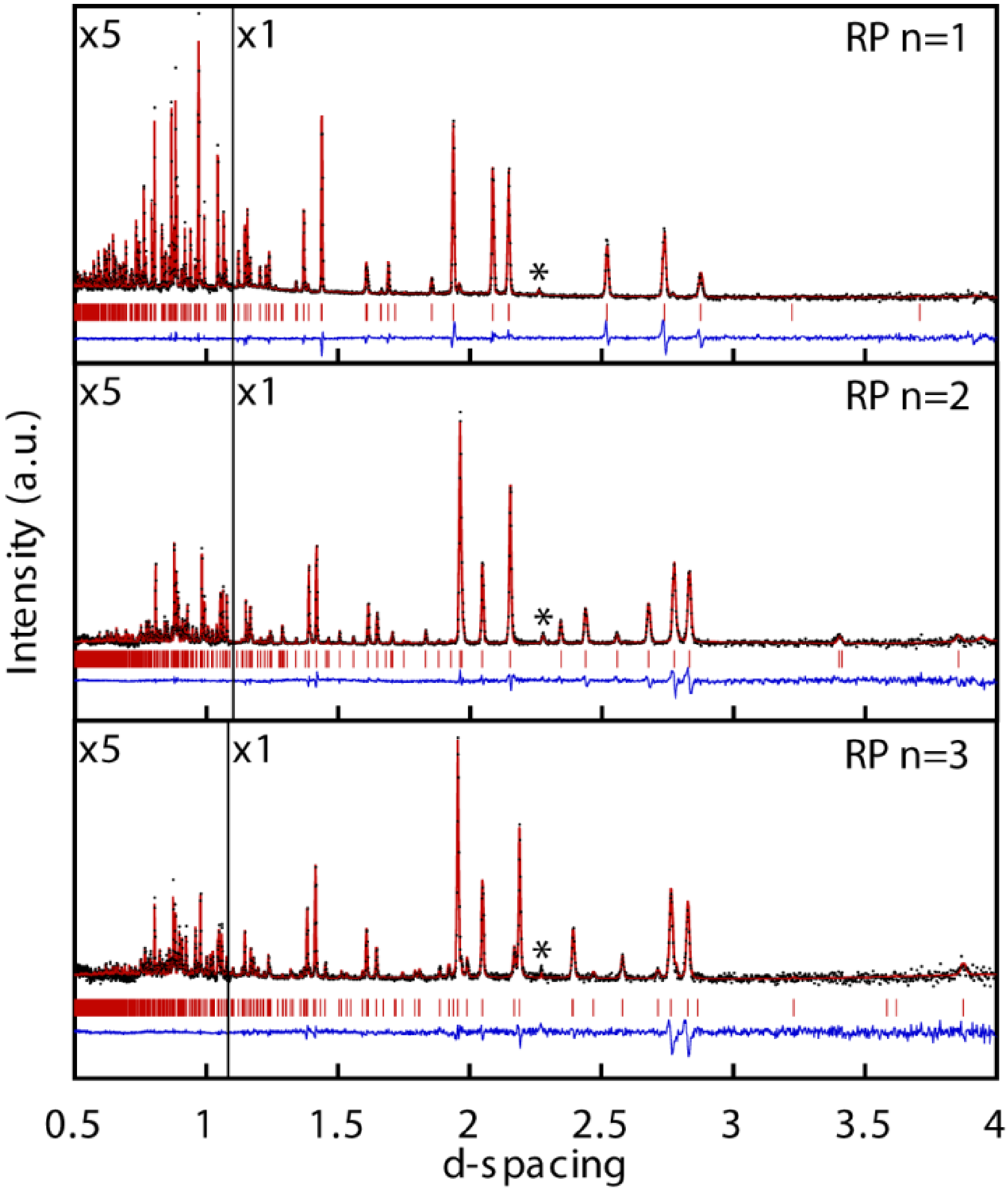

***Figure 5.2**: Representative data from neutron diffraction at 1070 K with a pO_2 of .1 atm for a) $LaSrCo_{0.5}Fe_{0.5}O_{4-\delta}$ (RPn1), b) $La_{0.3}Sr_{2.7}CoFeO_{7-\delta}$ (RPn2), and c) $LaSr_3Co_{1.5}Fe_{1.5}O_{10-\delta}$ (RPn3) samples. All three materials exhibited I4/mmm space group structures. A perovskite ($Pm\bar{3}m$) impurity was identified in each sample, with the primary diffraction peak marked by an asterisk below. Measured data (black dots), calculated diffraction pattern (top red line), difference pattern (bottom blue line), and expected peak positions are shown.*

Table 5.1: Tetragonal space group I4/mmm, Rietveld fit parameters for RPn1 structure at 1070 K with sites: La/Sr1: 4e (0,0,Z), Co/Fe1: 2a (0,0,0), O1: 4e (0,0,Z), O2: 4c (0.5,0,0)

RPn1 I4/mmm 1070 K

a,b (Å)	3.873(1)	χ^2	4.060
c (Å)	12.887(1)	R_P %	0.0974
V (Å^3)	193.58(1)	wR_P %	0.0392
ρ_c (g/cm^3)	5.929		

	Atomic displacement parameters (Å^2)*100				Fractional
	U_{11}/U_{iso}	U_{22}	U_{33}	Z	Occupancy
La/Sr1	2.16(3)			0.359(1)	
Co/Fe1	1.71(4)				
O1	3.88(7)	3.88(7)	1.8(1)	0.167(1)	0.936(8)
O2	0.97(7)	2.9(1)	3.7(1)		0.974(8)

Table 5.2: Tetragonal space group I4/mmm, Rietveld fit parameters for RPn2 structure at 1070 K with sites: La/Sr1: 4e (0,0,Z), La/Sr2: 2b (0,0,0.5), Co/Fe1: 4e (0,0,Z), O1: 4e (0,0,Z), O2: 8g (0,0.5,Z), O3: 2a (0,0,0)

RPn2 I4/mmm 1070 K

a,b (Å)	3.923(1)	χ^2	4.036
c (Å)	20.464(1)	R_P %	0.1499
V (Å^3)	314.97(1)	wR_P %	0.0596
ρ_c (g/cm^3)	5.203		

	Atomic displacement parameters (Å^2)*100				Fractional Occupancy
	U_{11}/U_{iso}	U_{22}	U_{33}	Z	
La/Sr1	3.20(7)			0.317(1)	
La/Sr2	2.80(9)				
Co/Fe1	2.08(5)			0.101(1)	
O1	4.13(8)			0.196(1)	1.0
O2	3.9(1)	2.0(1)	5.0(2)	0.090(1)	0.929(7)
O3	5.5(4)				0.56(2)

Table 5.3: Tetragonal space group I4/mmm, Rietveld fit parameters RPn3 structure at 1070 K with sites: La/Sr1: 4e(0,0,Z), La/Sr2: 4e (0,0,Z), Co/Fe1: 4e (0,0,Z), Co/Fe2: 2a (0,0,0), O1: 4e (0,0,Z), O2: 8g (0,0.5,Z), O3: 4e (0,0,Z), O4: 4c (0,0.5,0)

RPn3 I4/mmm 1070 K

a,b (Å)	3.909(1)	χ^2	2.381
c (Å)	28.675(1)	R_P %	0.1431
V (Å^3)	438.29(2)	wR_P %	0.0541
ρ_c (g/cm^3)	5.455		

	Atomic displacement parameters (Å^2)*100				Fractional
	U_{11}/U_{iso}	U_{22}	U_{33}	Z	Occupancy
La/Sr1	3.3(1)			0.2011(2)	
La/Sr2	3.5(1)			0.0713(2)	
Co/Fe1	2.0(1)			0.1416(1)	
Co/Fe2	3.7(2)				
O1	4.7(2)			0.2120(2)	1
O2	2.3(1)			0.1382(2)	0.91(1)
O3	6.0(4)	6.0(4)	3.1(4)	0.0646(3)	0.86(2)
O4	18.1(2)	1.8(6)	21(2)		0.89(4)

The *a* and *c* lattice parameters as a function of temperature for all three samples are shown in *Figure 5.3* and Figure 5.4, respectively. The RPn2 phase has the largest *a*-axis lattice parameter, followed by the RPn3 and RPn1 samples. This is the expected trend based on the variation of average cation radius between these phases, with substitution of the larger Sr^{2+} cation for La^{3+} resulting in a larger *a* parameter. The average B-site cation oxidation state, and therefore B-site ionic radii, will also influence the lattice parameters. The calculated average B-site oxidation states vary in the ranges 3.0-2.64, 3.38-3.12, and 3.67-3.08 from 500-800 ^{o}C for the RPn1, RPn2, and RPn3 phases, respectively.

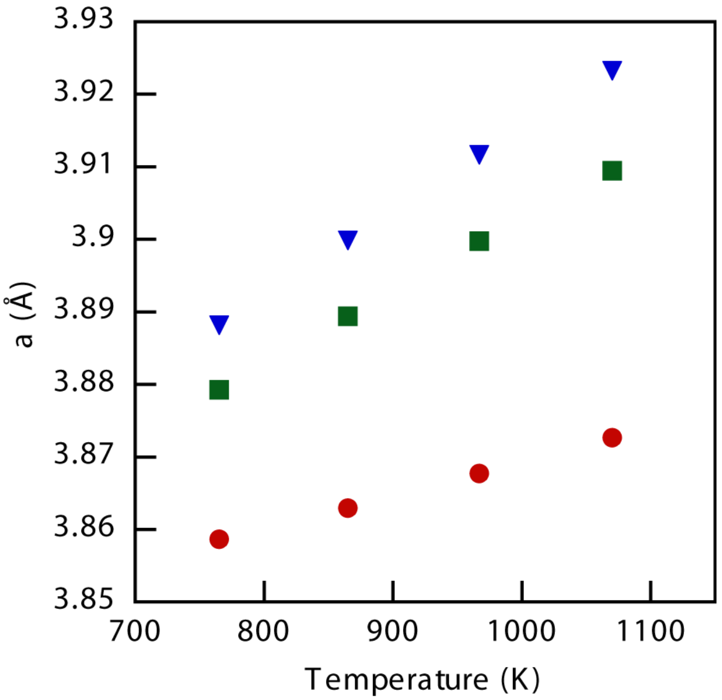

Figure 5.3: *a lattice parameter for RPn1 (Red circle), RPn2 (Blue inverted triangle), RPn3 (Green square).*

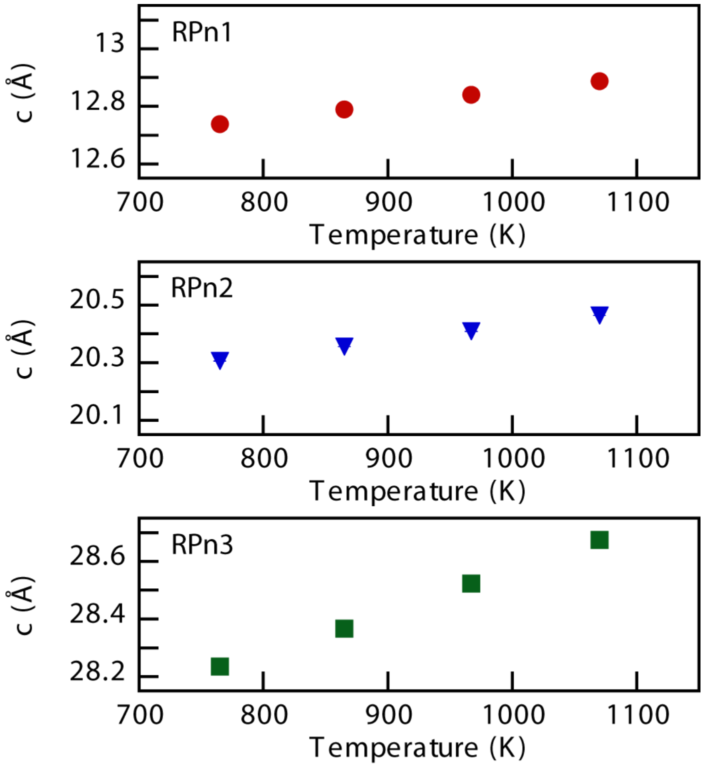

Figure 5.4*: c lattice parameter for RPn1 (Red circle), RPn2 (Blue inverted triangle), RPn3 (Green square).*

The simultaneously varying Ruddlesden-Popper structures, A-site ratios, and oxygen stoichiometries make it difficult to deconvolute the impact of each parameter on the lattice parameter. Previous research has shown that for an n=1 material of similar composition, the *a* lattice parameter is less responsive to temperature change than the *c* lattice, as the *c* axis expansion is less restricted by the expansion of the rock-salt layers[107]. Out of the materials examined, the n=1 and n=3 structures follow this trend identically, however the n=2 phase shows a greater expansion along the *a* axis than along the *c* axis. This is expected to be due to the conflicting thermal and chemical expansion along the *c* axis, as while thermal expansion occurs with increasing temperature, the presence of the heavily vacant O3 site of the n=2 structure causes a compression of the center perovskite cell with increasing temperature, evidenced by a shift of the Co1/Fe1 site towards the center of the unit cell. This decreases the expansion that may be expected along the *c* axis, while having little effect on the *a* lattice expansion. A similar effect was previously observed for PBCO and NBCO perovskite materials[7,8].

Fourier density maps were generated with GSAS for each of the three samples at 1070 K to gain information about the motion and preferred oxygen transport pathways within the materials, Figure 5.5 - Figure 5.7. These figures show the observed nuclear density at both metal cations and anionic oxygen sites within the Ruddlesden-Popper unit cell. The progression of color from blue to green to red denotes an increase in the observed nuclear density, showing the probable positions of the atoms. The three figures represent isosurface levels of 0.45, 0.4, and 0.555, corresponding to 3.8%, 4.2%, and 5.3% of the maximum density, respectively.

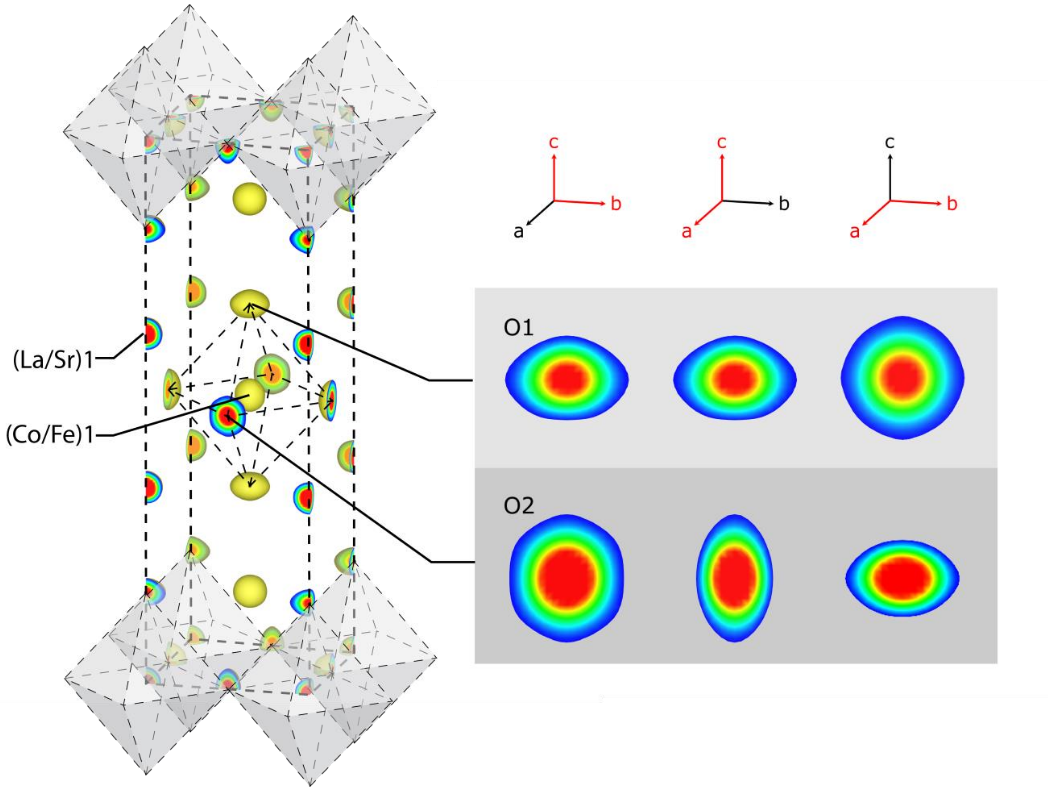

Figure 5.5*: Fourier observed nuclear density diagram at 1070 K with a pO_2 of .1 atm for LaSr$Co_{0.5}Fe_{0.5}O_{4-\delta}$ (RPn1). The progression of color from blue to green to red denotes an increase in the observed nuclear density, showing the probable positions for the atoms. Slices of the observed nuclear density along several different planes are shown for the different oxygen sites.*

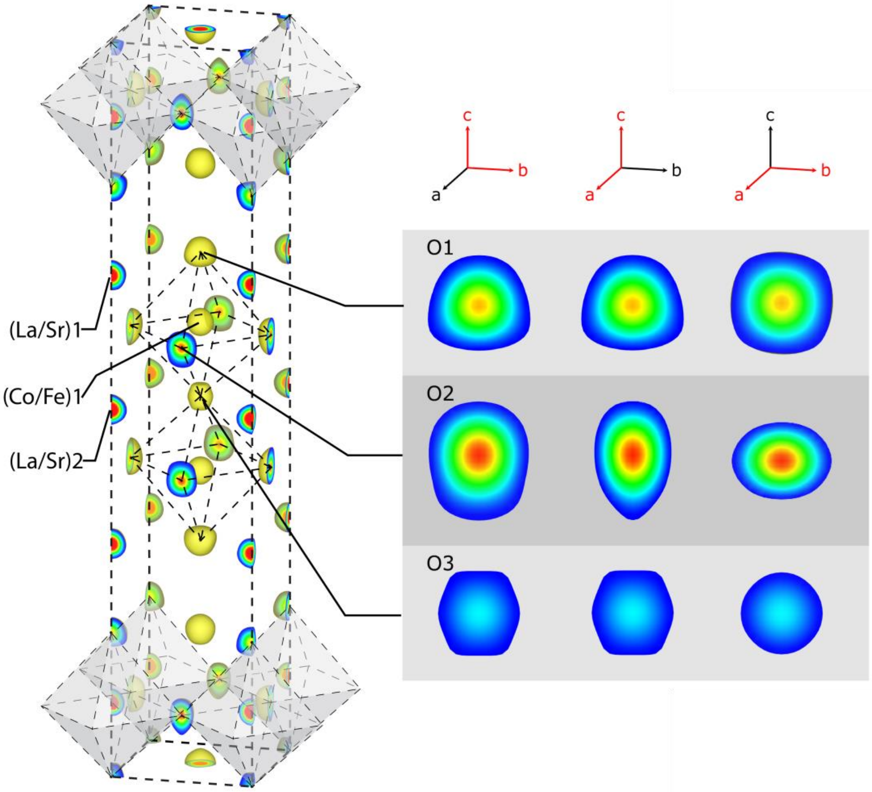

Figure 5.6*: Fourier observed nuclear density diagram at 1070 K with a pO_2 of .1 atm for $La_{0.3}Sr_{2.7}CoFeO_{7-\delta}$ (RPn2). The progression of color from blue to green to red denotes an increase in the observed nuclear density, showing the probable positions for the atoms. Slices of the observed nuclear density along several different planes are shown for the different oxygen sites.*

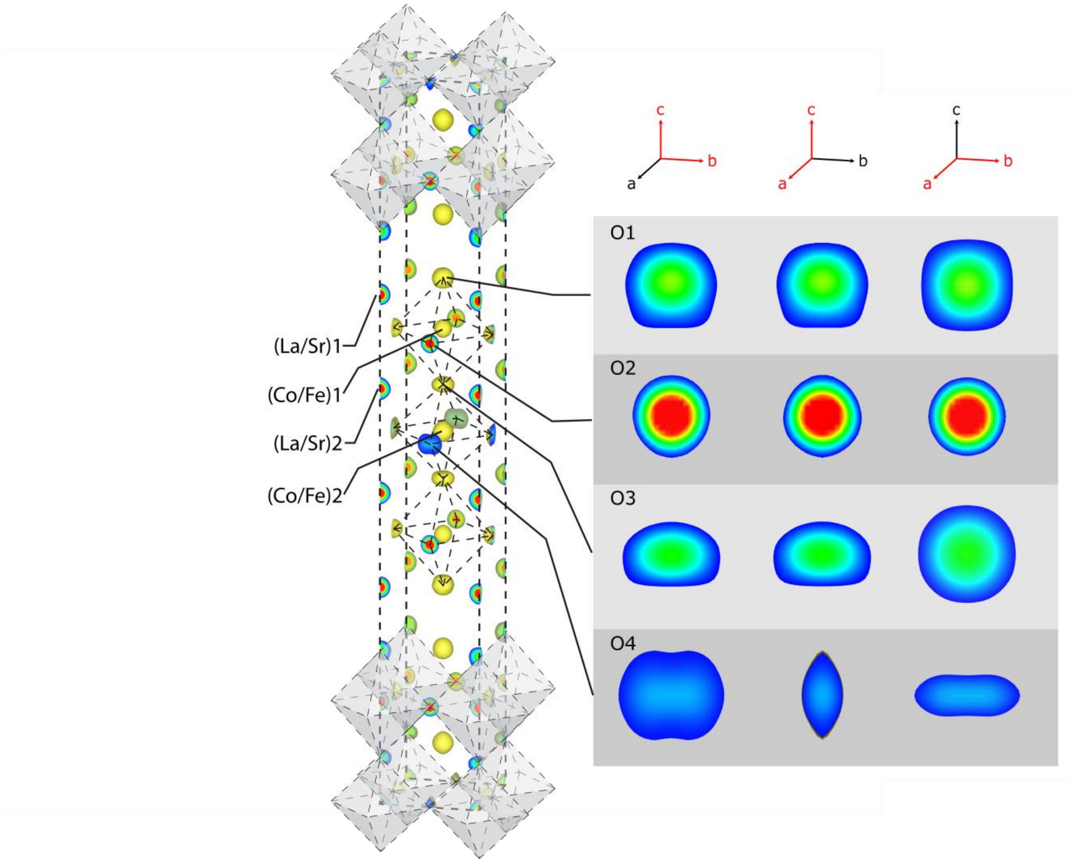

***Figure 5.7**: Fourier observed nuclear density diagram at 1070 K with a pO_2 of .1 atm $LaSr_3Co_{1.5}Fe_{1.5}O_{10-\delta}$ (RPn3). The progression of color from blue to green to red denotes an increase in the observed nuclear density, showing the probable positions for the atoms. Slices of the observed nuclear density along several different planes are shown for the different oxygen sites.*

No evidence for oxygen interstitials was observed for any of the materials, evidenced by the lack of nuclear density outside of the expected crystallographic sites. Ruddlesden-Popper phases with compositions such as $La_2NiO_{4+\delta}$ have been shown to contain oxygen interstitials as part of an interstitial mediated oxygen transport mechanism[93]. As with related neutron diffraction studies, we find no evidence for the existence of oxygen interstitials within an oxygen deficient material[108].

The oxygen sites within $LaSrCo_{0.5}Fe_{0.5}O_{4-\delta}$ (RPn1), Figure 5.5, were found to be close to fully occupied below 967 K; oxygen occupancies refined to values within a standard deviation of 1.0 were therefore held constant at full occupancy, Figure 5.8a. The first measureable vacancies are located at the O2 site, the equatorial site in the perovskite layer, at 967 K. The O1 site, located in the rock-salt layer, was found to be fully occupied until 1070 K where an oxygen occupancy of 0.974(8), slightly outside of the standard deviation from 1.0, was determined. These results are in line with previous findings on related Ruddlesden-Popper structures[107,109]. The atomic displacement parameters for the oxygen atoms were best fit with an anisotropic model, Table 5.1, with preferential displacement perpendicular to the central B-site of the perovskite octahedron. For the O1 site at 1070K, $U_{11}=U_{22}>2U_{33}$; for the O2 site, $U_{33}>1.25U_{22}\sim 3U_{11}$. These distortions in local nuclear density are illustrated as the observed non-spherical nuclear density in the Fourier map, Figure 5.5.

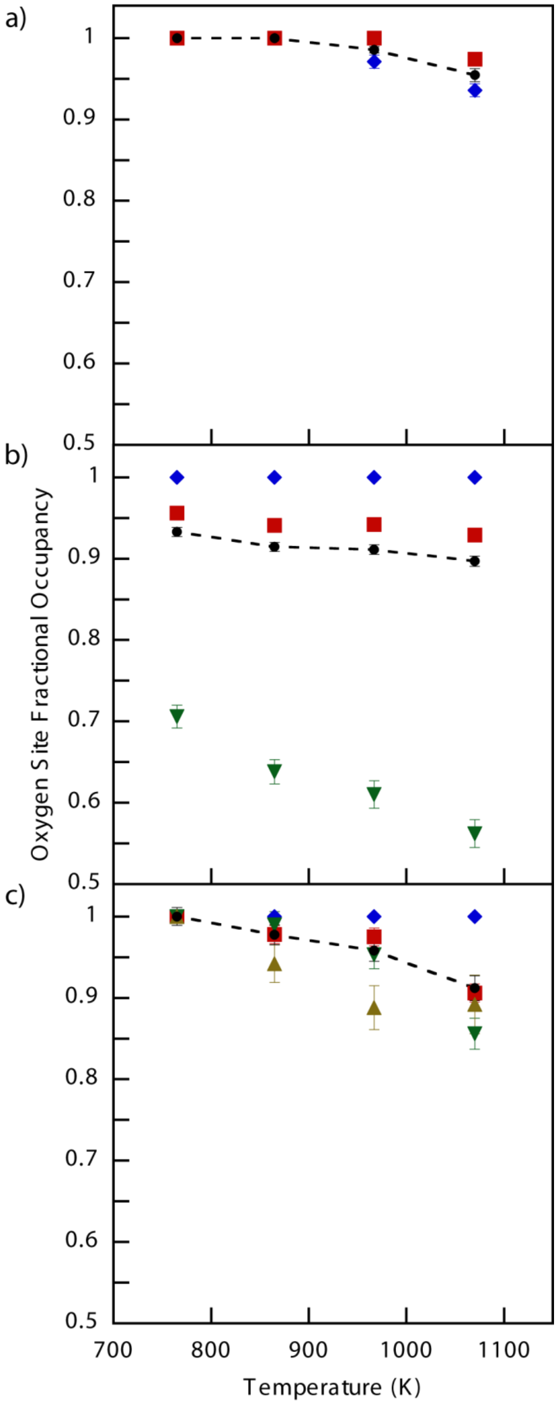

Figure 5.8: *Oxygen site occupancies for a)RPn1, b)RPn2, and c)RPn3 phases. Sites displayed include O1 (blue diamond), O2 (red square), O3 (green inverted triangle), and O4 (gold triangle). Overall oxygen occupancy at each temperature is denoted by black circles connected by the dashed line.*

In contrast, the $La_{0.3}Sr_{2.7}CoFeO_{7-\delta}$ (RPn2) refinement, Figure 5.6, showed significant deviations from full oxygen occupancy, i.e. the presence of oxygen vacancies, at all measured temperatures. These vacancies were formed primarily in the O3 position in the center of the perovskite layer, Figure 5.8b. Refined occupancies for this site ranged from 0.71(1) at 765 K to 0.56(2) at 1070 K. Smaller vacancy concentrations occurred in the neighboring O2 site, while the O1 site that borders the rock-salt layer remained fully occupied at all measured temperatures. The O2 oxygen position was best fit by an anisotropic model for atomic displacement, with preferred displacement towards the O2 site, Table 5.2. The O3 and O1 positions were fit equally well with either an isotropic or anisotropic atomic displacement model and were thus set as isotropic.

The corresponding Fourier nuclear density map, Figure 5.6, shows low nuclear density around the O3 position, as expected based on the low occupancy of this oxygen site. The nuclear density of the O2 site is preferentially distorted towards the O3 site, as expected from the anisotropic atomic displacement parameters. This preferential displacement in combination with the high concentration of oxygen vacancies at the O3 and O2 positions indicates a probable pathway for oxygen vacancy mediated transport between these two positions in the perovskite layer. Conversely, the lack of oxygen vacancies in the O1 position combined with comparatively low atomic displacement indicates that significant oxygen transport does not occur through the O1 sites in the rock-salt layers.

$LaSr_3Co_{1.5}Fe_{1.5}O_{10-\delta}$ (RPn3), Figure 5.7, has a similar distribution of oxygen vacancies as the RPn2 phase, with the O1 oxygen sites in the rock-salt layer remaining fully occupied at all measured temperatures and the majority of the oxygen vacancies located near the center of the perovskite layers, Figure 5.8c. Unlike the RPn2 phase however, the vacancies are located on both the O3 and O4 sites, corresponding to the oxygen sites in contact with the center octahedron rather than exclusively in the centermost oxygen site. The overall oxygen occupancy of the RPn3 phase remains higher than that of the RPn2 phase and lower than that of the RPn1. The O3 and O4 sites were best fit with an anisotropic model for atomic displacement, while attempts to fit the O1 and O2 sites with an anisotropic model did not significantly alter the refined χ^2 value, Table 5.3.

The Fourier nuclear density map, Figure 5.7, and refined atomic displacement parameters, Table 5.3, suggests an oxygen transport pathway through the lower occupancy O3 and O4 sites. The O3 site shows anisotropic atomic density in the a-b plane. A possible split in the O4 site can be discerned from the nuclear density at the O4 site which may explain the very large refined anisotropic atomic displacement parameters for the O4 site. Both confirm a large spread in atomic density perpendicular to the B-site in the center of the octahedron. Attempts to refine this oxygen site as a split site did not significantly alter the refined χ^2 value over a single anisotropic position. The high occupancy and relatively low average displacement suggests low transport rate through the O1 sites in the rock-salt layer.

For comparison purposes, the overall oxygen site occupancy between the three structures is shown in Figure 5.8, and follows the trend RPn2 > RPn3 >> RPn1 at each temperature. This may be expected due to the increasing Sr^{2+} substitution from RPn2 > RPn3 > RPn1. Each individual material also shows the expected trend of decreasing oxygen stoichiometry with increasing temperature due to reduction of the B-site cations. In all three structures, the density of the oxygen sites located in the B-site layers of the octahedrons are heavily anisotropic in favor of motion tangential to the octahedron, with the oxygen sites located in the A-layers showing a lesser but still present anisotropy with similar preferences. This anisotropy supports the idea of a curved oxygen exchange pathway around the B-site centers of each octahedron[7,8].

A comparison of the direct distances between neighboring oxygen sites for all three materials is shown in Figure 5.9. The RPn2 has the shortest distance between the most likely sites for oxygen transport, the O2 and O3 sites. Transport distances between O3 and O4 sites in the RPn3 structure were slightly longer at lower temperatures, yet were almost equal at 1070 K. The RPn1 structure had the longest oxygen transport distance, with the distance between neighboring O2 sites shown to be shorter than transport between O1 and O2 sites.

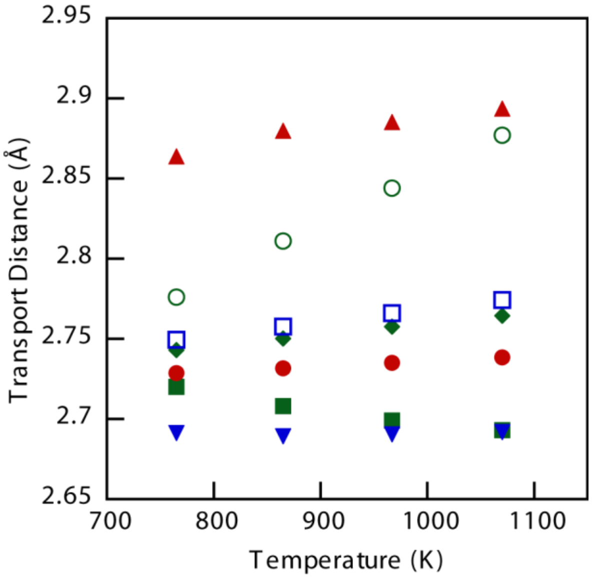

Figure 5.9*: Direct oxygen transport distances between nearest oxygen sites: RPn1 O2 - O2 (Red closed circle), RPn1 O1 - O2 (Red triangle), RPn2 O2 - O2 (Blue open square), RPn2 O2 - O3 (Blue inverted triangle), RPn3 O2 - O3 (Green open circle), RPn3 O3 - O4 (Green closed square), RPn3 O4 - O4 (Green diamond).*

Further comparisons of Co/Fe-O bond lengths as well as comparisons in O-Co/Fe-O bond angles for the three materials are shown in Figure 5.10 and Figure 5.11 respectively. The RPn2 phase has significantly more angular distortion in the octahedron centered on the Co/Fe1 site, yet the RPn3 phase had significantly more distortion in Co/Fe-O bond lengths with the Co/Fe1-O3 and Co/Fe2-O3 bond lengths varying significantly from the ideal octahedron with increasing temperature.

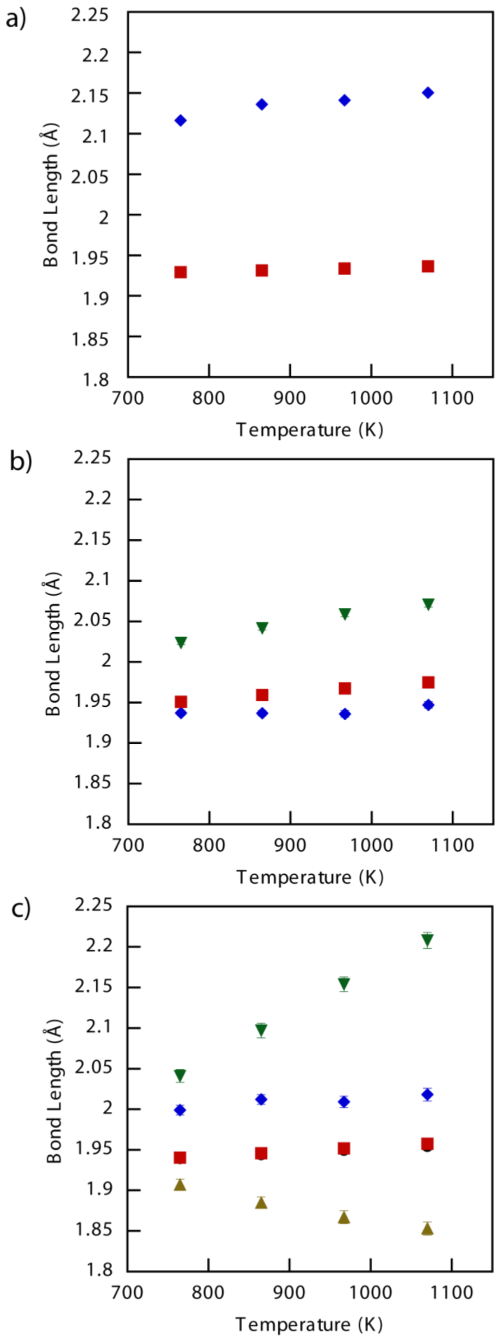

***Figure 5.10**: Co/Fe - O bond lengths for: a) RPn1 structure Co/Fe1 - O1 (Blue Diamond), Co/Fe1 - O2 (Red square) b) RPn2 structure Co/Fe1 - O1 (Blue Diamond), Co/Fe1 - O2 (Red square), Co/Fe1 - O3 (Green inverted triangle) c) RPn3 structure Co/Fe1 - O1 (Blue Diamond), Co/Fe1 - O2 (Red square), Co/Fe1 - O3 (Green inverted triangle), Co/Fe2 - O3 (Gold triangle), Co/Fe2 - O4 (Black circle, located under Co/Fe1 - O2 red squares).*

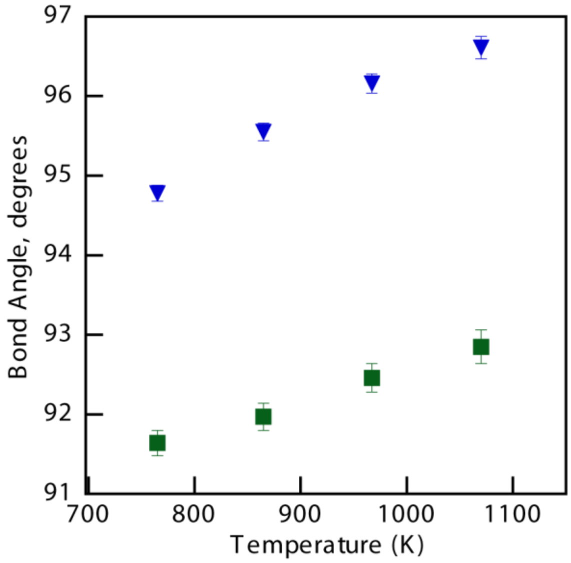

***Figure 5.11**: Bond angle of O1 - Co/Fe1 - O2 bond for RPn2 (Blue inverted triangle) and RPn3 (Green square) structures. Increased angle above 90 ^{0} corresponds to a distortion of the O2 site towards the perovskite layers compared to an ideal octahedron.*

The octahedron bordering the rock-salt layer is distorted for all materials by a shift of the O1 site position towards the rock-salt layer and displacement in the Co/Fe1 and neighboring oxygen sites. This is evidenced by a distortion of the O1 site from the La/Sr1 plane, with the O1 site migrating into the rock-salt layer by 11.9%, 9.9%, and 11.1% of the distance between the La/Sr1 planes forming the rock-salt layer, showing that this distortion increases with greater La/Sr ratio.

The Co/Fe1-O3 bond length similarly increases to 2.071 Å and 2.208 Å for the RPn2 and RPn3 phases compared to expected lengths of 1.874 Å and 1.861 Å respectively, assuming the Co/Fe1 position midway between the neighboring La/Sr sites. The corresponding bond length for the RPn1 phase fixed to 2.147 Å by symmetry. The difference between these lengths demonstrates a displacement of the Co/Fe1 site towards the rock-salt layer, likely caused by the available free space in this layer. The equatorial oxygen site O2 is similarly displaced from its ideal site, with an O2-Co/Fe1-O2 angle of

166.77^0, and 174.30^0 for the RPn2 and RPn3 phases with the O2 site located closer to the perovskite. This angle is held constant by symmetry at 180^0 for the RPn1 phase.

5.4 *Discussion*

The overall oxygen stoichiometry of the three materials follows the trend we may expect with varying La/Sr ratio at a fixed Co/Fe ratio; the oxygen vacancy concentration decreases (oxygen occupancy increases) in the order RPn2 > RPn3 >> RPn1 as Sr/La ratio decreases in the order 9>3>1. Increasing Sr^{2+} substitution for La^{3+} leads to a decrease in overall oxygen site occupancy through oxygen vacancy formation due to charge compensation, holding temperature and pO_2 constant. The temperature dependence of overall oxygen stoichiometry for the RPn1, RPn2, and RPn3 phases, Figure 5.8, shows the expected trend of decreasing occupancy with increasing temperature at constant pO_2 as the average B-site oxidation state decreases.

We can infer the preferred ion transport pathways in these layered materials through consideration of site occupancy, and observed atomic displacement from the ideal site positions. In general, we find that the vacancies in these materials are primarily located in the perovskite structured layers, confirming the trend identified by several other groups for varying Ruddlesden-Popper materials over a wide range of temperatures[101,104,110-113]. There are almost no oxygen vacancies within the rock-salt layer of any of the Ruddlesden-Popper materials studied, with only the RPn1 phase above 967 K showing any deviation from full occupancy of the O1 site. While this layering of vacancies may be expected to limit ionic conductivity, and thus device performance, similar oxygen vacancy localization is found in the layered perovskites[7,8,114-116] that can provide high performance when employed as SOFC electrode materials.

Oxygen anion transport in the RPn1 structure is limited due to low oxygen vacancy concentrations at both oxygen sites, with the first vacancies forming at 967K. While there are small amounts of oxygen vacancies formed within the O1 site in the rock salt layer for the RPn1 structure, the oxygen transport distances between the O1 and O2 sites range from 2.86 Å – 2.89 Å as the temperature increases from 765 K to 1070 K, slightly longer than the transport distances of 2.72 Å – 2.74 Å between neighboring O2 sites. The transport of oxygen within the RPn1 structure likely utilizes a combination of both the O1-O2-O1 and O2-O2-O2 pathways, as the former utilizes the more vacant O1 site while the latter has reduced transport distances, with the transport likely occurring via a curved pathway[117,118].

There is a correlation between oxygen transport distance and the calculated activation energy for oxygen vacancy transport for a similar composition $La_{2-x}Sr_xCoO_{4-d}$ resulting from molecular dynamics and energy minimization performed by Tealdi et al[119]. The transport pathway of O2-O2-O2 was calculated to have the lowest activation energy for oxygen vacancy migration followed by the O2-O1-O2 pathway and the O1-O1-O1 pathway. This correlation between the direct transport distance and the energy required for motion between the oxygen sites is expected to hold true for materials of similar composition, notably the three Ruddlesden-Popper compositions examined in this work, allowing the measured oxygen transport distances to be utilized as an approximation of the activation energy for oxygen vacancy transport.

The oxygen vacancies in the RPn2 phase are predominantly found at the O3 site in the A-site plane between the two perovskite octahedra. The O3-site oxygen occupancy is as low as 0.56(2) at the highest measurement temperature. Some vacancy formation is observed at the neighboring O2 site in the B-site planes, with a minimum oxygen occupancy of 0.929(7) at the highest measurement temperature. The O1 site in the rock-salt layer is fully occupied under all measurements conditions. This preference for vacancy formation in the A-site plane over the B-site plane is reported in the literature for the related layered-perovskite materials, where oxygen vacancies form almost exclusively in the same plane as either the A or A' cation [7,8,114-116].

If we consider next the direct distances between oxygen sites, transport between neighboring O2 and O3 sites is likely favored due to the relatively short direct distance between these sites, 2.69 Å within error under all measurement conditions. The transport distance between neighboring O2 sites is slightly longer at all measured temperatures, ranging from 2.75 Å to 2.77 Å, suggesting that this alternative hopping pathway may be less favorable, especially considering that such an exchange pathway would not involve the highly vacant O3 site.

The anisotropic atomic displacement of these oxygen sites also suggests a transport pathway between the O2 and O3 sites. There is a significant deviation from the O2 site towards the heavily vacant O3 site, suggesting rapid oxygen exchange between the O2 and O3 sites. The nuclear density on the O2 site is significantly higher than that on the O3 site, corresponding to differences in oxygen occupancy as shown by the change in color from blue to red in the figure. Unfortunately, the low density on the O3 site makes it difficult to visualize any deviations in density towards the O2 site due to the low signal to noise ratio near this low occupancy site.

The oxygen vacancies in the RPn3 structure are split between the O3 position in an A-site layer and the O2 and O4 positions in the B-site layers of the perovskite. The sites have similar oxygen vacancy concentrations at all measurement conditions. This vacancy spread suggests ion transport primarily between the O2, O3 and O4 sites within the perovskite layers. No vacancies are formed at the O1 site in the rock-salt layer. This vacancy distribution across the RPn3 structure is due to the combination of preferential formation of vacancies within the perovskite layers and the favorable localization of these vacancies in the A-site planes.

The oxygen transport distances are similar between neighboring O4 sites, varying from 2.74 Å – 2.76 Å with increasing temperature, and between O3 and O4 sites, varying from 2.72 Å – 2.69 Å with increasing temperature. The distance between O3 and O4 counterintuitively decreases with increasing temperature. This is due to the increase in lattice parameter from thermal expansion being offset by a shift in the position of the O3 site along the c-axis towards the center of the unit cell. The direct distance between O2 and O3 sites is slightly longer, ranging from 2.78 Å to 2.88 Å, suggesting that this pathway may be less active.

The most significant feature of the nuclear density map for RPn3, Figure 5.7, is the apparent split in the nuclear density of the O4 site. Despite the insensitivity of the Rietveld quality of fit between a model with split oxygen sites and one without, the presence of such a clear split in the nuclear density map shows that the most likely case is a split in the position of the O4 site, and likely motion between two apparently equivalent positions at the elevated measurement temperature. The O3 and O4 sites shows significant spread in observed density, while the O2 site is more centered on the ideal position. Based on all of these considerations, we suggest that oxygen anions are mobile between the O2, O3, and O4 sites, perhaps with motion between O3 and O4 preferred.

Comparing all of the data, the shortest oxygen transport distances and highest vacancy concentrations are found for the RPn2 materials, followed by RPn3, with RPn1 showing both the longest transport distances and the least vacant oxygen sites. We thus estimate that oxygen transport rates decrease in the order of RPn2 $\gtrsim$ RPn3 >> RPn1. This is likely a function of both structural and composition variation between the materials, resulting in the observed maximum vacancy concentration for the RPn2 phase synthesized in this study. This follows our previously measured trend of surface reaction rate for these materials; RPn2 $\gtrsim$ RPn3 >> RPn1[103]. The surface exchange rate of RPn2 is ~2.0 times greater than RPn3, which is ~9.6 times greater than RPn1.

Ionic conductivity data published by Manthiram, Prado, and Armstrong[9] decreases in the order of RPn3 $\gtrsim$ RPn2 >> RPn1 at 1173K. The trend in ionic conductivity for RPn2 and RPn3 is reversed compared to the trend of surface exchange rates while RPn1 remains relatively inactive. The ionic conductivity of RPn3 is ~1.9 times greater than RPn2, which is ~17.4 times greater than RPn1, in reasonable agreement with our suggested trend of RPn2 $\gtrsim$ RPn3 >> RPn1. Note that the RPn3 and RPn2 compositions are identical to those examined in this study but the measured RPn1 compositions are the end members $Sr_{1.2}La_{0.8}CoO_{4-\delta}$ and $Sr_{1.2}La_{0.8}FeO_{4-\delta}$, suggesting that the crystal structure is the primary factor in determining differences in conductivity between similar compositions. The discrepancy between studies could be due to the difference in measurement temperature, as the surface rates were measured from 623K to 848K, while the bulk ionic conductivity was measured at 1173K. Furthermore, differences in the state of the surface such as preferential segregation of Sr to the surface, surface impurities, and the formation of secondary phases near the surface can greatly impact surface measurements, with these factors changing greatly depending on specific synthesis conditions and sample history[103,120,121]. The difference in oxygen occupancy and transport distances shown through neutron diffraction between the RPn2 and RPn3 phases become smaller as temperature increases, with almost equal values at 1070K, and may reverse at higher temperatures.

There remains a question as to why the three measured Ruddlesden-Popper phases are distorted from the "ideal" structure where the atoms are positioned to form identical cubic perovskite units between ideal rock-salt structures. All three structures show a significant deviation from fully symmetric octahedra, Figure 5.10 and Figure 5.11, with significant distortion at the rock-salt / perovskite interface. This displacement, as characterized by the difference in Co/Fe1-O bond lengths, increases with the fraction of La^{3+} on the A-site. SrO forms in the rock salt structure, $Fm\bar{3}m$, with alternating A-site cations and oxygen anions forming the structure, while La_2O_3 forms as trigonal $P\bar{3}m1$. Therefore, higher Sr^{2+} fraction leads to lower distortion within the rock-salt layer. It should be noted that the O1 site shows a much greater spread in nuclear density than would be expected compared to the more vacant and mobile oxygen sites, with a correspondingly greater atomic displacement parameter. The spread in density represents both thermal motion as well as static displacive disorder caused by neighboring cations[122]. This uncertainty in the rock-salt O1 position is in line with similar results for n=1 Ruddlesden-Popper structures[107]. As the O1 position is greatly affected by whether the nearest neighbors are La^{3+} or Sr^{2+} cations, since the oxygen sites displace towards La^{3+} cations.

Increasing density of oxygen vacancies in the center of the perovskite layers of the RPn2 and RPn3 structures leads to a shift in position of the neighboring oxygen sites towards the vacancy rich sites. This can be seen in the change in the O1 - Co/Fe1 - O2 bond angle shown in Figure 5.11. Increased distortion in the O2 sites towards the center of the perovskite layer can be viewed as an increase in this bond angle. At all temperatures, the RPn2 has a significantly higher O1 - Co/Fe1 - O2 bond angle than the RPn3, although both structures maintain a bond angle above 90^0. Similarly, the same trend can be seen by comparing the apical angles of the centermost perovskite octahedra for the RPn2 and RPn3 phases, with angles of 93.57 and 93.06 respectively at 1070 K, where increasing angles correspond to a shift in the equatorial oxygen position towards the center of the unit cell where oxygen vacancy concentrations are highest.

5.5 *Conclusion*

$LaSrCo_{0.5}Fe_{0.5}O_{4-\delta}$ (n=1), $La_{0.3}Sr_{2.7}CoFeO_{7-\delta}$ (n=2), and $LaSr_3Co_{1.5}Fe_{1.5}O_{10-\delta}$ (n=3) Ruddlesden-Popper structures were characterized using neutron powder diffraction under *in-situ* conditions from 765 K-1070 K with a pO_2 of 10^{-1} atm. These structures were characterized by a tetragonal P4/*mmm* space group. The average oxygen occupancy per site varied with increased Sr^{2+} concentration, with values of 0.897, 0.912, and 0.955 corresponding to the RPn2, RPn3, and RPn1 phases respectively. These oxygen vacancies were heavily localized within the perovskite layers of the Ruddlesden-Popper structure, with the rock-salt layers remaining almost completely occupied at all measured temperatures. Analysis of the vacancy localization combined with the atomic displacement parameters suggests oxygen transport pathways through the center of the perovskite layers. Under the assumption of similar mobility per vacancy, these results suggest a trend in oxygen transport of RPn2 $\gtrsim$ RPn3 >> RPn1.

6 Is the surface oxygen exchange rate linked to bulk ion diffusivity in mixed conducting Ruddlesden-Popper phases?

6.1 *Introduction*

An intriguing observation in the literature is a proposed correlation between the surface oxygen exchange rate, k,[48] and the bulk anion diffusivity, D, across a wide range of MIEC materials.[76,77,123] Direct correlations between these parameters have been derived,[76] with De Souza suggesting a 'universal' equation for the surface exchange coefficient.[77] The most common interpretation[48,123] for 'electron-rich' materials is that the two processes are linked through the oxygen vacancy concentration. Where bulk anion transport via vacancy hopping depends directly on vacancy concentration, the relationship between the surface exchange coefficient and the vacancy concentration depends on the assumed surface reaction mechanism and the rate limiting step. For example, Merkle et al.[124] derived a direct correlation between these bulk and surface parameters by assuming a two-step surface mechanism; a molecular oxygen rapidly dissociates to form O^{-}, followed by a rate-determining step of oxygen incorporation to fill a vacancy.

An underlying assumption in all of these derived correlations is that the bulk composition and oxygen vacancy concentration extend up to the outer MIEC surface. This assumption is in stark contrast to the observation by multiple authors that the surface compositions of these materials vary dramatically from the bulk. This is most commonly observed as surface enrichment of A-site cations, notably Sr.[1,79,121,125,126] With such segregation it is difficult to reconcile mechanisms that link the outermost surface reaction rate to the bulk composition, structure or oxygen vacancy concentration. If the outermost surface compositions of these materials are similar, we would expect similar surface reaction rates irrespective of the bulk composition or structure. Reconciling these contradictions remains an important challenge to the field.

We have previously suggested that the observed correlation may in part be due to the inherent difficulty in accurately extracting two independent parameters from a single exponential curve;[1] a technique applied in most simultaneous measurements of k and D. This suggestion motivated our group to adopt two independent measurements of these parameters. We utilize in situ neutron diffraction[7,33,35,42,43] to examine bulk ion transport and an isotopic pulse exchange technique to characterize surface exchange rates.[24,34,44,46] This information is then complemented by determination of the surface composition via X-ray photoelectron spectroscopy (XPS) or high sensitivity low energy ion scattering (HS-LEIS).

High temperature, controlled atmosphere in situ powder neutron diffraction is utilized to extract details of crystal symmetry, lattice constants and atomic positions, occupancies, and displacement parameters for both the cations and anions in MIEC materials.[35] While this does not yield a direct measurement of ionic conductivity or a D parameter, this crystallographic information allows the ionic transport pathways in the materials to be discerned and enables direct comparison of ion motion between materials of the same crystal structure. Oxygen anions are transported through the bulk structure via a vacancy hopping mechanism, and thus insights into the rate of oxygen transport for a given material can be gained by simultaneous consideration of the concentration of oxygen vacancies, the hopping distance between neighboring oxygen sites, and the magnitude and orientation of the anisotropic atomic displacement parameters for the anions.

We have previously performed these combined studies on both cubic[34] and layered perovskites,[24] and in both cases we have found the same correlation between high bulk ion mobility and rapid surface exchange, even noting changes in surface exchange rate upon changes in bulk crystal symmetry. This is despite the surface compositions of these materials varying dramatically from the average bulk compositions. Herein we present a related body of work, studying layered Ruddlesden–Popper structures and suggesting a possible explanation for the observed correlation. The Ruddlesden–Popper phases are layered materials of general form $A_{n-1}A'_2B_nO_{3n+1}$, $A_{n-1}A'_2B_nX_{3n+1}$, consisting of n perovskite layers alternating with a rock salt layer. Figure 6.1 illustrates the structures of the n = 1, n = 2 and n = 3 materials considered in this study.

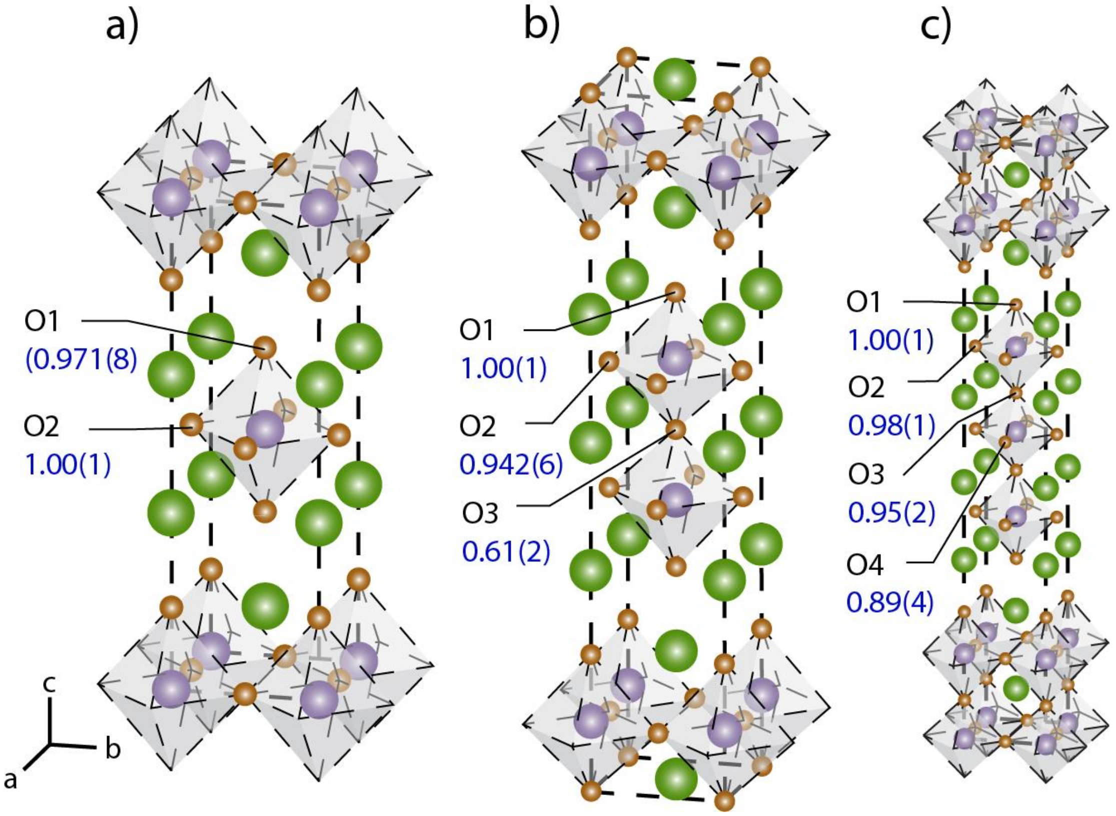

***Figure 6.1**: Ruddlesden–Popper structures for (a) n = 1 (RPn1), (b) n = 2 (RPn2) and (c) n = 3 (RPn3). Note that these structures are derived from Rietveld refinement of the neutron diffraction data collected at 967 K with a pO_2 of 0.1 atm. The numbers in blue denote the refined oxygen site occupancies at these conditions.*

6.2 ***Experimental***

Material synthesis

Formation of n = 1, n = 2 and n = 3 Ruddlesden–Popper phases with identical La/Sr and Co/Fe ratios was not possible due to sample decomposition into a mixture of the desired phase along with perovskite, simple oxide and other Ruddlesden–Popper phases. Sharma and Singh developed a tolerance factor for Ruddlesden–Popper n = 1 phases.[105] This approach was used to vary the La/Sr ratio at a constant Co/Fe ratio to synthesize three Ruddlesden–Popper materials, $LaSrCo_{0.5}Fe_{0.5}O_{4-\delta}$ (RPn1), $La_{0.3}Sr_{2.7}CoFeO_{7-\delta}$ (RPn2), and $LaSr_3Co_{1.5}Fe_{1.5}O_{10-\delta}$ (RPn3). Each material has a tolerance factor t_f of approximately

1.08, corresponding to a tetragonal phase K_2NiF_4-type structure. The La/Sr ratios vary from 1 : 1 to 1 : 9 and 1 : 3 for RPn1, RPn2, and RPn3 materials, respectively.

All materials were synthesized using the modified Pechini method, as described in section 1.4. The cake resulting from this combustion was then ground into powder and calcined in air at 1623 K for 10 hours. The final powder samples were characterized by X-ray diffraction [Rigaku Miniflex II, Texas, USA] as an initial verification of phase purity.

In situ determination of bulk crystal structure

Neutron diffraction measurements were conducted at the POWGEN beamline, Spallation Neutron Source (SNS), Oak Ridge Laboratory, Oak Ridge, TN, USA. The sample environment was created using a continuous flow of an ultra-high purity mixture of O_2 and N_2 with a pO_2 of 10^{-1} atm at 500 sccm, with each sample allowed to equilibrate for at least one hour prior to each measurement. Diffraction patterns were collected at 967 K in the d-spacing range of 0.45–5.35 Å until a total accelerator source proton charge of 9.0×10^{12} pC was reached (~2 hour measuring time). Rietveld[37] refinements were performed using the GSAS package[38] with the EXPGUI interface as described in Section 1.7.

Surface oxygen exchange

Surface oxygen exchange rates were measured utilizing the isotopic pulse exchange technique described in Section 1.8. 100 mg of powder, sieved to particle diameters between 106 μm and 150 μm, was placed within a 4 mm id. quartz tube and held in place by plugs of quartz wool. Measurements of reaction rates at higher temperatures were performed using samples diluted with $SrTiO_3$ (STO) to avoid exchange of the entire isotopic pulse. STO is inert relative to the materials of interest for the oxygen exchange reaction.[24]

Pulses were measured in sets of five at each temperature, with the standard deviation between measurements represented as error bars in the data. Each pulse within a set was separated from the others by a 90 s delay to allow sufficient time for the measured isotopic fraction to return to baseline values.

Surface composition

The surface compositions were measured by high sensitivity-low energy ion scattering (HS-LEIS, ION-TOF Qtac-100, Münster, Germany). Powder samples were treated in air at 1173 K for 12 hours and pressed into pellets at 2000 psi. An initial scan was performed using 3 keV He^+ to identify the presence of lighter surface contaminants such as surface carbonates.[34] The samples were then exposed to an oxygen plasma to remove any surface carbon species without altering the distribution or composition of the outer surface. Measurements of the surface composition were then performed using 5 keV Ne^+ to further distinguish between the La and Sr peaks, as the two peaks partially overlap when utilizing a He^+ ion source. The ion beam impacted normal to the surface and was rastered over a 1000 μm × 1000 μm area. Repeated sputtering of the sample surface with 2.1×10^{14} cm^{-2} of a 0.5 keV Ar^+ beam followed by subsequent measurement with the 5 keV Ne^+ ion source allowed for the development of a depth profile to examine the transition from surface to bulk compositions within the samples. To enhance the signal to background ratio for a given measurement time, measurements were focused on three regions: (1) 1100–1400 eV with 7.2×10^{13} Ne^+ cm^{-2} for Fe and Co, (2) 1900–2300 eV with 1.3×10^{13} Ne^+ cm^{-2} for Sr; and (3) 2650–3000 eV with 1.3×10^{13} Ne^+ cm^{-2} for La.

6.3 *Results*

In situ neutron diffraction

At 967 K and $pO_2 = 0.1$ atm, the structures of all three samples were fit satisfactorily to a tetragonal structure, space group I4/mmm, as depicted in Figure 6.1. Figure 6.2 shows the measured, fit, and difference patterns, with structural details and quality of fit parameters listed in Table 6.1 - Table 6.3. Less than 4 wt% of a cubic perovskite impurity phase, space group $Pm\bar{3}m$, was present in each sample, with positions denoted by an asterisk in Figure 6.2. No evidence for A-site (La/Sr) or B-site (Co/Fe) ordering nor deviations from the proposed material stoichiometries were observed from the refinement. As such the occupancies of A-sites and B-sites by La/Sr and Co/Fe were fixed at the proposed overall material compositions and the atomic displacement parameters for the individual A- and B-sites were identical irrespective of cation.

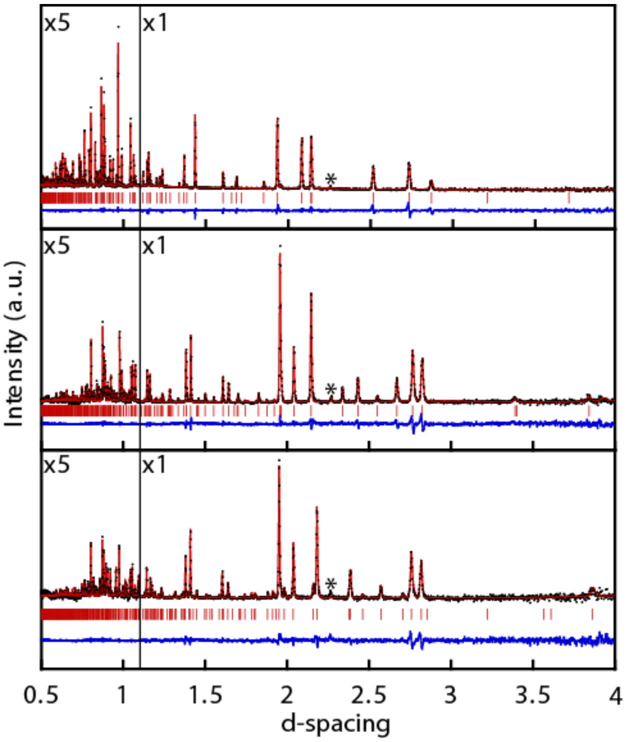

Figure 6.2: *Neutron diffraction patterns collected at 967 K with a* pO_2 *of 0.1 atm for (a)* $LaSrCo_{0.5}Fe_{0.5}O_{4-\delta}$ *(RPn1), (b)* $La_{0.3}Sr_{2.7}CoFeO_{7-\delta}$ *(RPn2), and (c)* $LaSr_3Co_{1.5}Fe_{1.5}O_{10-\delta}$ *(RPn3) samples. All three materials were fitted to structures with the I4/mmm space group. A perovskite (*$Pm\bar{3}m$*) impurity was identified in each sample, with the primary diffraction peak marked by an asterisk. Measured data (black dots), calculated diffraction pattern (top red line), difference pattern (bottom blue line) and expected peak positions are shown.*

Table 6.1*: Tetragonal space group I4/mmm, Rietveld fit parameters for RPn1 structure at 967 K with sites: La/Sr1: 4e (0,0,Z), Co/Fe1: 2a (0,0,0), O1: 4e (0,0,Z), O2: 4c (0.5,0,0);*

RPn1 I4/mmm 967 K

a,b (Å)	3.868(1)	χ^2	4.522
c (Å)	12.840(1)	R_P %	0.1055
V (Å^3)	192.08(1)	wR_P %	0.0423
ρ_c (g/cm^3)	5.999		

	Atomic displacement parameters (Å^2)*100				Fractional
	U_{11}/U_{iso}	U_{22}	U_{33}	Z	Occupancy
La/Sr1	1.90(2)			0.359(1)	
Co/Fe1	1.53(3)				
O1	3.52(7)	3.52(7)	1.8(1)	0.167(1)	0.971(8)
O2	1.0(7)	2.7(1)	3.3(1)		1.0

Table 6.2*: Tetragonal space group I4/mmm, Rietveld fit parameters for RPn2 structure at 967 K with sites: La/Sr1: 4e (0,0,Z), La/Sr2: 2b (0,0,0.5), Co/Fe1: 4e (0,0,Z), O1: 4e (0,0,Z), O2: 8g (0,0.5,Z), O3: 2a (0,0,0);*

RPn2 I4/mmm 967 K

a,b (Å)	3.912(1)	χ^2	4.529
c (Å)	20.409(1)	R_P %	0.1459
V (Å^3)	312.28(1)	wR_P %	0.0587
ρ_c (g/cm^3)	5.265		

	Atomic displacement parameters (Å^2)*100				Fractional
	U_{11}/U_{iso}	U_{22}	U_{33}	Z	Occupancy
La/Sr1	2.87(6)			0.317(1)	
La/Sr2	2.52(7)				
Co/Fe1	1.76(5)			0.101(1)	
O1	3.65(7)			0.196(1)	1.0
O2	3.4(1)	1.8(1)	4.4(2)	0.091(1)	0.942(6)
O3	4.7(3)				0.61(2)

***Table 6.3**: Tetragonal space group I4/mmm, Rietveld fit parameters for RPn3 structure at 967 K with sites: La/Sr1: 4e(0,0,Z), La/Sr2: 4e (0,0,Z), Co/Fe1: 4e (0,0,Z), Co/Fe2: 2a (0,0,0), O1: 4e (0,0,Z), O2: 8g (0,0.5,Z), O3: 4e (0,0,Z), O4: 4c (0,0.5,0)*

RPn3 I4/mmm 967 K

a,b (Å)	3.900(1)	χ^2	2.786
c (Å)	28.523(1)	R_P %	0.1577
V (Å^3)	433.78(2)	wR_P %	0.0587
ρ_c (g/cm^3)	5.568		

	Atomic displacement parameters (Å^2)*100				Fractional
	U_{11}/U_{iso}	U_{22}	U_{33}	Z	Occupancy
La/Sr1	2.5(1)			0.2013(1)	
La/Sr2	2.8(1)			0.0710(2)	
Co/Fe1	1.5(1)			0.1409(1)	
Co/Fe2	2.7(1)				
O1	3.8(2)			0.2114(2)	1
O2	2.5(1)			0.1380(2)	0.98(1)
O3	5.7(3)			0.0654(3)	0.95(2)
O4	12(1)	2.2(4)	11.4(9)		0.89(4)

Of primary interest to oxygen anion transport is the relative occupancies, Figure 6.1 and, anisotropic atomic displacement parameters, Table 6.1 - Table 6.3, and direct site-to-site hopping distance, Table 6.4, of the oxygen sites in the structure. These represent the oxygen vacancy concentrations, the average motion of the oxygen anions, and the hopping distance for oxygen transport, respectively.

Table 6.4*: Direct oxygen transport distances through least occupied sites at 967 K. Transport distances between neighboring equatorial oxygen sites as well as between axial and equatorial sites are considered*

Direct oxygen transport distances at 967 K			
	RPn1	**RPn2**	**RPn3**
O_1–O_2	2.885(2)	2.905(4)	2.860(6)
O_2–O_2	2.734(1)	2.766(1)	2.758(1)
O_2–O_3		2.690(2)	2.844(7)
O_3–O_4			2.699(5)
O_4–O_4			2.758(1)

The oxygen sites in the RPn1 material were almost completely occupied under the measurement conditions, with only a small vacancy concentration, 97.1(8)% occupied, for the apical oxygen of the perovskite layer. The RPn2 and RPn3 both show increased vacancy concentrations and a degree of vacancy localization within the perovskite layers, with the oxygen sites in the rock-salt layer refined to full occupancy. This localization trend is analogous to previously published data on both Ruddlesden–Popper[9,104,111-113] and other layered materials.[7,8,20] The RPn2 structure was found to have the lowest oxygen stoichiometry, with an occupancy of 0.61(2) at the centermost apical oxygen site (O3) and an occupancy of 0.942(6) at the neighboring equatorial (O2) site. The oxygen vacancies in the RPn3 structure were more diffuse, although still centered within the central octahedron, with the central equatorial site (O3) showing the lowest occupancy and with occupancy increasing outward from the center through O3, O2 and O1.

The compositions thus calculated are $LaSrCo_{0.5}Fe_{0.5}O_{3.94}$ (RPn1), $La_{0.3}Sr_{2.7}CoFeO_{6.38}$ (RPn2) and $LaSr_3Co_{1.5}Fe_{1.5}O_{9.58}$ (RPn3); that is, the oxygen vacancy concentration follows the trend RPn2 > RPn3 > RPn1. This trend is expected via charge compensation from the increasing Sr^{2+}vs. La^{3+} content at a fixed Co/Fe ratio in the same trend of RPn2 > RPn3 > RPn1.

Ideally, anisotropic atomic displacement parameters would be utilized for each oxygen site in each structure. However, the addition of these fit parameters is only justified if it leads to significant improvement in refinement quality (measured by χ^2, R_P and wR_P parameters). This was the case for only a limited number of sites in this study; for all other cases, the atomic displacement parameters were refined isotropically. The isotropic atomic displacements for the least occupied equatorial sites of each material are shown as density maps in Figure 6.3, illustrating their relative anisotropy.

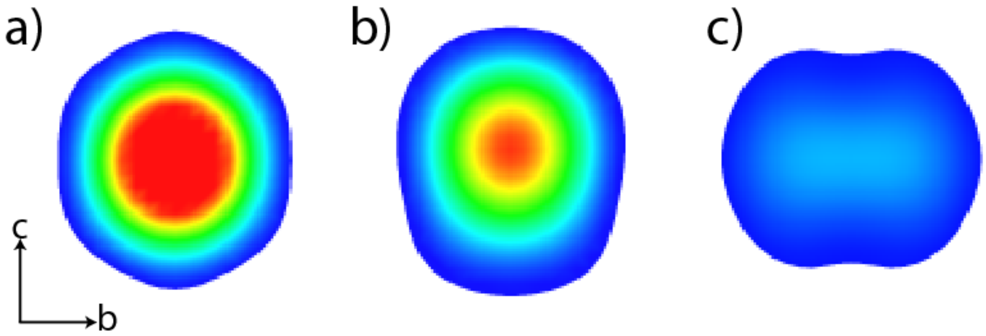

Figure 6.3*: Observed nuclear density cut along the b–c plane of the least occupied equatorial oxygen for (a) the O2 site of RPn1, (b) the O2 site of RPn2 and (c) the O4 site of RPn3.*

The refined anisotropic oxygen displacement parameters for the two oxygen sites in the RPn1 structure indicate that the apical (O1) site moves primarily within the a–b plane towards the nearest neighbor equatorial oxygen site (O2). In turn, this neighboring site shows preferential displacement along the c-axis towards the apical site.

Unfortunately, any anisotropy of the apical sites (O1 and O3) in the RPn2 phase could not be differentiated from the Rietveld refinement. However, we can observe a significant increase in atomic displacement for the lowest occupancy central apical site (O3) when compared to the site in the rock salt layer (O1). We were able to differentiate anisotropic displacement for the equatorial site (O2) which showed statistically significant preferential displacement along the c-axis towards the apical sites and along the face of the unit cell towards the equatorial neighbor, when compared with motion towards the central B-cation.

Similar limitations were observed in determining the anisotropy of the oxygen sites in the RPn3 material. Only the O4 equatorial site showed significant anisotropic displacement, again along the c-axis towards the apical site and along the face of the unit cell towards the neighboring equatorial site.

The neutron diffraction data also provides information on the relative direct oxygen transport distances between materials, Table 6.4. Note that we only consider hops between nearest neighbors and that these direct distance comparisons do not account for the real curved path that the oxygen anions must take around the cations. The shortest hop across all materials is between the least occupied apical O3 site and the neighboring equatorial O2 site in the RPn2 structure. The second shortest is between the similar lowest occupied equatorial O4 site to the apical O3 site in the RPn3 structure. The differences in direct hopping distances are due to atomic shifts from the ideal lattice sites towards the lower oxygen occupancy planes in the structure, Table 6.1 - Table 6.3.

In situ neutron diffraction data was also collected at 765 K, 865 K and 1070 K and will be presented in detail elsewhere. The crystal structure and, in general terms, all of the trends between materials observed at 967 K are conserved across the temperature range.

When taken in combination, the locations and densities of oxygen vacancies, the atomic displacement magnitudes and directionalities, and the distances for vacancy hopping all suggest an oxygen anion transport pathway through the central perovskite layers of all of these materials. Rapid ion transport should be favored by high local vacancy concentration (low oxygen occupancy) and short hopping distances. Based on these considerations, we conclude that ion transport through the perovskite layers decreases in the order RPn2 > RPn3 > RPn1.

In particular, the O2 to O3 hop in RPn2 is favored by having the shortest distance and highest vacancy concentration. The relatively diffuse and highly oriented atomic displacement between these two sites is further confirmation that transport between these sites is facile. We suggest that this is the most facile pathway observed in all three of these materials. Hops between other sites in RPn2 are less favorable due to greater distances and lower vacancy concentrations, also reflected in the more localized atomic displacement parameters. The RPn1 structure is the least favorable due to high oxygen occupancy in the perovskite layer and relatively long hopping distances between nearest neighboring sites. The RPn3 structure is a middle case, with vacancies distributed across the sites in the perovskite layers and some short hops comparable to those in the RPn2 structure.

Surface exchange and composition

Representative data for the isotopic pulse experiments are shown in Figure 6.4a. At room temperature, there is no detectable exchange of $^{18}O_2$, resulting in a single peak corresponding to the $^{18}O_2$ signal (m/z = 36). At operating temperatures, there is significant exchange of ^{18}O from the gas phase with ^{16}O species in the material, yielding a large $^{16}O^{18}O$ (m/z = 34) signal with corresponding decrease in the $^{18}O_2$ signal.

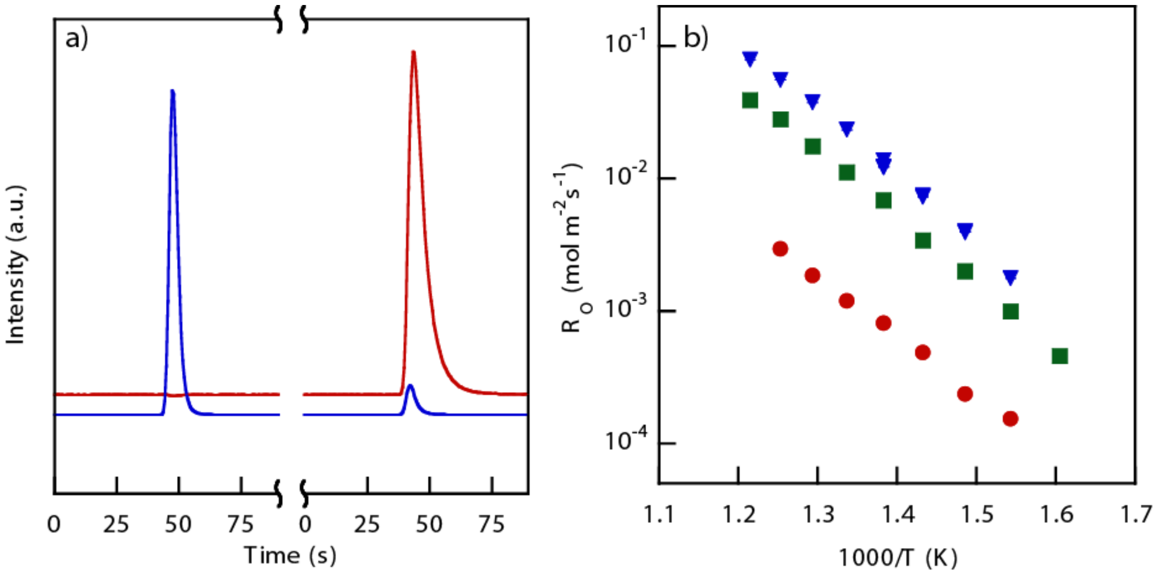

***Figure 6.4**: (a) Representative RGA signals for $^{16}O^{18}O$ (m/z = 34, red) and $^{18}O_2$ (m/z = 36, blue) for pulses at 298 K (left) and 973 K (right). (b) Arrhenius plot of surface reaction rates derived from $^{18}O_2$ isotopic pulse experiments for RPn1 (red circle), RPn2 (blue inverted triangle) and RPn3 (green square).*

The overall surface oxygen exchange rate, R_0, is shown as a function of inverse temperature for all three materials in Figure 6.4b. The reaction rate of the RPn2 phase was found to be the highest, followed reasonably closely by RPn3, with the rate over RPn1 being more than one order of magnitude lower. The experiment was repeated with multiple pure samples and samples diluted with STO in order to measure reaction rates at the highest temperatures. No deviation was observed upon repetition or dilution. The activation energies calculated for each of the Ruddlesden–Popper samples were 85.5 kJ mol^{-1}, 95.7 kJ mol^{-1} and 95.4 kJ mol^{-1} for the RPn1, RPn2 and RPn3 phases, respectively.

Initial scans of the as-prepared surfaces of each material using the 3 keV He$^+$ beam (selected to observe light elements on the surface) showed well defined O, C (likely as carbonate) and Sr peaks with a small shoulder to the Sr peak hinting at the presence of

La when using He^+ as the probe ion. The carbon contaminants were removed by treatment of the surface with oxygen plasma.

Switching to 5 keV Ne^+ probe ions to differentiate between Sr and La showed each surface to be dominated by Sr, with small amounts of surface La present (Figure 6.5 and Figure 6.6). Co and Fe were absent from the surface. Repeated sputtering with 0.5 keV Ar^+ enabled determination of a depth profile. Oxygen is not measured due to the use of the Ar^+ ion. Peaks attributed to Co and Fe were identified after the initial surface was removed. The measurement of a depth profile continued until the Sr, La and Co/Fe peak areas were constant, considered to be equal to the bulk ratios. These bulk values were used to normalize the surface spectra and calculate the composition profiles as functions of depth, Figure 6.6.

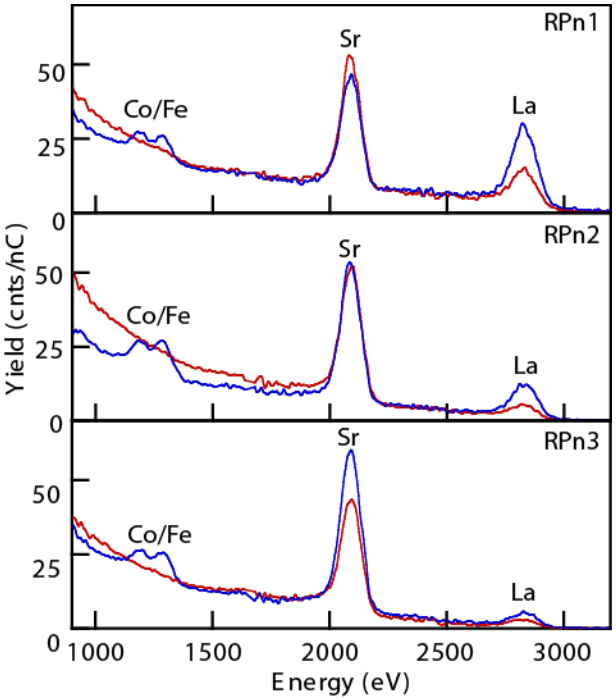

Figure 6.5: *Example LEIS spectra for RPn1, RPn2 and RPn3 samples, showing initial scans of the surfaces after treatment with O atoms (red) and after achieving bulk compositions (blue).*

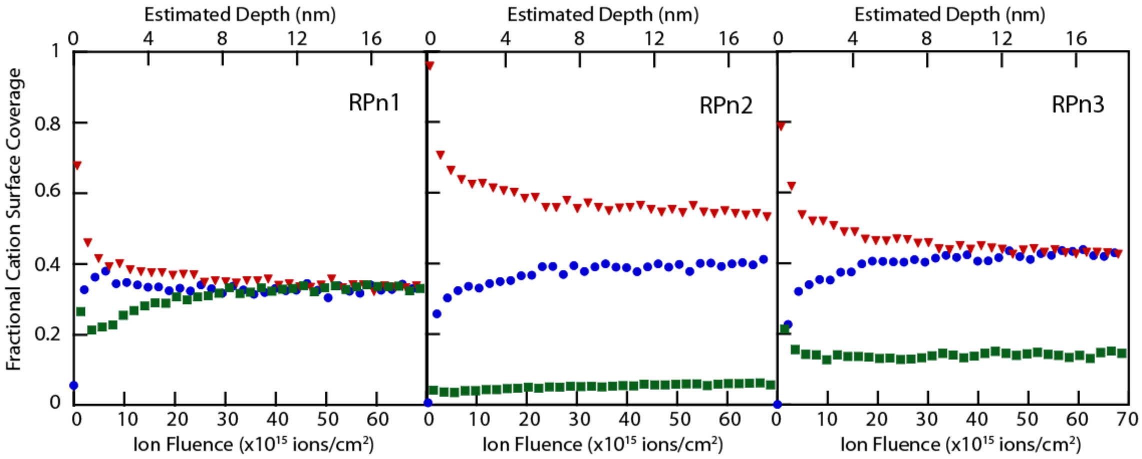

Figure 6.6: *Depth profiles generated by LEIS, showing the fractional surface coverages of Co/Fe (blue circle), Sr (red inverted triangle) and La (green square) for RPn1, RPn2 and RPn3 structures.*

All three materials show a significant surface enrichment of Sr with a corresponding absence of B-site cations Co and Fe. Figure 6.6 shows that the surfaces of the materials have 68%, 96% and 70% surface coverage of Sr cations for the RPn1, RPn2 and RPn3 materials, respectively, with the remainder comprised of La cations. This follows the trend of the Sr/La ratios in the materials and is in line with previous reports. [1,49,79,121,125-128] The similarities of the surfaces of these three Ruddlesden–Popper materials, despite the vastly differing bulk structures, would hint that the three should have comparable surface reaction rates. The approximate sputtering depth was estimated from previously published work.[121] The compositions reach the bulk values within ~10 nm of the surfaces.

6.4 *Discussion*

Numerous research groups have identified correlations between surface and bulk oxygen transport rates. For example, the trends proposed by De Souza show a direct correlation between surface exchange and bulk diffusivity for a wide range of materials.[77] The existence of this trend over such a wide range of materials despite that fact that surface structures can vary greatly depending on synthesis route, and more importantly differ significantly from the bulk structure due to cation segregation[49,127] or the presence of surface impurities,[50] shows a fundamental issue with the separation between “surface” and “bulk” properties.

Our work on these Ruddlesden–Popper phases appears to confirm the previously reported correlation between rapid oxygen surface exchange and high ion mobility. The ionic mobility follows the same trend as the surface exchange rates: RPn2 > RPn3 > RPn1. In this case, the relatively high activity of the RPn2 phase is likely due to the relatively high oxygen non-stoichiometry of the RPn2 phase, induced by the higher Sr/La ratio in this material. The more puzzling aspect is the question of why we see the k–D correlation across these materials, especially when we observe that the outer surface composition looks very similar between materials. If the surface exchange rate is a true measure of oxygen dissociation kinetics on the outer atomic surface, we would anticipate very similar rates for all of the materials in this study, and indeed for all materials with heavily Sr-enriched surfaces.

If the outer atomic surface composition directly reflected the bulk composition, it may be possible to explain the k–D correlation in terms of oxygen vacancy availability or energetics of vacancy formation. However, when the outer surface composition of three materials looks similar but the measured exchange rate differs by more than an order of magnitude, the simplest logical explanation is that the measured 'surface' exchange rate is not a true 'atomic outer surface' rate.

This can be confirmed simply for our isotopic exchange measurements. In the course of these measurements ~0.4% of the bulk ^{16}O within each particle is exchanged for ^{18}O. Assuming that the ^{18}O missing from the pulse must require an equal amount of ^{16}O to be released from the sample, at minimum the surface ~200 nm of the ~150 μm particles participate in the isotope pulse reaction with this depth calculated based on a complete exchange within the depth. The actual value is likely to be higher due to bulk mixing. In contrast, the surface Sr enrichment reaches the bulk composition within ~10 nm of the outer surface. Thus, the isotopic pulse experiments exchange oxygen across a depth ~20 times greater than the thickness of the outer "surface" composition of the material, resulting in a significant contribution of "bulk" transport rates within the measurement of the surface exchange rate. We suggest that a similar 'surface sensitivity' analysis should be conducted for all of the approaches to measuring surface exchange rates and bulk diffusivity. Certainly the observed consistent k–D correlation across materials and, to the best of our knowledge, universal variation of surface composition from the bulk suggests that measured values for k are influenced by penetration into the outer layers of the material.

Despite this, materials exhibiting rapid surface exchange also typically yield high performance electrodes. Any oxygen incorporated into these materials must be transferred from the outer atomic surface into the bulk, and we propose that the surface exchange rates in the literature simply reflect the incorporation rate into the first few hundred nanometers of the material. Thus, the measured parameters are still very useful, and we would suggest, still applicable for some modelling efforts.

The concept that we are inherently measuring a bulk property when we attempt to measure surface exchange rates has implications for our understanding of surface incorporation rates. It certainly suggests that oxygen dissociation and incorporation in the outermost atomic layers is facile when compared with ionic transport across a few hundred nanometers. If these outermost steps, which must be determined by the outermost atomic composition, were rate limiting, we would measure the same surface exchange rates across materials in this study. Instead, we find a correlation between the surface exchange rate and the bulk ion mobility. It appears that the bulk transport is rate limiting.

An alternative explanation is that all samples are surface limited and that the Sr content on the outer surface determines the rate. The determined surface exchange rates do increase as the Sr surface concentration increases, however it is difficult to correlate a greater than one order of magnitude difference in the surface exchange rate between RPn1 and RPn3 with the relatively small difference (2%) in surface composition. It seems more likely that the large difference in vacancy concentration and ion mobility is responsible.

The challenge to the field then remains to measure the rates of these outermost surface steps. In our case, it is difficult to increase the surface sensitivity of the isotopic pulse technique as we are limited by limits of isotope detection in the RGA. We can become more surface sensitive by utilizing smaller pulses or more rapid gas flow rates but the measurements simultaneously become much more difficult to make due to the reduced area of the resulting peaks generated by the RGA. It is not clear how surface sensitive the other commonly used techniques are.

6.5 *Conclusion*

Three Ruddlesden–Popper phases of general form $A_{n-1}A'_2B_nX_{3n+1}$, $LaSrCo_{0.5}Fe_{0.5}O_{4-\delta}$ (n = 1, RPn1), $La_{0.3}Sr_{2.7}CoFeO_{7-\delta}$ (n = 2, RPn2) and $LaSr_3Co_{1.5}Fe_{1.5}O_{10-\delta}$ (n = 3, RPn3), were synthesized and found to have a tetragonal structure, space group I4/mmm, at 967 K and pO_2 = 0.1 atm. The oxygen vacancies in these materials were localized within the perovskite layers, with vacancy concentration following the expected trend, concurrent with Sr/La ratios of RPn2 > RPn3 > RPn1. Analysis of the crystal structure indicates that vacancy mobility follows the same trend. A similar trend in oxygen surface exchange rate is observed despite the surface compositions of the materials being quite similar. All surfaces showed significant surface segregation of Sr. It is suggested that the observed correlation between surface and bulk properties is due to experimental limitations that inherently convolute the two properties. Furthermore, our results indicate that surface oxygen incorporation is not rate limiting in these materials. The challenge remains to experimentally determine the true outer surface oxygen exchange rate.

7 Structural Analysis of $PrBaMn_2O_{5+\delta}$ under SOFC Anode Conditions by In-Situ Neutron Powder Diffraction

7.1 *Introduction*

While direct hydrocarbon solid oxide fuel cells (SOFCs) offer efficient power generation from hydrocarbon fuels, this promise has not been realized due to limitations of the current suite of anode materials[12]. The Ni component of traditional Ni-based SOFC anodes catalyzes graphitic carbon formation[12,129,130], prompting the development of alternative Cu-based and oxide-based anode materials[12,131]. The anode must provide both oxygen anion and electronic conductivity and sufficient electrocatalytic activity towards hydrocarbon oxidation.

Mixed ionic-electronic conducting (MIEC) oxides are of great interest as anode as well as the previously discussed cathode materials for SOFCs. Most recently, A-site double perovskite materials of general form $AA'B_2O_{5+\delta}$, have garnered significant attention as candidate anode materials [24,73,82,84,132-134]. With respect to hydrocarbon anode materials, the layered manganite $PrBaMn_2O_{5+\delta}$ has recently been demonstrated as an active, carbon and sulfur tolerant anode for hydrocarbon fuels[134]. $PrBaMn_2O_{5+\delta}$ has also been demonstrated as a potential cathode material due to its stability and activity over a wide range of temperatures and oxygen partial pressure, pO_2 [135-137]. Previous studies on $PrBaMn_2O_{5+\delta}$ have shown a capacity for large changes in oxygen stoichiometry corresponding to values of $0 \leq \delta \leq 1$[136,137]. Studies on the related material $YBaMn_2O_{5+\delta}$

have also shown that the rapid uptake and release of oxygen within the layered manganites is reversible without structural changes[138,139].

The potential high activity of these materials is proposed to originate from their structure. The size difference between the A and A' cations drives A-site layering into alternating $ABO_{3-\delta}$ and $A'BO_{3-\delta}$ perovskite unit cells in a doubling of the simple perovskite unit cell. This cation leads to localization of the oxygen vacancies within the larger radii A-site cation layer[7,8]. In contrast to the random vacancy distribution and anion hopping in single perovskites, this vacancy localization is suggested to lead to facile oxygen transport within this vacancy rich layer[7,8,21]. This is likely key to the high performance provided by these materials. Knowledge of the crystal structure and oxygen anion distribution in these materials is critical to understanding and enhancing their performance.

We have previously utilized high temperature *in-situ* neutron powder diffraction to study the oxygen transport pathways in cubic perovskite [33,34], layered perovskite [7,8], and Ruddlesden-Popper [21,103] structured materials under SOFC cathode conditions. In the current work we report the structure and oxygen stoichiometry of $PrBaMn_2O_{5+\delta}$ under SOFC anode conditions, confirming that the oxygen site in the Pr-O plane is vacant or near-vacant under anode conditions. Only a limited number of oxygen anions are present in this layer under the most oxidizing conditions studied.

7.2 *Experimental*

Layered $PrBaMn_2O_{5+\delta}$ was synthesized through a two-step procedure. A mixture of cubic $Pr_{0.5}Ba_{0.5}MnO_{3-d}$ with hexagonal $BaMnO_{3-d}$[134,135] was first synthesized in air at 1473K as detailed in Section 1.4. This powder was then reduced at 1173K for 14 hours in a humidified 5% H_2 95% N_2 gas mixture passed through a bubbler at room temperature. X-ray diffraction confirmed the formation of a single layered perovskite, space group *P4/mmm*.

In-situ neutron diffraction measurements were conducted at the POWGEN beamline, Spallation Neutron Source (SNS), Oak Ridge Laboratory, Oak Ridge, TN, USAas described in Section 1.6. Measurements were conducted under continuous flow of varying mixtures of pure H_2, N_2, and He humidified with 289K water to control the pO_2 in the sample chamber. The H_2O content of each feed gas stream is calculated as 1.8% by Antoine's equation[140]. Outlet pO_2 values were continuously monitored using a stabilized zirconia oxygen sensor. The pO_2 measured at the outlet and theoretical pO_2 values based on inlet gas composition for each measurement condition are provided in Table 7.1.

***Table 7.1**: Measured and calculated outlet pO_2 as a function of gas composition and temperature*

Outlet log (pO_2) values (atm)								
Gas Atmosphere	Measured				Calculated			
	692K	788K	886K	984K	692K	788K	886K	984K
50%H_2 / N_2				-23.3				-23.4
4% H_2 / He	-32.4	-27.6	-24.2	-21.2	-32.3	-27.8	-24.1	-21.2
0.08% H2 / 0.08% He / 99.84% N_2				-17.9				-17.8

Diffraction patterns were collected flowing 200SCCM of humidified 4% H_2/He at 692K, 788K, 886K, and 984K Å with a total collection time of 1 hour upon stabilization. Diffraction patterns were similarly collected at 984K in 200SCCM humidified 50% H_2/N_2 and 300SCCM humidified 0.08% H_2 / 0.08% He / 99.84% N_2 for 45 minutes and 12 hours, respectively. The sample conditions are reported herein with reference to the calibrated sample temperature and measured sample stage outlet pO_2.

Synchrotron X-ray data was collected at line 11-BM, Advanced Photon Source, Argonne National Labs, Argonne, IL, USA[31], utilizing the mail-in sample program. The profile was collected at room temperature with a calibrated wavelength of 0.413895 Å.

Rietveld[37] refinements were performed using the GSAS package[38] with the EXPGUI interface[39] as described in Section 1.7. Mn, O1, and O2 were refined with anisotropic atomic displacement parameters. Pr and Ba sites were refined with isotropic atomic displacement parameters. Setting these sites to anisotropic resulted in values within a standard deviation of the isotropic case. DIFA, absorption, and scaling parameters were constrained across the measured temperatures.

Bond valence sum (BVS) calculations were performed for the crystal structures obtained under all measured conditions with the VESTA software package[40] using the parameters obtained by Brown and Altermatt[141].

7.3 *Results and Discussion*

A representative Rietveld fit for the collected neutron diffraction patterns is shown in Figure 7.1. The pattern was fit to the *P4/mmm* space group representing a layered perovskite structure, *Table 7.2*. Less than 2 wt-% of an MnO impurity phase, space group $Fm\bar{3}m$, was identified in the sample. The degree of A-site ordering was determined through refinement of the synchrotron X-ray diffraction patterns by adding a disordered phase to the model. The phase fraction for the disordered phase refined to 0 at room temperature, and thus the A-sites were set to be fully ordered and the composition of the sample assumed to match the proposed stoichiometry. Refined values of all parameters and χ^2 for the Rietveld fitting are provided in *Table 7.2* for the data collected at 984K, log (pO$_2$) = -20.85.

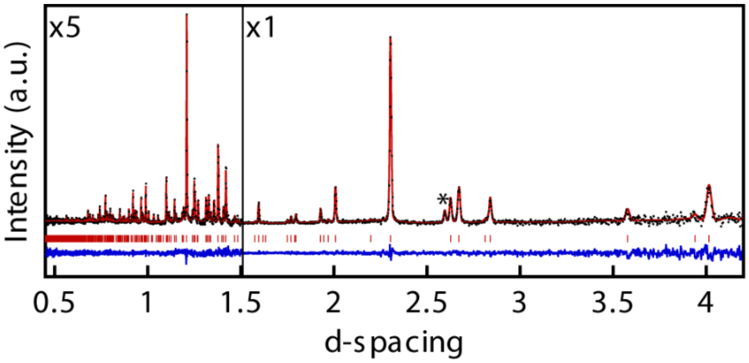

***Figure 7.1**: Neutron diffraction patterns collected at 984 K under log (pO_2) = -21.2 for $PrBaMn_2O_{5+\delta}$. The structure was fitted with the P4/mmm space group. A MnO ($Fm\bar{3}m$) impurity was identified in each sample, with the primary diffraction peak marked by an asterisk below. Measured data (black dots), calculated diffraction pattern (top red line), difference pattern (bottom blue line), and expected peak positions are shown.*

***Table 7.2**: Tetragonal space group P4/mmm, Rietveld fit parameters for Model 1 structures at 984 K, log (pO_2) = -20.85 with sites: Pr: (0,0,0), Ba: (0,0,0.5), Mn: (0.5,0.5,Z), O1: (0.5,0.5,0.5), O2: (0.5,0,Z), O3: (0.5,0.5,0)*

a) $PrBaMn_2O_{5+\delta}$ (Model 1) *P4/mmm* 984 K log *p*O_2: -20.85

a,b (Å)	4.014(1)	χ^2	1.494
c (Å)	7.877(1)	R_P %	6.44
V (Å^3)	126.93(1)	wR_P %	2.39
ρ_c (g/cm^3)	6.134		

	Atomic displacement parameters (Å^2)*100			Z	Fractional Occupancy
	U_{11}/U_{iso}	U_{22}	U_{33}		
Pr	2.1(1)				
Ba	2.4(1)				
Mn	1.4(1)	1.4(1)	2.6(2)	0.243(1)	
O1	3.8(2)	3.8(2)	1.8(2)		1.0
O2	2.7(1)	2.2(1)	4.4(1)	0.194(1)	1.0
O3	2.9				0.05(1)

***Table 7.3**: Tetragonal space group P4/mmm, Rietveld fit parameters for Model 2 (no O3) structures at 984 K, log (pO_2) = -20.85 with sites: Pr: (0,0,0), Ba: (0,0,0.5), Mn: (0.5,0.5,Z), O1: (0.5,0.5,0.5), O2: (0.5,0,Z), O3: (0.5,0.5,0)*

b) $PrBaMn_2O_{5+\delta}$ (Model 1) *P4/mmm* 984 K log pO_2: -20.85

a,b (Å)	4.014(1)	χ^2	1.508
c (Å)	7.877(1)	R_P %	6.54
V (Å^3)	126.93(1)	wR_P %	2.40
ρ_c (g/cm^3)	6.124		

	Atomic displacement parameters (Å^2)*100			Z	Fractional Occupancy
	U_{11}/U_{iso}	U_{22}	U_{33}		
Pr	1.9(1)				
Ba	2.6(1)				
Mn	1.5(1)	1.5(1)	2.6(2)	0.244(1)	
O1	3.7(2)	3.7(2)	1.8(2)		1.0
O2	2.3(1)	2.7(1)	4.4(1)	0.195(1)	1.0

The layered $PrBaMn_2O_{5+\delta}$ structure contains three oxygen sites, shown in Figure 7.2. At all measured conditions, the O1 and O2 site occupancies, corresponding to the oxygen sites in the Ba and Mn layers respectively, refined to within a standard deviation of 1.0 and were therefore fixed to 1.0. The O1 and O2 sites both show anisotropic atomic displacement with preferred displacement tangential to the Mn at the B-site. The position of the O2 sites are significantly displaced into the vacancy rich O3 layers, evidenced by a significant deviation in the O2-Mn-O2 bond angle to ~159 degrees for all measured conditions from the 180° bond angle of an ideal cubic perovskite. Similar deviation in this bond angle is also observed for related layered perovskite materials[7,8].

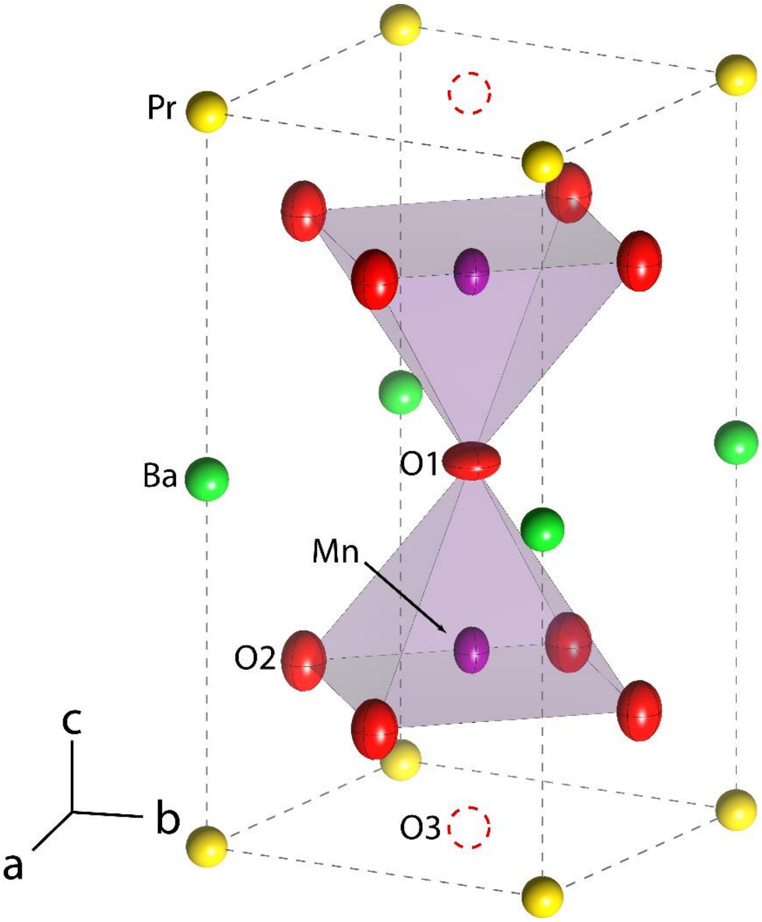

Figure 7.2: *Two stacked unit cells for* $PrBaMn_2O_{5+\delta}$ *at 984K, log* $(pO_2) = -21.2$. *Atoms are shown as ellipsoids of size corresponding to their atomic displacement parameters. Two unit cells were shown to better display the near-vacant O3 site located in the Pr layers.*

In contrast, the occupancy of the O3 site in the Pr layer refines to very low values. That is, all of the vacancies within the $PrBaMn_2O_{5+\delta}$ structure are located within the Pr layer. The site occupancy and atomic displacement parameters are inevitably correlated in the Rietveld refinement as either reduced occupancy or increased atomic displacement will lower the nuclear density at the site. This is particularly problematic with the very low occupancies refined for the O3 site in this study and was addressed by examining two models for the structure.

The first, denoted Model 1 with results shown in *Table 7.2*, allows fractional occupancy of the O3 site and sets the isotropic displacement to be equal to that of the neighboring O2 site to allow for refinement of the fractional occupancy. Model 2, results shown in *Table 7.3*, removes the O3 site to represent a fully vacant layer in the structure. In both cases the other oxygen sites were refined with anisotropic atomic displacement. The quality of fit parameters and determined oxygen stoichiometry for both models for all of the data are shown in Table 7.4. In many cases, the two model fits provide similar quality of fit parameters, making it difficult to confirm the presence or absence of oxygen in the Pr layer from neutrons alone. To aid in this analysis, we also report the oxygen occupancy derived from the TGA data of Sengodan et al at 984 K[134]. In the case of data collected at lower temperatures, we report values linearly extrapolated with respect to temperature from the published TGA data.

Table 7.4*: Quality of fit for Model 1 and Model 2 over a range of measurement conditions. The highlighted occupancy shows the preferred model for each condition.*

Sample Conditions		Chi^2		R_p%		wR_p%	
		Model 1	Model 2	Model 1	Model 2	Model 1	Model 2
692K	log(pO_2) = -32.4	1.768	1.782	6.40	6.53	2.94	2.95
788K	log(pO_2) = -27.6	1.691	1.707	6.59	6.70	2.76	2.78
886K	log(pO_2) = -24.2	1.522	1.542	4.44	4.52	1.67	1.68
984K	log(pO_2) = -17.9	1.996	2.425	4.30	5.09	1.82	2.01
984K	log(pO_2) = -21.2	1.386	1.399	6.19	6.30	2.30	2.31
984K	log(pO_2) = -23.3	1.254	1.257	5.41	5.45	1.94	1.95

Sample Conditions		Occupancy		
		Model 1	Model 2	TGA
692K	log(pO_2) = -32.4	0.04(1)	**0.00**	0.00*
788K	log(pO_2) = -27.6	**0.04(1)**	0.00	0.05*
886K	log(pO_2) = -24.2	**0.05(1)**	0.00	0.06*
984K	log(pO_2) = -17.9	**0.17(1)**	0.00	0.32
984K	log(pO_2) = -21.2	**0.04(1)**	0.00	0.07
984K	log(pO_2) = -23.3	0.02(1)	**0.00**	0.00

The largest neutron model differentiation comes from the data, 984K, log(pO_2)=-17.9 with the largest refined oxygen occupancy of δ=0.17(1) where there is a clear improvement upon allowing occupancy of the O3 site in the Pr layer. The refined value is significantly below the TGA reported value of ~0.32[134], likely due to slow reoxidation kinetics under these conditions in the neutron sample environment. It is necessary to balance sample equilibration times with data collection under the limited time allocation at the beam line and a lack of equilibration is not apparent until full data fitting has been completed[8]. In this case, the sample was allowed to equilibrate for a total of 12 hours but this may have been insufficient.

As an additional example, both models for the data collected at 984K, log(pO_2)=-21.2 atm provide very similar qualities of fit, with χ^2 differing by less than 1%, despite the O3 occupancy of model 1 refining to 0.05(1). While above the expected error based on the standard deviation, this small occupancy is insufficient to significantly impact the overall quality of fit. Increasing the occupancy of the O3 site above this refined level leads to a significant decrease in quality of fit; setting the occupancy to 0.15 increase χ^2 by ~4% for model 1 vs model 2. Therefore, the refinement results suggest some oxygen occupancy of this site, but are not conclusive on their own.

Fourier nuclear density maps are an additional tool for visualizing the presence or absence of oxygen at the O3 site. Figure 7.3 shows the observed nuclear density map generated by GSAS for the data collected at 984K, log(pO_2)=-21.2 atm. The oxygen nuclear density at the center of the O3 site is less than 1/10 of the nuclear density at the fully occupied O1 and O2 sites at 984K, pO_2 = -21.2. This low value is approximately twice the value of the noise in the map data, suggesting that there is a low occupancy of oxygen under these conditions. In contrast, a similar map of the data at 984K, log(pO_2) = -23.3 shows a nuclear density at the center of the O3 site equivalent to the noise level in the data at less than 1/20 of the density on the fully O1 and O2. This further indicates that the O3 site is vacant under these more reducing conditions.

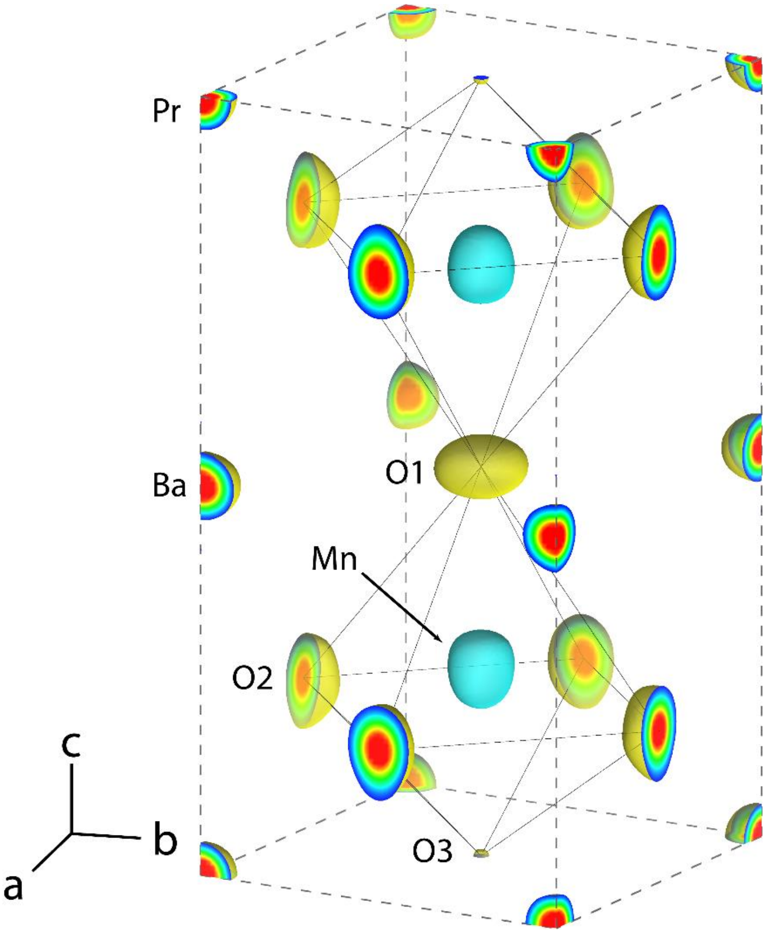

Figure 7.3*: Fourier observed nuclear density diagram at 984 K, log (pO_2) = -21.2 for $PrBaMn_2O_{5+\delta}$. The surfaces drawn in yellow and cyan correspond to positive and negative surfaces, respectively. The progression of color for the interior sections denotes an increase in observed nuclear density, increasing from blue to green to red.*

With all of these caveats in mind, we have highlighted the suggested 'correct' model data for each condition in Table 7.4 and compare this data to the TGA-derived data obtained by Sengodan et al.[134] in Figure 7.4. For the conditions where Model 1 is selected it provides improved quality of and is corroborated by significant nuclear density in the Fourier maps. The two cases where Model 2 is selected are the two cases where the Fourier density maps show nuclear density at O3 consistent with the noise level in the data. Following this procedure, the neutron derived data matches with the TGA data for all points except 984K and log (pO_2) = -17.9 due to the equilibration issues discussed above.

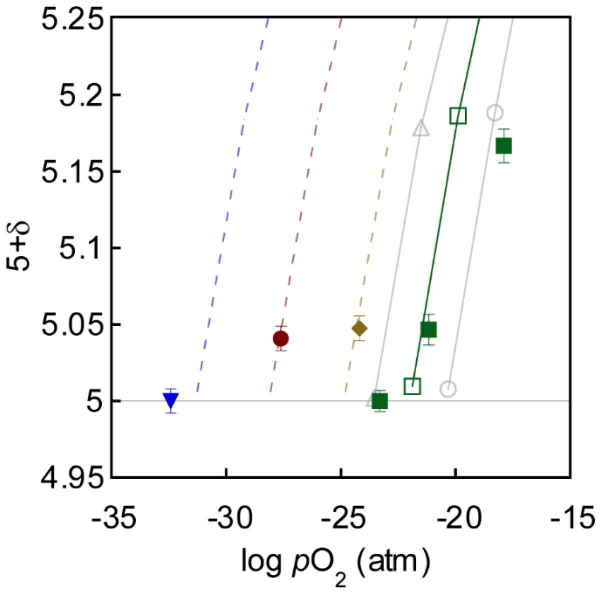

***Figure 7.4**: Overall stoichiometry of the $PrBaMn_2O_{5+\delta}$ structure as a function of pO_2 and temperature. Previously measured data from Sengodan et al.[134] is shown in gray for 650C (upwards open triangle), and 750C (open circle), and in green for 700C (open square). Data measured via neutron diffraction is displayed for 692K (blue downwards triangle), 788K (red circle), 886K (gold diamond), and 984K (green square).*

The trend in lattice parameter with temperature and oxygen stoichiometry is shown in Figure 7.5. At constant gas composition, both *a* and *c* parameters increase with increasing temperature due to thermal expansion. The slight increase in pO_2 of the gas with increasing temperature would be expected to induce chemical contraction of the lattice, however thermal expansion dominates. Decreasing the pO_2 at constant temperature leads to slight chemical expansion. This small shift is due to the small changes in oxygen stoichiometry. A larger chemical contraction is observed upon increasing the pO_2 as the change in oxygen stoichiometry is greater. This is in contrast to our prior findings on $NdBaCo_2O_{5+\delta}$ and $PrBaCo_2O_{5+\delta}$ where the *c*-axis contracts upon reduction. This difference is likely due to the small changes close to zero occupancy at the O3 site of $PrBaMn_2O_{5+\delta}$ compared to larger shifts closer to 50% occupancy for the $NdBaCo_2O_{5+\delta}$ and $PrBaCo_2O_{5+\delta}$ that lead to significant shifts in the position of the B-site cation within the unit cell.

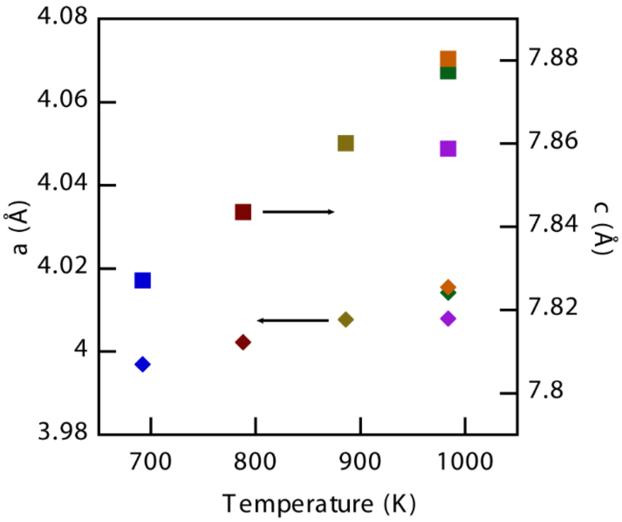

***Figure 7.5**: a and c lattice parameters for $PrBaMn_2O_{5+\delta}$ as a function of temperature. Diamonds and squares represent the a and c lattice parameters, respectively. Color denotes measurement conditions with 692K log (pO_2) = -32.4 (blue), 788K log (pO_2) =-27.6 (red), 886K log (pO_2) =-24.2 (gold), 984K log (pO_2) =-17.9 (purple), 984K log (pO_2) =-21.2 (green), and 984K log (pO_2) =-23.3 (orange).*

The bond valence sums for all anion-cation pairs are shown in Table 7.5. Calculations were performed utilizing Model 1 and Model 2 as shown in Table 7.4, with the bond valence of the O3 site modified by its occupancy. The Mn oxidation state was adjusted to maintain overall neutrality of the crystal structure, resulting in an average oxidation state slightly above $Mn^{+2.5}$. Bond valences shown are lower than the expected oxidation states due to expansion of the bond lengths caused by lattice expansion at increased temperatures.

***Table 7.5**: Bond valence sums around each cation / anion under all measured conditions. Displayed O3 valences are modified by occupancy.*

		Bond Valence Sum					
		Pr	Ba	Mn	O1	O2	O3
692K	$\log(pO_2) = -32.4$	2.905	1.774	2.513	-1.977	-1.932	0
788K	$\log(pO_2) = -27.6$	2.901	1.752	2.524	-1.939	-1.916	-0.098
886K	$\log(pO_2) = -24.2$	2.894	1.721	2.497	-1.915	-1.900	-0.097
984K	$\log(pO_2) = -17.9$	2.805	1.783	2.617	-1.944	-1.886	-0.332
984K	$\log(pO_2) = -21.2$	2.853	1.698	2.476	-1.908	-1.876	-0.093
984K	$\log(pO_2) = -23.3$	2.830	1.689	2.436	-1.901	-1.872	0

7.4 *Conclusion*

The layered manganite $PrBaMn_2O_{5+\delta}$ was examined under reducing conditions at intermediate temperatures via in-situ neutron diffraction. The resulting neutron diffraction patterns were fit to a tetragonal (*P4/mmm*) space group. Under all examined conditions, the O3 oxygen site in the Pr layer became heavily vacant while the O1 and O2 sites in the Ba and Mn layers remained fully occupied. Under all but the least reducing conditions the O3 site was almost completely vacant, containing at most 5% oxygen occupancy. $PrBaMn_2O_{5+\delta}$ remains stable over a wide range of pO_2 and temperature, with no changes in structure or oxygen distribution despite greatly varying δ values. The oxygen partial pressures studied within this work encompass the expected range of partial pressures experienced by a fuel cell anode under operating conditions, showing that $PrBaMn_2O_{5+\delta}$ provides an extremely promising and robust anode material for SOFC operation.

8 Conclusion

The work presented in this dissertation shows the nature of the link between surface reaction rates and bulk conductivity across a wide variety of MIEC materials for use in solid oxide fuel cells (SOFCs). Neutron and synchrotron X-ray diffraction techniques were utilized to characterize the bulk material, with particular focus on the oxygen vacancies and structuring. Isotopic pulse exchange was used to determine the surface reaction rates, with additional surface characterization determined using HS-LEIS or XPS.

Chapter 2 provided the framework for the neutron powder diffraction experiments with the analysis of $Ba_{0.5}Sr_{0.5}Co_{0.5}Fe_{0.5}O_{3-\delta}$. The oxygen stoichiometry of the material was determined and comparisons to other techniques including thermogravimetric analysis and previous neutron diffraction experiments were made. This work proved the efficacy of neutron powder diffraction for determining the bulk structure and oxygen vacancy concentrations within a powder sample.

Chapter 3 provided an analysis of the surface reaction rate for the layered perovskite structures, $LnBaCo_2O_{5+d}$ (Ln = Nd, Pr, Gd). The surface reaction rates measured with O^{18} isotopic pulsing was linked to electrochemical impedance spectroscopy measurements, showing a surface limitation for the overall transport of oxygen through the material. Despite this however, a phase transition in the GBCO was linked with a discontinuity in the surface reaction rate, hinting that the bulk structure has some influence on the surface reaction rate. Surface composition measurements showed slight Ba enrichment on the surface for all materials, but not enough to dominate the surface.

Chapters 4 and 5 provided a combined analysis of the Ruddlesden-Popper series of structures, $A_{n+1}B_nO_{3n+1}$ utilizing both the surface and bulk techniques utilized previously. The oxygen vacancies were found to concentrate heavily in the center of the perovskite layers of the Ruddlesden-Popper structure, with the rock-salt layers remaining almost completely occupied. Surface reaction rate measurements revealed a direct link between oxygen vacancy concentrations and measured surface rate. Despite this, surface composition analysis showed that the surfaces of all three materials were heavily dominated by Sr segregated out of the bulk. This seeming contradiction between surface dominated reaction rates despite almost identical surface structures leads to the conclusion that the overall rate is not dominated by the “true” atomic surface and instead dominated by transport of the oxygen from the sub-surface to the bulk. This also explains the supposed correlation between surface and bulk measurements claimed in numerous studies.

Chapter 6 applies the principles utilized previously to measure cathode materials to a layered perovskite anode material, $Pr_{0.5}Ba_{0.5}MnO_{3-d}$. Neutron powder diffraction analysis showed the material to behave similar to the layered cobaltites discussed in Chapter 3, with oxygen vacancies localized into the Pr layers. The extremely reducing operating conditions present in a SOFC anode however led to extremely low occupancy in the Pr layers, quickly approaching full vacancy.

9 References

References

1. Cox-Galhotra, R. A.; McIntosh, S. Unreliability of simultaneously determining kchem and Dchem via conductivity relaxation for surface-modified La0.6Sr0.4Co0.2Fe0.8O3 − δ. *Solid State Ionics* **2010**, *181*, 1429-1436.

2. Bouwmeester, H. J. M.; Otter, M. W.; Boukamp, B. A. Oxygen transport in La0.6Sr0.4Co1-y Fe y O3-d. *Journal of Solid State Electrochemistry* **2004**, *8*, 599-605.

3. Lane, J. A.; Benson, S. J.; Waller, D.; Kilner, J. A. Oxygen transport in La0.6Sr0.4Co0.2Fe0.8O3−δ. *Solid State Ionics* **1999**, *121*, 201-208.

4. Petric, A.; Huang, P.; Tietz, F. Evaluation of La–Sr–Co–Fe–O perovskites for solid oxide fuel cells and gas separation membranes. *Solid State Ionics* **2000**, *135*, 719-725.

5. Yoo, S.; Choi, S.; Kim, J.; Shin, J.; Kim, G. Investigation of layered perovskite type NdBa1−xSrxCo2O5+δ (x = 0, 0.25, 0.5, 0.75, and 1.0) cathodes for intermediate-temperature solid oxide fuel cells. *Electrochim. Acta* **2013**, *100*, 44-50.

6. Liu, J.; Collins, G.; Liu, M.; Chen, C.; He, J.; Jiang, J.; Meletis, E. I. Ultrafast oxygen exchange kinetics on highly epitaxial PrBaCo2O5+δ thin films. *Appl. Phys. Lett.* **2012**, *100*.

7. Cox-Galhotra, R. A.; Huq, A.; Hodges, J. P.; Yu, C.; Wang, X.; Gong, W.; Jacobson, A. J.; McIntosh, S. An in-situ neutron diffraction study of the crystal structure of

PrBaCo2O5 + δ at high temperature and controlled oxygen partial pressure. *Solid State Ionics* **2013***, 249–250*, 34-40.

8. Cox-Galhotra, R.; Huq, A.; Hodges, J. P.; Kim, J.; Yu, C.; Wang, X.; Jacobson, A. J.; McIntosh, S. Visualizing oxygen anion transport pathways in NdBaCo2O5+δ by in situ neutron diffraction. *J. Mater. Chem. A* **2013***, 1*, 3091-3100.

9. Manthiram, A.; Prado, F.; Armstrong, T. Oxygen separation membranes based on intergrowth structures. *Solid State Ionics* **2002***, 152–153*, 647-655.

10. Mogni, L.; Prado, F.; Caneiro, A.; Manthiram, A. High temperature properties of the n = 2 Ruddlesden–Popper phases (La,Sr)3(Fe,Ni)2O7−δ. *Solid State Ionics* **2006***, 177*, 1807-1810.

11. Carter, S.; Selcuk, A.; Chater, R. J.; Kajda, J.; Kilner, J. A.; Steele, B. C. H. Oxygen transport in selected nonstoichiometric perovskite-structure oxides. *Solid State Ionics* **1992***, 53–56, Part 1*, 597-605.

12. McIntosh, S.; Gorte, R. J. Direct Hydrocarbon Solid Oxide Fuel Cells. *Chem. Rev.* **2004***, 104*, 4845-4866.

13. Adler, S. B. Factors Governing Oxygen Reduction in Solid Oxide Fuel Cell Cathodesâ€ . *Chem. Rev.* **2004***, 104*, 4791-4844.

14. Fleig, J. SOLID OXIDE FUEL CELL CATHODES: Polarization Mechanisms and Modeling of the Electrochemical Performance. *Annu. Rev. Mater. Res.* **2003***, 33*, 361-382.

15. Mizusaki, J.; Yasuda, I.; Shimoyama, J.; Yamauchi, S.; Fueki, K. Electrical Conductivity, Defect Equilibrium and Oxygen Vacancy Diffusion Coefficient of La1 − x Ca x AlO3 − δ Single Crystals. *Journal of The Electrochemical Society* **1993***, 140*, 467-471.

16. Ishihara, T., Ed.; In *Perovskite oxide for solid oxide fuel cells;* Springer: 2009; .

17. Ishigaki, T.; Yamauchi, S.; Kishio, K.; Mizusaki, J.; Fueki, K. Diffusion of oxide ion vacancies in perovskite-type oxides. *Journal of Solid State Chemistry* **1988***, 73*, 179-187.

18. Kilner, J. A. Optimisation of oxygen ion transport in materials for ceramic membrane devices. *Faraday Discuss.* **2007***, 134*, 9-15.

19. Mizusaki, J. Nonstoichiometry, diffusion, and electrical properties of perovskite-type oxide electrode materials. *Solid State Ionics* **1992***, 52*, 79-91.

20. Frontera, C.; Caneiro, A.; Carrillo, O. J.; Garcia-Munoz, J. L. Tailoring Oxygen Content on PrBaCo2O5+d Layered Cobaltites. *Chem. Mater.* **2005***, 17*, 5439-5445.

21. Tomkiewicz, A. C.; Tamimi, M.; Huq, A.; McIntosh, S. Oxygen transport pathways in Ruddlesden-Popper structured oxides revealed via in situ neutron diffraction. *J. Mater. Chem. A* **2015***, 3*, 21864-21874.

22. Kagomiya, I.; Jimbo, K.; Kakimoto, K.; Nakayama, M.; Masson, O. Oxygen vacancy formation and the ion migration mechanism in layered perovskite (Sr,La)3Fe2O7-small delta]. *Phys. Chem. Chem. Phys.* **2014***, 16*, 10875-10882.

23. Shilova, Y. A.; Patrakeev, M. V.; Mitberg, E. B.; Leonidov, I. A.; Kozhevnikov, V. L.; Poeppelmeier, K. R. Order–Disorder Enhanced Oxygen Conductivity and Electron Transport in Ruddlesden–Popper Ferrite-Titanate Sr3Fe2−xTixO6+δ. *Journal of Solid State Chemistry* **2002***, 168*, 275-283.

24. Tomkiewicz, A. C.; Meloni, M.; McIntosh, S. On the link between bulk structure and surface activity of double perovskite based SOFC cathodes. *Solid State Ionics* **2014***, 260*, 55-59.

25. Kaliaguine, S.; Van Neste, A.; Szabo, V.; Gallot, J. E.; Bassir, M.; Muzychuk, R. Perovskite-type oxides synthesized by reactive grinding: Part I. Preparation and characterization. *Applied Catalysis A: General* **2001***, 209*, 345-358.

26. Szabo, V.; Bassir, M.; Van Neste, A.; Kaliaguine, S. Perovskite-type oxides synthesized by reactive grinding: Part II: Catalytic properties of LaCo(1−x)FexO3 in VOC oxidation. *Applied Catalysis B: Environmental* **2002***, 37*, 175-180.

27. Pechini, M. P. 3,330,697, 1967.

28. Taguchi, H.; Matsuda, D.; Nagao, M.; Tanihata, K.; Miyamoto, Y. Synthesis of Perovskite-Type (La1-xSrx)MnO3 (O <= X <= 0.3) at Low Temperature. *J Am Ceram Soc* **1992***, 75*, 201-202.

29. Huízar-Félix, A. M.; Hernández, T.; de la Parra, S.; Ibarra, J.; Kharisov, B. Sol–gel based Pechini method synthesis and characterization of Sm1 − xCaxFeO3 perovskite 0.1 ≤ x ≤ 0.5. *Powder Technol* **2012***, 229*, 290-293.

30. Vaqueiro, P.; Lopez-Quintela, M. A. Influence of Complexing Agents and pH on Yttrium-Iron Garnet Synthesized by the Sol-Gel Method. *Chem. Mater.* **1997**, *9*, 2836-2841.

31. Argonne National Laboratory Beamline 11-BM: High Resolution Powder Diffraction. *http://11bm.xray.aps.anl.gov/description.html*2013).

32. Toby, B. A Very Abbreviated Introduction to Powder Diffraction. *14th National School on Neutron and X-ray Scattering* **2012**.

33. Tomkiewicz, A. C.; Tamimi, M. A.; Huq, A.; McIntosh, S. Evidence for the low oxygen stoichiometry of cubic Ba0.5Sr0.5Co0.5Fe0.5O3-δ from in-situ neutron diffraction. *Solid State Ionics* **2013**, *253*, 27-31.

34. Tamimi, M. A.; Tomkiewicz, A. C.; Huq, A.; McIntosh, S. On the link between bulk and surface properties of mixed ion electron conducting materials Ln0.5Sr0.5Co0.8Fe0.2O3-small delta] (Ln = La, Pr, Nd). *J. Mater. Chem. A* **2014**, *2*, 18838-18847.

35. Tamimi, M. A.; McIntosh, S. High temperature in situ neutron powder diffraction of oxides. *J. Mater. Chem. A* **2014**, *2*, 6015-6026.

36. Touloukian, Y. S.; Kriby, R. K.; Taylor, R. E.; Desai, P. D. *Thermophysical Properties of Matter;* Purdue Research Foundation: 1977; Vol. 13.

37. Rietveld, H. M. A Profile Refinement Method for Nuclear and Magnetic Structures. *J. Appl. Crystallog.* **1969**, *2*, 65-71.

38. Larson, A. C.; von Dreele, R. B. General Structure Analysis System (GSAS). *Los Alamos National Laboratory: Los Alamos, New Mexico* **2004**.

39. B. H. Toby, E. *J. Appl. Cryst.* **2001**, 210-213.

40. Momma, K.; Izumi, F. VESTA 3 for three-dimensional visualization of crystal, volumetric and morphology data. *J. Appl. Crystallog.* **2011***, 44*, 1272-1276.

41. Bonturim, E.; Mazzocchi, V.; Parente, C.; Mestnik-Filho, J.; de Lima, N.; Seo, E. Oxygen stoichiometry of Ba0.50Sr0.50Co0.80Fe0.20O3-d obtained by EDTA-citrate method and measured by X-ray and neutron diffraction. *J. Radioanal. Nucl.* **2015**, 1-5.

42. McIntosh, S.; Vente, J. F.; Haije, W. G.; Blank, D. H. A.; Bouwmeester, H. J. M. Oxygen Stoichiometry and Chemical Expansion of Ba0.5Sr0.5Co0.8Fe0.2O3-δ Measured by in Situ Neutron Diffraction. *Chem. Mater.* **2006***, 18*, 2187-2193.

43. McIntosh, S.; Vente, J. F.; Haije, W. G.; Blank, D. H. A.; Bouwmeester, H. J. M. Phase stability and oxygen non-stoichiometry of SrCo0.8Fe0.2O3−δ measured by in situ neutron diffraction. *Solid State Ionics* **2006***, 177*, 833-842.

44. Bouwmeester, H. J. M.; Song, C.; Zhu, J.; Yi, J.; van Sint Annaland, M.; Boukamp, B. A. A novel pulse isotopic exchange technique for rapid determination of the oxygen surface exchange rate of oxide ion conductors. *Physical Chemistry Chemical Physics* **2009**, 9640-9643.

45. Shin, H. H.; - McIntosh, S. On the H2/D2 isotopic exchange rate of proton conducting barium cerates and zirconates. *J. Mater. Chem. A* **2013**, 7639.

46. Shin, H. H.; McIntosh, S. Insights into Hydrogen Oxidation on SOFC Anode Materials by Isotopic Exchange. *ECS Electrochemistry Letters* **2013***, 2*, F88-F91.

47. van den Bossche, M.; McIntosh, S. The rate and selectivity of methane oxidation over La0.75Sr0.25CrxMn1−xO3−δ as a function of lattice oxygen stoichiometry under solid oxide fuel cell anode conditions. *Journal of Catalysis* **2008***, 255*, 313-323.

48. Maier, J. On the correlation of macroscopic and microscopic rate constants in solid state chemistry. *Solid State Ionics* **1998***, 112*, 197-228.

49. Crumlin, E. J.; Mutoro, E.; Liu, Z.; Grass, M. E.; Biegalski, M. D.; Lee, Y.; Morgan, D.; Christen, H. M.; Bluhm, H.; Shao-Horn, Y. Surface strontium enrichment on highly active perovskites for oxygen electrocatalysis in solid oxide fuel cells. *Energy Environ. Sci.* **2012***, 5*, 6081-6088.

50. Hansen, K. V.; Norrman, K.; Mogensen, M. TOF-SIMS studies of yttria-stabilised zirconia. *Surf. Interface Anal.* **2006***, 38*, 911-916.

51. Leadley, D. *http://www2.warwick.ac.uk/fac/sci/physics/current/postgraduate/regs/mpags/ex5/techniques/electronic/xps/* (accessed May, 2014).

52. ter Veen, H. R. J.; Kim, T.; Wachs, I. E.; Brongersma, H. H. Applications of High Sensitivity-Low Energy Ion Scattering (HS-LEIS) in heterogeneous catalysis. *Catalysis Today* **2009***, 140*, 197-201.

53. Arnold, M.; Gesing, T. M.; Martynczuk, J.; Feldhoff, A. Correlation of the Formation and the Decomposition Process of the BSCF Perovskite at Intermediate Temperatures. *Chem. Mater.* **2008***, 20*, 5851-5858.

54. Bucher, E.; Egger, A.; Ried, P.; Sitte, W.; Holtappels, P. Oxygen nonstoichiometry and exchange kinetics of Ba0.5Sr0.5Co0.8Fe0.2O3 − δ. *Solid State Ionics* **2008***, 179*, 1032-1035.

55. Dalslet, B. T.; Søgaard, M.; Bouwmeester, H. J. M.; Hendriksen, P. V. Defect chemistry and oxygen transport of (La0.6Sr0.4 − xMx)0.99Co0.2Fe0.8O3 − δ, M = Ca (x = 0.05, 0.1), Ba (x = 0.1, 0.2), Sr: Part I: Defect chemistry. *Solid State Ionics* **2009***, 180*, 1173-1182.

56. Efimov, K.; Xu, Q.; Feldhoff, A. Transmission Electron Microscopy Study of Ba0.5Sr0.5Co0.8Fe0.2O3-δ Perovskite Decomposition at Intermediate Temperatures. *Chem. Mater.* **2010***, 22*, 5866-5875.

57. Jung, J.; Misture, S. T.; Edwards, D. D. Oxygen stoichiometry, electrical conductivity, and thermopower measurements of BSCF (Ba0.5Sr0.5CoxFe1 − xO3 − δ, 0≤ x ≤ 0.8) in air. *Solid State Ionics* **2010***, 181*, 1287-1293.

58. Kriegel, R.; Kircheisen, R.; Töpfer, J. Oxygen stoichiometry and expansion behavior of Ba0.5Sr0.5Co0.8Fe0.2O3 − δ. *Solid State Ionics* **2010***, 181*, 64-70.

59. Kuklja, M. M.; Mastrikov, Y. A.; Jansang, B.; Kotomin, E. A. First principles calculations of (Ba,Sr)(Co,Fe)O3 − δ structural stability. *Solid State Ionics* **2013***, 230*, 21-26.

60. Mueller, D. N.; De Souza, R. A.; Weirich, T. E.; Roehrens, D.; Mayer, J.; Martin, M. A kinetic study of the decomposition of the cubic perovskite-type oxide BaxSr1-xCo0.8Fe0.2O3-δ] (BSCF) (x = 0.1 and 0.5). *Phys. Chem. Chem. Phys.* **2010***, 12*, 10320-10328.

61. Mueller, D. N.; De Souza, R. A.; Yoo, H.; Martin, M. Phase Stability and Oxygen Nonstoichiometry of Highly Oxygen-Deficient Perovskite-Type Oxides: A Case Study of (Ba,Sr)(Co,Fe)O3-δ. *Chem. Mater.* **2012***, 24*, 269-274.

62. Müller, P.; Störmer, H.; Meffert, M.; Dieterle, L.; Niedrig, C.; Wagner, S. F.; Ivers-Tiffée, E.; Gerthsen, D. Secondary Phase Formation in $Ba_{0.5}Sr_{0.5}Co_{0.8}Fe_{0.2}O_{3-d}$ Studied by Electron Microscopy. *Chem. Mater.* **2013***, 25*, 564-573.

63. Müller, P.; Störmer, H.; Dieterle, L.; Niedrig, C.; Ivers-Tiffée, E.; Gerthsen, D. Decomposition pathway of cubic Ba0.5Sr0.5Co0.8Fe0.2O3 − δ between 700 °C and 1000 °C analyzed by electron microscopic techniques. *Solid State Ionics* **2012***, 206*, 57-66.

64. Niedrig, C.; Taufall, S.; Burriel, M.; Menesklou, W.; Wagner, S. F.; Baumann, S.; Ivers-Tiffée, E. Thermal stability of the cubic phase in Ba0.5Sr0.5Co0.8Fe0.2O3 - δ (BSCF)1. *Solid State Ionics* **2011***, 197*, 25-31.

65. Shao, Z.; Yang, W.; Cong, Y.; Dong, H.; Tong, J.; Xiong, G. Investigation of the permeation behavior and stability of a Ba0.5Sr0.5Co0.8Fe0.2O3−δ oxygen membrane. *J. Membr. Sci.* **2000***, 172*, 177-188.

66. Švarcová, S.; Wiik, K.; Tolchard, J.; Bouwmeester, H. J. M.; Grande, T. Structural instability of cubic perovskite BaxSr1 − xCo1 − yFeyO3 − δ. *Solid State Ionics* **2008**, *178*, 1787-1791.

67. Vente, J.; McIntosh, S.; Haije, W.; Bouwmeester, H. M. Properties and performance of BaxSr1-xCo0.8Fe0.2O3-d materials for oxygen transport membranes. *Journal of Solid State Electrochemistry* **2006**, *10*, 581-588.

68. Shao, Z.; Haile, S. M. A high-performance cathode for the next generation of solid-oxide fuel cells. *Nature* **2004**, *431*, 170-173.

69. McIntosh, S.; Vente, J. F.; Haije, W. G.; Blank, D. H. A.; Bouwmeester, H. J. M. Structure and oxygen stoichiometry of SrCo0.8Fe0.2O3−δ and Ba0.5Sr0.5Co0.8Fe0.2O3−δ. *Solid State Ionics* **2006**, *177*, 1737-1742.

70. Mitchell, B. J.; Rogan, R. C.; Richardson Jr., J. W.; Ma, B.; Balachandran, U. Stability of the cubic perovskite SrFe0.8Co0.2O3−δ. *Solid State Ionics* **2002**, *146*, 313-321.

71. King, G.; Woodward, P. M. Cation ordering in perovskites. *J. Mater. Chem.* **2010**, *20*, 5785-5796.

72. Yashima, M.; Kamioka, T. Neutron diffraction study of the perovskite-type lanthanum cobaltite La0.6Sr0.4Co0.8Fe0.2O3 − δ at 1260 °C and 394 °C. *Solid State Ionics* **2008**, *178*, 1939-1943.

73. Tarancón, A.; Skinner, S. J.; Chater, R. J.; Hernandez-Ramirez, F.; Kilner, J. A. Layered perovskites as promising cathodes for intermediate temperature solid oxide fuel cells. *J. Mater. Chem.* **2007**, 3175.

74. Kim, G.; Wang, S.; Jacobson, A. J.; Reimus, L.; Brodersen, P.; Mims, C. A. Rapid oxygen ion diffusion and surface exchange kinetics in PrBaCo2O5+ with a perovskite related structure and ordered A cations. *J. Mater. Chem.* **2007**, 2500.

75. Tarancon, A.; Burriel, M.; Santiso, J.; Skinner, S. J.; Kilner, J. A. Advances in layered oxide cathodes for intermediate temperature solid oxide fuel cells. *J. Mater. Chem.* **2010***, 20*, 3799-3813.

76. De Souza, R. A.; Kilner, J. A. Oxygen transport in La1−xSrxMn1−yCoyO3±δ perovskites: Part II. Oxygen surface exchange. *Solid State Ionics* **1999***, 126*, 153-161.

77. De Souza, R. A. A universal empirical expression for the isotope surface exchange coefficients (k*) of acceptor-doped perovskite and fluorite oxides. *Phys. Chem. Chem. Phys.* **2006***, 8*, 890-897.

78. Cox-Galhotra, R. A.; McIntosh, S. Electrical conductivity relaxation of polycrystalline PrBaCo2O5 + δ thin films. *Solid State Ionics* **2012***, 228*, 14-18.

79. Baumann, F. S.; Fleig, J.; Konuma, M.; Starke, U.; Habermeier, H.; Maier, J. Strong Performance Improvement of La0.6Sr0.4Co0.8Fe0.2O3 − δ SOFC Cathodes by Electrochemical Activation. *Journal of The Electrochemical Society* **2005***, 152*, A2074-A2079.

80. Toby, B. H. EXPGUI, a graphical user interface for GSAS. *Journal of Applied Crystallography* **2001***, 34*, 210-213.

81. Streule, S.; Podlesnyak, A.; Sheptyakov, D.; Pomjakushina, E.; Stingaciu, M.; Conder, K.; Medarde, M.; Patrakeev, M. V.; Leonidov, I. A.; Kozhevnikov, V. L.; Mesot, J. High-temperature order-disorder transition and polaronic conductivity in PrBaCo2O5.48. *Phys.Rev.B* **2006**, *73*, 094203.

82. Seymour, I. D.; Tarancón, A.; Chroneos, A.; Parfitt, D.; Kilner, J. A.; Grimes, R. W. Anisotropic oxygen diffusion in PrBaCo2O5.5 double perovskites. *Solid State Ionics* **2012**, *216*, 41-43.

83. Tarancón, A.; Marrero-López, D.; Peña-Martínez, J.; Ruiz-Morales, J. C.; Núñez, P. Effect of phase transition on high-temperature electrical properties of GdBaCo2O5 + x layered perovskite. *Solid State Ionics* **2008**, *179*, 611-618.

84. Taskin, A. A.; Lavrov, A. N.; Ando, Y. Achieving fast oxygen diffusion in perovskites by cation ordering. *Appl. Phys. Lett.* **2005**, *86*.

85. Peña-Martínez, J.; Tarancón, A.; Marrero-López, D.; Ruiz-Morales, J. C.; Núñez, a. Evaluation of GdBaCo2O5 + δ as Cathode Material for Doped Lanthanum Gallate Electrolyte IT-SOFCs. *Fuel Cells* , 351.

86. Hu, Y.; Bogicevic, C.; Bouffanais, Y.; Giot, M.; Hernandez, O.; Dezanneau, G. Synthesis, physical–chemical characterization and electrochemical performance of GdBaCo2−xNixO5+δ (x = 0–0.8) as cathode materials for IT-SOFC application. *J. Power Sources* **2013**, *242*, 50-56.

87. Li, N.; Wei, B.; Lü, Z.; Huang, X.; Su, W. GdBaCo2O5+δ–Sm0.2Ce0.8O1.9 composite cathodes for intermediate temperature SOFCs. *J. Alloys Compounds* **2011**, *509*, 3651-3655.

88. Choi, M. B.; Jeon, S. Y.; Lee, J. S.; Hwang, H. J.; Song, S. J. Chemical diffusivity and ionic conductivity of GdBaCo2O5+δ. *J. Power Sources* **2010***, 195*, 1059-1064.

89. Vance, A. A.; McIntosh, S. Performance and Activation Behavior of Surface-Doped Thin-Film La0.8Sr0.2MnO3 − δ Cathodes. *Journal of The Electrochemical Society* **2008***, 155*, B1-B7.

90. Jiang, S. Activation, microstructure, and polarization of solid oxide fuel cell cathodes. *Journal of Solid State Electrochemistry* **2007***, 11*, 93-102.

91. Mogni, L.; Prado, F.; Jiménez, C.; Caneiro, A. Oxygen order–disorder phase transition in layered GdBaCo2O5+δ perovskite: Thermodynamic and transport properties. *Solid State Ionics* **2013***, 240*, 19-28.

92. Jacobson, A. J. Materials for Solid Oxide Fuel Cells. *Chem. Mater.* **2010***, 22*, 660-674.

93. Amow, G.; Davidson, I. J.; Skinner, S. J. A comparative study of the Ruddlesden-Popper series, Lan+1NinO3n+1 (n = 1, 2 and 3), for solid-oxide fuel-cell cathode applications. *Solid State Ionics* **2006***, 177*, 1205-1210.

94. Kharton, V. V.; Viskup, A. P.; Kovalevsky, A. V.; Naumovich, E. N.; Marques, F. M. B. Ionic transport in oxygen-hyperstoichiometric phases with K2NiF4-type structure. *Solid State Ionics* **2001***, 143*, 337-353.

95. Kharton, V.,V.; Viskup, A.,P.; Naumovich, E.,N.; Marques, F.,M.B. Oxygen ion transport in La2NiO4-based ceramics. *J. Mater. Chem.* **1999***, 9*, 2623-2629.

96. Kovalevsky, A. V.; Kharton, V. V.; Yaremchenko, A. A.; Pivak, Y. V.; Tsipis, E. V.; Yakovlev, S. O.; Markov, A. A.; Naumovich, E. N.; Frade, J. R. Oxygen permeability,

stability and electrochemical behavior of Pr2NiO4+d -based materials. *Journal of Electroceramics* **2007**, *18*, 205-218.

97. Bassat, J. M.; Odier, P.; Villesuzanne, A.; Marin, C.; Pouchard, M. Anisotropic ionic transport properties in La2NiO4+δ single crystals. *Solid State Ionics* **2004**, *167*, 341-347.

98. Skinner, S. J.; Kilner, J. A. Oxygen diffusion and surface exchange in La2−xSrxNiO4+δ. *Solid State Ionics* **2000**, *135*, 709-712.

99. Kilner, J. A.; Shaw, C. K. M. Mass transport in La2Ni1−xCoxO4+δ oxides with the K2NiF4 structure. *Solid State Ionics* **2002**, *154–155*, 523-527.

100. Markov, A. A.; Patrakeev, M. V.; Kharton, V. V.; Pivak, Y. V.; Leonidov, I. A.; Kozhevnikov, V. L. Oxygen Nonstoichiometry and Ionic Conductivity of Sr3Fe2-xScxO7-d. *Chem. Mater.* **2007**, *19*, 3980-3987.

101. Prado, F.; Armstrong, T.; Caneiro, A.; Manthiram, A. Structural Stability and Oxygen Permeation Properties of Sr3 − x La x Fe2 − y Co y O 7 − δ (0 ⩽ x ⩽ 0.3 and 0 ⩽ y ⩽ 1.0) . *Journal of The Electrochemical Society* **2001**, *148*, J7-J14.

102. McIntosh, S. Oxygen Anion Transport in Solid Oxides. In ; Kreysa, G., Ota, K. and Savinell, R., Eds.; Springer New York: 2014; pp 1461-1475.

103. Tomkiewicz, A. C.; Tamimi, M. A.; Huq, A.; McIntosh, S. FD Electrolysis: Is the Surface Oxygen Exchange Rate Linked to Bulk Ion Diffusivity in Mixed Conducting Ruddlesden-Popper Phases? *Faraday Discuss.* **2015**.

104. Armstrong, T.; Prado, F.; Manthiram, A. Synthesis, crystal chemistry, and oxygen permeation properties of LaSr3Fe3−xCoxO10 (0≤x≤1.5). *Solid State Ionics* **2001***, 140*, 89-96.

105. Sharma, I.; Singh, D. Solid state chemistry of Ruddlesden-Popper type complex oxides. *Bull. Mater. Sci.* **1998***, 21*, 363-374.

106. Von Dreele, R. B.; Jorgensen, J. D.; Windsor, C. G. Rietveld refinement with spallation neutron powder diffraction data. *Journal of Applied Crystallography* **1982***, 15*, 581-589.

107. Chatzichristodoulou, C.; Hauback, B. C.; Hendriksen, P. V. In situ X-ray and neutron diffraction of the Ruddlesden–Popper compounds (RE2−xSrx)0.98(Fe0.8Co0.2)1−yMgyO4−δ (RE=La, Pr): Structure and CO2 stability. *Journal of Solid State Chemistry* **2013***, 201*, 164-171.

108. Bahout, M.; Tonus, F.; Prestipino, C.; Pelloquin, D.; Hansen, T.; Fonda, E.; Battle, P. D. High-temperature redox chemistry of Pr0.5Sr1.5Cr0.5Mn0.5O4-small delta] investigated in situ by neutron diffraction and X-ray absorption spectroscopy under reducing and oxidizing gas flows. *J. Mater. Chem.* **2012***, 22*, 10560-10570.

109. Chatzichristodoulou, C.; Schönbeck, C.; Hagen, A.; Hendriksen, P. V. Defect chemistry, thermomechanical and transport properties of (RE2 − xSrx)0.98(Fe0.8Co0.2)1 − yMgyO4 − δ (RE = La, Pr). *Solid State Ionics* **2013***, 232*, 68-79.

110. Mazo, G. N.; Kazakov, S. M.; Kolchina, L. M.; Istomin, S. Y.; Antipov, E. V.; Lyskov, N. V.; Galin, M. Z.; Leonova, L. S.; Fedotov, Y. S.; Bredikhin, S. I.; Liu, Y.; Svensson,

G.; Shen, Z. Influence of structural arrangement of R2O2 slabs of layered cuprates on high-temperature properties important for application in IT-SOFC. *Solid State Ionics* **2014**, *257*, 67-74.

111. Dann, S. E.; Weller, M. T.; Currie, D. B. Structure and oxygen stoichiometry in Sr3Fe2O7−y, 0 ≤ y ≤ 1.0. *Journal of Solid State Chemistry* **1992**, *97*, 179-185.

112. Prado, F.; Mogni, L.; Cuello, G. J.; Caneiro, A. Neutron powder diffraction study at high temperature of the Ruddlesden–Popper phase Sr3Fe2O6 + δ. *Solid State Ionics* **2007**, *178*, 77-82.

113. Lee, J. Y.; Swinnea, J. S.; Steinfink, H.; Reiff, W. M.; Pei, S.; Jorgensen, J. D. The Crystal Chemistry and Physical Properties of the Triple Layer Perovskite Intergrowths LaSr3Fe3O10-δ and LaSr3(Fe3-xAlx)O10-δ. *Journal of Solid State Chemistry* **1993**, *103*, 1-15.

114. Mitchell, J. F.; Burley, J.; Short, S. Crystal and magnetic structure of NdBaCo2O5+δ: Spin states in a perovskite-derived, mixed-valent cobaltite. *J. Appl. Phys.* **2003**, *93*, 7364-7366.

115. Khalyavin, D.; Prokhnenko, O.; St\u\sser, N.; Sikolenko, V.; Efimov, V.; Salak, A.; Yaremchenko, A.; Kharton, V. Crystal and magnetic structures of NdBaCo2O5+d (d ~ 0.75): A neutron diffraction study. *Phys.Rev.B* **2008**, *77*, 174417.

116. Lobanovsky, L. S.; Troyanchuk, I. O.; Szymczak, H.; Prokhnenko, O. Structure and physical properties of layered double perovskite NdBaCo2O5.50 + d (d ~ 0.25). *Journal of Experimental and Theoretical Physics* **2006**, *103*, 740-746.

117. Saiful Islam, M. Ionic transport in ABO3 perovskite oxides: a computer modelling tour. *J. Mater. Chem.* **2000**, *10*, 1027-1038.

118. Cherry, M.; Islam, M. S.; Catlow, C. R. A. Oxygen Ion Migration in Perovskite-Type Oxides. *Journal of Solid State Chemistry* **1995**, *118*, 125-132.

119. Tealdi, C.; Ferrara, C.; Mustarelli, P.; Islam, M. S. Vacancy and interstitial oxide ion migration in heavily doped La2-xSrxCoO4+/-small delta]. *J. Mater. Chem.* **2012**, *22*, 8969-8975.

120. Kubicek, M.; Limbeck, A.; Frömling, T.; Hutter, H.; Fleig, J. Relationship between Cation Segregation and the Electrochemical Oxygen Reduction Kinetics of La0.6Sr0.4CoO3−δ Thin Film Electrodes. *Journal of The Electrochemical Society* **2011**, *158*, B727-B734.

121. Druce, J.; Tellez, H.; Burriel, M.; Sharp, M. D.; Fawcett, L. J.; Cook, S. N.; McPhail, D. S.; Ishihara, T.; Brongersma, H. H.; Kilner, J. A. Surface termination and subsurface restructuring of perovskite-based solid oxide electrode materials. *Energy Environ. Sci.* **2014**, *7*, 3593-3599.

122. Dunitz, J. D.; Schomaker, V.; Trueblood, K. N. Interpretation of atomic displacement parameters from diffraction studies of crystals. *J. Phys. Chem.* **1988**, *92*, 856-867.

123. Kilner, J. A.; De Souza, R. A.; Fullarton, I. C. Surface exchange of oxygen in mixed conducting perovskite oxides. *Solid State Ionics* **1996**, *86–88, Part 2*, 703-709.

124. Merkle, R.; Maier, J.; Bouwmeester, H. J. M. A Linear Free Energy Relationship for Gas-Solid Interactions: Correlation between Surface Rate Constant and Diffusion

Coefficient of Oxygen Tracer Exchange for Electron-Rich Perovskites. *Angewandte Chemie International Edition* **2004**, *43*, 5069-5073.

125. Jiang, S. P.; Love, J. G. Origin of the initial polarization behavior of Sr-doped LaMnO3 for O2 reduction in solid oxide fuel cells. *Solid State Ionics* **2001**, *138*, 183-190.

126. Wang, W.; Jiang, S. P. A mechanistic study on the activation process of (La, Sr)MnO3 electrodes of solid oxide fuel cells. *Solid State Ionics* **2006**, *177*, 1361-1369.

127. Decorse, P.; Caboche, G.; Dufour, L. A comparative study of the surface and bulk properties of lanthanum-strontium-manganese oxides La1−xSrxMnO3±δ as a function of Sr-content, oxygen potential and temperature. *Solid State Ionics* **1999**, *117*, 161-169.

128. Druce, J.; Ishihara, T.; Kilner, J. Surface composition of perovskite-type materials studied by Low Energy Ion Scattering (LEIS). *Solid State Ionics* **2014**, *262*, 893-896.

129. Clarke, S. H.; Dicks, A. L.; Pointon, K.; Smith, T. A.; Swann, A. Catalytic aspects of the steam reforming of hydrocarbons in internal reforming fuel cells. *Catalysis Today* **1997**, *38*, 411-423.

130. Dicks, A. L. Advances in catalysts for internal reforming in high temperature fuel cells. *J. Power Sources* **1998**, *71*, 111-122.

131. Tao, S.; Irvine, J. T. S. Discovery and characterization of novel oxide anodes for solid oxide fuel cells. *The Chemical Record* **2004**, *4*, 83-95.

132. Kim, G.; Wang, S.; Jacobson, A. J.; Yuan, Z.; Donner, W.; Chen, C. L.; Reimus, L.; Brodersen, P.; Mims, C. A. Oxygen exchange kinetics of epitaxial PrBaCo2O5+δ thin films. *Appl. Phys. Lett.* **2006***, 88*.

133. Tarancón, A.; Morata, A.; Dezanneau, G.; Skinner, S. J.; Kilner, J. A.; Estradé, S.; Hernández-Ramírez, F.; Peiró, F.; Morante, J. R. GdBaCo2O5+x layered perovskite as an intermediate temperature solid oxide fuel cell cathode. *J. Power Sources* **2007***, 174*, 255-263.

134. Sengodan, S.; Choi, S.; Jun, A.; Shin, T. H.; Ju, Y.; Jeong, H. Y.; Shin, J.; Irvine, J. T. S.; Kim, G. Layered oxygen-deficient double perovskite as an efficient and stable anode for direct hydrocarbon solid oxide fuel cells. *Nat Mater* **2015***, 14*, 205-209.

135. Shin, T. H.; Myung, J.; Verbraeken, M. C.; Kim, G.; Irvine, J. T. S. FD Electrolysis: Oxygen Deficient Layered Double Perovskite as an Active Cathode for CO2 Electrolysis Using Solid Oxide Conductor. *Faraday Discuss.* **2015**.

136. S V Trukhanov and L S Lobanovski and M V Bushinsky and V V Fedotova and I O Troyanchuk and A V Trukhanov and V A Ryzhov and H Szymczak and R Szymczak and,M.Baran Study of A-site ordered PrBaMn2O6-d manganite properties depending on the treatment conditions. *Journal of Physics: Condensed Matter* **2005***, 17*, 6495.

137. Trukhanov, S. V.; Trukhanov, A. V.; Szymczak, H.; Szymczak, R.; Baran, M. Thermal stability of A-site ordered PrBaMn2O6 manganites. *Journal of Physics and Chemistry of Solids* **2006***, 67*, 675-681.

138. Motohashi, T.; Ueda, T.; Masubuchi, Y.; Kikkawa, S. Oxygen Intake / Release Mechanism of Double-Perovskite Type BaYMn2O5+d (0 ≤ d ≤ 1). *J. Phys. Chem. C* **2013***, 117*, 12560-12566.

139. Motohashi, T.; Ueda, T.; Masubuchi, Y.; Takiguchi, M.; Setoyama, T.; Oshima, K.; Kikkawa, S. Remarkable Oxygen Intake/Release Capability of BaYMn2O5+d: Applications to Oxygen Storage Technologies. *Chem. Mater.* **2010***, 22*, 3192-3196.

140. Wagner, W.; Pruß, A. The IAPWS Formulation 1995 for the Thermodynamic Properties of Ordinary Water Substance for General and Scientific Use. *Journal of Physical and Chemical Reference Data* **2002***, 31*, 387-535.

141. Brown, I. D.; Altermatt, D. Bond-valence parameters obtained from a systematic analysis of the Inorganic Crystal Structure Database. *Acta Crystallographica Section B* **1985***, 41*, 244-247.

10 Vita

Alex Tomkiewicz was born on September 14, 1989 in Rochester, New York to John and Heidi Tomkiewicz. In his youth, he was always excited about science and technology, with a particular interest in chemistry. He began studying Chemical Engineering at Cornell University in 2007, receiving his Bachelor of Science degree in 2011. He began studying as a PhD student later that year at Lehigh University. Under the supervision of his advisor, Prof. Steven McIntosh, Alex has published several papers in the field of solid oxide fuel cells, focusing on the oxygen transport within the anode and cathode. The main results of his work are described in this dissertation.